SAPIENZA
UNIVERSITÀ DI ROMA

Studies of Longitudinal Coupled-Bunch Instabilities in the LHC Injectors Chain

Scuola di dottorato in Fisica degli Acceleratori

Dottorato di Ricerca in Fisica – XXIX Ciclo

Candidate

Letizia Ventura
ID number 1144803

Thesis Advisors

Professor: Mauro Migliorati
CERN Supervisor: Dr. Guido Sterbini

A thesis submitted in partial fulfillment of the requirements
for the degree of Doctor of Philosophy in Physics

Thesis not yet defended

Studies of Longitudinal Coupled-Bunch Instabilities in the LHC Injectors Chain
Ph.D. thesis. Sapienza – University of Rome

This thesis has been typeset by LaTeX and the Sapthesis class.

Author's email: ventura.letizia@gmail.com

If your dreams do not scare you, they are not big enough.
-Ellen Johnson Sirleaf

Contents

List of Figures

List of Tables

Introduction

Colliders are the privileged instruments to explore the high energy frontier in particle physics. They require high quality particle beams with high intensity, low transverse emittances, and low energy spread to achieve high luminosity. These requirements present a number of challenges, including the suppression of beam instabilities driven by collective effects that lead to intensity limitations and have a considerable detrimental impact on the performance of high intensity machines.

Collective effects are caused by the interactions between charged particles and their surroundings and become more significant, and therefore more disrupting, at a high beam intensity. The electromagnetic fields produced by the interaction between protons and their surroundings, the so-called wakefields, can lead to longitudinal and transverse instabilities, which limit the ultimate achievable beam current because, typically, they produces beam losses.
Among these instabilities, the coupled bunch (CB) instabilities are a serious issue in accelerators operated with multiple bunches at a high beam current.

This research focuses on the study of longitudinal CB instabilities in the CERN Proton Synchrotron (PS) in the framework of the LHC Injectors Upgrade (LIU) project. One of LIU goal is to double the beam intensity in the PS in order to achieve the integrated luminosity target of the High-Luminosity LHC. The CB oscillations induce longitudinal blow up and large bunch-to-bunch intensity and longitudinal variation, not compatible with the specifications of the future LHC-type beams. Up to present intensities (2014) they could be suppressed by a dedicated feedback system which used the 10 MHz cavities as longitudinal kicker, in addition to their function for acceleration. In the framework of the LIU project a new wide-band Finemet cavity has been installed in the PS in 2014 as a longitudinal kicker for a new digital coupled-bunch feedback system.

In Chapter 1 I will provide the theoretical background introducing the concepts of impedance, spectrum, wakefields and I will report in detail on the theory of longitudinal multi-particle beam dynamics.

In Chapter 2 I will present the PS Complex explaining its features, the operation of the cycle that leads to the production of the nominal beam for the LHC and I will describe the RF system involved in the preparation of the LHC nominal beam longitudinal structure. I will focus in particular on two RF systems: the 10 MHz accelerating system which is the main impedance source of CB instabilities and the

Finemet cavity, a part of the new coupled-bunch feedback (FB) system. For all these cavities, starting from machine measurements, I derived a simplified model used in simulations.

In Chapter 3 I will introduce the tools used for this research work: the simulation code MuSiC, the data acquisition techniques, and the analysis algorithm that I developed, based on the circulant matrix theory. I will also show simulations and measurements results to clarify the source of instability and to predict the beam performance after the upgrade implemented by the LIU project.

In Chapter 4 I will analyze in detail the new digital feedback system with all its components and the measurements carried out during its commissioning to confirm that the system interacts with the beam as expected. Finally I will present recent measurements results we obtained during 2016 machine run with the feedback contribute.

In the Conclusions I will give an overview of my research activity and draw conclusions on the current state of the art for CB instabilities in the CERN PS.

Chapter 1

Beam Dynamics in a Synchrotron

In this Chapter I will give an introduction to the accelerator physics basic equations. More details can be found on [1], [2], [3] and [4]. During the treatment of the subject numerous practical example referring to the parameter space of the CERN Proton Synchrotron (PS) will be used.

In 1943 M. Oliphant [5] conceived the synchrotron, a machine where the radius is fixed and all the fields can be confined only around the fixed orbit. A picture of the first machine is shown in Fig. 1.1. The invention of the synchrotron along with that of an efficient scheme for the transverse confinement of the particles during acceleration (alternate gradient focusing [6]) opened the way for the construction of large high energy synchrotrons. At that time a proton synchrotron (still in operation)

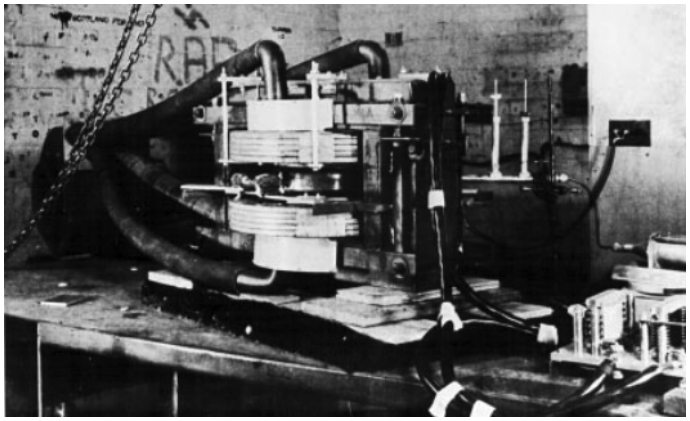

Figure 1.1. The world's first synchrotron, installed at Malvern [7].

was built: the CERN Proton Synchrotron (28 GeV, 1959) and in Fig. 1.2 we can see one of the first pictures taken during the construction. The main advantage of circular accelerators is that a single radio-frequency (RF) cavity, where the beam passes many times guided by the confinement action of magnetic fields, is capable of very high energy acceleration. This is a very efficient scheme where only a relatively small amount of RF power is required.

Figure 1.2. First PS combined magnet unit, with members of the Magnet Group [6].

Modern accelerators need to provide charged particle beams with an high current to achieve high intensity, and this presents several challenges in the development of these accelerators. Beam instabilities developing in transverse and longitudinal plane are one of the most important factors limiting the maximum attainable beam current. In this thesis we will focus on a specific family of longitudinal instability, *i.e.*, coupled-bunch (CB) instabilities.

1.1 The Single Particle Dynamics

The particles' motion is usually described in a reference frame co-moving with the synchronous particle (*i.e.*, with nominal momentum and therefore on nominal closed orbit) where it is possible to identify a transverse plane and a longitudinal one. Charged particles in a synchrotron are accelerated by electromagnetic (e.m.) fields, guided and confined by external electromagnetic forces and the motion of a single charge is governed by the Lorentz force [8]. The e.m. field inside RF cavities oscillates with the RF period T_{RF}. The harmonic number h is defined as the ratio between the revolution period, T_{rev}, and T_{RF}:

$$h = \frac{T_{rev}}{T_{\mathrm{RF}}} \tag{1.1}$$

with $T_{rev} = 2\pi/\omega_0$, $T_{RF} = 2\pi/\omega_r$, and ω_r, ω_{rev} the RF and revolution angular frequency respectively. In case of protons in the PS, the revolution frequency varies between $f_{rev} = 436$ kHz at injection and 477 kHz at extraction as shown in Fig. 1.3. In addition to the RF cavities, the circulating beam itself represents another source of e.m. fields that depends on the beam current, the geometry of the beam pipe and the surrounding materials: these fields are responsible of the so called beam instabilities. The underlying physical mechanism can be described as follow: the first bunch in a ring will induce electromagnetic fields in the cavity which oscillate and

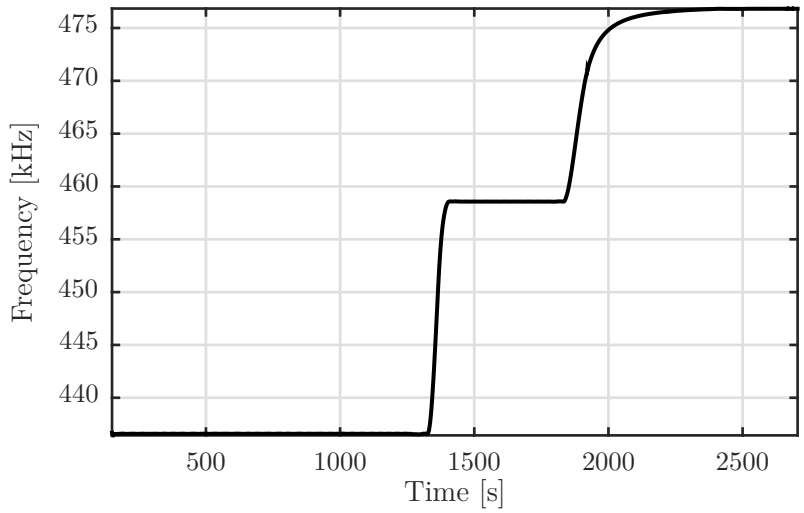

Figure 1.3. Measured revolution frequency in the PS cycle between machine injection and extraction.

then decay; the next bunch can experience some field left and it will be influenced by it. The phase of the field can be such to induce the increase of the synchrotron oscillation amplitude that can grows exponentially leading to instability. The e.m. fields induced by the beam are referred as wakefields due to the fact that they are left mainly behind the traveling charge. These fields interact with the beam leading to an instability or a change of the particle distribution. This kind of effect is usually known as collective effect since it is caused by a collective action of the many particles in the beam.
In the following Sections we show two different approaches to study the single particle dynamics: the Newtonian and the Hamiltonian mechanism. The Newtonian mechanics develops the equations of motion based on forces and acceleration as described by Newton's laws; the Hamiltonian mechanism is a refinement of the Lagrangian one, where the time derivatives of a system's coordinates are replaced by 'generalized momenta' (time derivatives of the system's Lagrangian).
The Newtonian and the Hamiltonian formulations are equivalent and any one can be derived from the other, but one or the other may be more convenient to use, depending on the system one needs to describe.

1.1.1 The Newtonian Formalism

Classical mechanics has not really changed since the days of Isaac Newton. The essence of Newton's insight, encoded in his second law $\mathbf{F} = \frac{dp}{dt}$, is that the motion of a particle described by its trajectory is completely determined if its initial position, velocity and $\mathbf{F}$ are known. His equation relates the acceleration to the force on the particle, which is implicitly assumed to depend only on the positions, and possible the velocities, of the particles in the system.

Consider a system with a particle with charge e passing through a cavity with an accelerating sinusoidal voltage $V_0 = V_{RF} \sin \phi_s$. The motion of the particle in the coordinate system momentum-phase (ϕ, p) is described by [9]:

$$\mathbf{F} = \frac{dp}{dt} = \frac{eV_{RF}}{2\pi R_s}(\sin\phi - \sin\phi_s) \tag{1.2}$$

$$\frac{d\phi}{dt} = -\frac{\eta h}{p_s}\frac{\beta_s c}{R_s}p \tag{1.3}$$

where $\eta = 1/\gamma_t^2 - 1/\gamma^2$ is the frequency slip factor, $\beta = v/c$, R_s is the average machine radius and p_s the momentum of the synchronous particle. Combining these two equations we obtain the equation of motion:

$$\frac{d^2\phi}{dt^2} + \frac{\Omega_{\text{synch}}^2}{\cos\phi_s}(\sin\phi - \sin\phi_s) = 0 \tag{1.4}$$

where:

$$\Omega_{\text{synch}} = \omega_s \sqrt{\frac{eV_{RF}h}{2\pi\beta^2 E_s}\,\eta\cos\phi_s} \tag{1.5}$$

From Eq. (1.4) is possible to obtain the expression of the separatrix:

$$\frac{\dot{\phi}}{\Omega_{\text{synch}}} = \pm\sqrt{\frac{2}{\cos\phi_s}[\cos\phi + \phi\sin\phi_s - \cos(\pi - \phi_s) - (\pi - \phi_s)\sin\phi_s]}. \tag{1.6}$$

The phase space area enclosed by the separatrix is called the bucket [10].

1.1.2 The Hamiltonian Formalism

Although Newton's equation correctly describes the motion of a particle (or a system of particles), it is often convenient to adopt an equivalent formalism. For example, a particle may be restricted in its motion such that it follows the contours of a given surface, or that the forces that keep the particle on the surface are not easily expressible in Cartesian coordinates. Such occurrences make difficult to treat the problem with the Newtonian formalism since this requires the knowledge of all forces acting on the particles.
The fundamental idea of the Hamilton's approach to mechanics is to reformulate the equations of motion in terms of the dynamical variables that describe the degrees of freedom, and thereby to incorporate constraint forces into the definition of the degrees of freedom rather than explicitly including them as forces in Newton's second law. Although the method based on Hamilton's principle does not constitute itself a new physical theory, it is probably justified to say that it is more fundamental than Newton's equations. This is because Hamilton's principle can be applied to a much wider range of physical phenomena than Newton's theory. From the Hamiltonian function $H(\phi, W)$ [3]:

$$H(\phi, W) = eV_{RF}[\cos\phi - \cos\phi_s + (\pi - \phi_s)\sin\phi_s] - \frac{1}{4\pi}\frac{h\eta\beta_s c}{p_s\,R_s}\,W^2, \tag{1.7}$$

introducing a new convenient variable, $W = 2\pi\ R_s\ p$, it is possible to obtain the evolution over time of (ϕ, W) by simply differentiating the Hamiltonian. The two

variables (ϕ, W) are canonical since these equations of motion can be derived from a Hamiltonian $H(\phi, W, t)$:

$$\frac{d\phi}{dt} = \frac{dH}{dW}, \tag{1.8}$$

$$\frac{dW}{dt} = -\frac{dH}{d\phi}. \tag{1.9}$$

This process leads to the 1st order equations:

$$\frac{dW}{dt} = eV_{RF}(\sin\phi - \sin\phi_s) \tag{1.10}$$

$$\frac{d\phi}{dt} = -\frac{1}{2\pi}\frac{h\eta\beta_s c}{p_s\, R_s}W \tag{1.11}$$

The Hamiltonian plays the same role in Hamiltonian mechanics as does the force in Newtonian mechanics: it defines the dynamics of the system but using first-order equations, which has certain advantages concerning linear methods, stability analysis, etc...

Phase Space Reconstruction in the PS: the Tomography

By all this treatment it is clear that the Hamiltonian is the best way to treat the physics in the phase space as it allows us to determine the properties of the particles ensemble; now we want to give an interpretation and application of the Hamiltonian from the operational point of view. H can be plotted in phase-space to provide a visual representation of the system's behavior. One of the benefits of phase-space dynamics is that every point on the phase-space plot represents the complete physical state of the system under consideration. In this discussion the phase-space coordinates will be expressed in energy and time [MeV,ns] to remain consistent with the type of information we acquire with the beam instrumentation during measurements in the PS . An example of measured phase space, as taken from the tomoscope (developed by S. Hancock at CERN [11]), is visible in Fig. 1.4. The underlying principle of tomography is to combine the information in a sufficiently large number of profiles to be able to reconstruct the picture with the extra dimension reinstated. On each turn, a longitudinal pick-up provides a "snapshot" of the bunch projected at a slightly different angle of its longitudinal phase space rotation. The acquisition of multiple profiles of the same bunch, each separated by a few machine turns, is achieved with the tomoscope application program. Longitudinal phase space tomography takes into account the non-linearity of synchrotron motion by tracking test particles in order to build maps which describe the evolution of phase space. The maps are used to reconstruct iteratively a two-dimensional density distribution whose projections converge towards the measured bunch profiles. In short, the Tomoscope allows the user to acquire a series of digitized bunch profiles from which a two-dimensional picture of how longitudinal phase space is populated inside the bunch can be generated. The energy distribution of the particles is reconstituted from the measured bunch shape information.
In Fig. 1.4 the largest plot is the two-dimensional histogram of the contents of phase space with the bucket separatrix shown in blue. The associated color scale

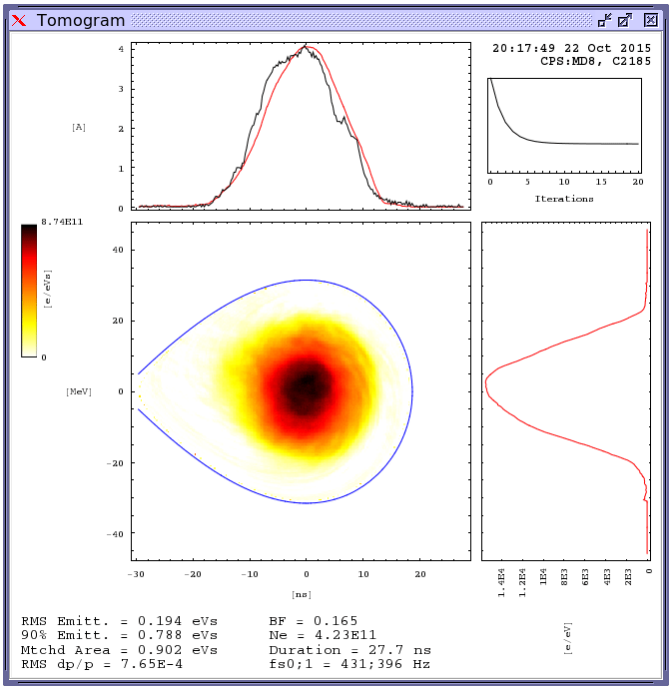

Figure 1.4. Phase space reconstruction as from the CERN Tomoscope.

appears to the left and the peak charge density within the bunch is quantified. The statistical properties of the distribution are summarized in a couple of beam parameters which appear below the plots: the σ emittance ("RMS Emitt.") and the $\Delta p/p$ relative momentum half-width ("Mom. Spread "), both rms calculations that are weighted by the individual pixel contents. The two orthogonal projections of the phase space distribution are plotted in red. The integral under these curves – and under the two-dimensional surface – is the same as that under the measured profile corresponding to the reconstruction time. The integral ("Ne ") and the bunching factor ("BF ") of this measured profile are listed with the other beam parameters. The area ("Matched Area") inside the matched phase space contour passing through both the resultant foot-tangent points is also listed. Numerical integration around this contour yields the synchrotron frequency ("fs1") at the edge of the bunch. The synchrotron frequency ("fs0 ") at the center of the bucket is also calculated. Finally, in the top right-hand corner, a small plot gives a qualitative idea of how well the iterations of the reconstruction algorithm converged.

1.2 Beam Spectra

Usually bunches do not have a default profile and it has to be chosen how to fit it, meaning with gaussian or parabolic profiles. In the case of the PS, as shown in Fig. 1.5, the assumption of a gaussian shape is more than acceptable and this will be the basic assumptions throughout this discussion.

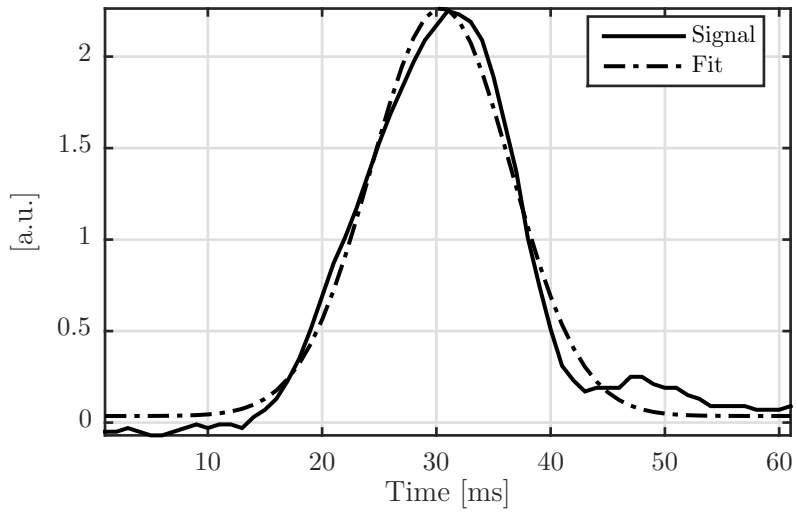

Figure 1.5. Plot of a measured bunch longitudinal profile and corresponding Gaussian fit.

We want to give details about the beam signal and spectrum as they will be useful in the following sections to fully understand the interaction of the beam with the machine impedance.
We will investigate three main conditions related to the type of bunch motion: the spectrum of a single bunch for a single-passage, the spectrum of multiple bunches for multi-passage and finally the spectrum of multiple bunches in case of multi-passage and synchrotron oscillations [3].

Spectrum of a Single Bunch and Single-Passage. Consider a point bunch circulating in the accelerator without synchrotron oscillation; it can be represented by a current $I(t)$:

$$I(t) = \sum_{k=-\infty}^{\infty} \delta(t - kT_0) \tag{1.12}$$

where the summation is over all revolutions. The frequency spectrum of the signal, obtained by a Fourier transformation, is:

$$\tilde{I}(t) = \omega_0 \sum_{p} \delta(\omega - p\omega_0) \tag{1.13}$$

Both the beam signal and beam spectrum are shown schematically in Fig. 1.6. The frequency content of the beam signal is therefore a series of δ-functions at $\omega = p\omega_0$.

Spectrum of Multiple Bunches and Multi-Passage. We now consider a stationary bunch which passes repetitively, with period T_0, at a given location in case of no synchrotron oscillations. Real beams have a longitudinal distribution of charge whose total signal is the sum over the individual charges. If we consider

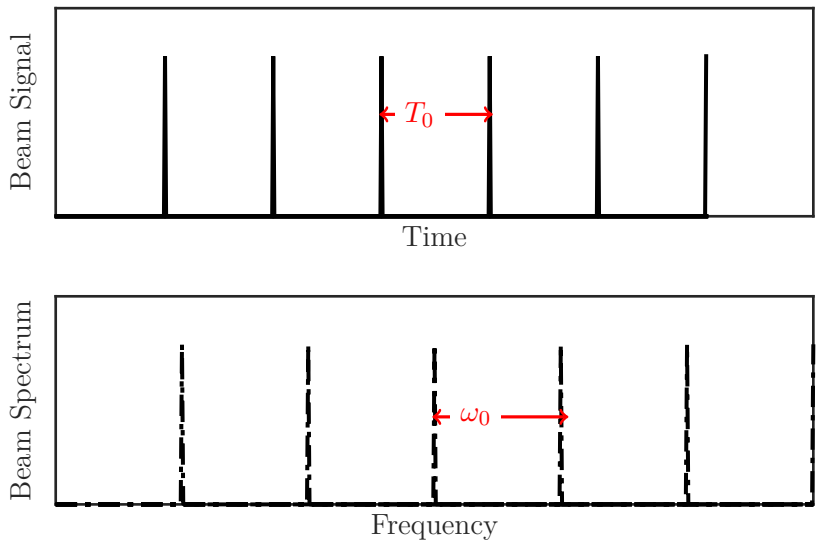

Figure 1.6. Signal of a point charge beam (above) and its spectrum (below) in case of a single bunch for a single-passage.

a bunch with a longitudinal distribution $\rho(t)$, the total signal is the sum over the single particle current and can be expressed as:

$$I(t) = \sum_{k=-\infty}^{\infty} I(t - kT_0) = I \otimes \sum \delta(t - kT_0) \tag{1.14}$$

where $\otimes$ represents the convolution operator. The signal in frequency domain is a comb of rotation harmonics with an envelope determined by the FFT of the longitudinal distribution $\tilde{\rho}(\omega)$:

$$\tilde{I}(t) = \omega_0 \, \tilde{I}_\omega \, \tilde{\rho}(\omega) \sum_p \delta(\omega - p\omega_0) \tag{1.15}$$

The beam spectrum still consists of a series of δ-functions at frequencies $\omega = p\omega_0$, but the strength of those δ-functions now contain an extra form factor given by the beam longitudinal distribution. The beam signal and the corresponding spectrum are shown in Fig. 1.7.

Spectrum of Multiple Bunches in case of Multi-Passage and Synchrotron Oscillations. If the bunch executes synchrotron oscillations with frequency $\omega_s = \omega_0 Q_s$ (usually we assume that the oscillation frequency is small compared to the revolution frequency $Q_s << 1$), this cause a modulation of its passage time t_k at a cavity in successive turns k as shown in Fig. 1.8:

$$t_k = kT_0 + \tau_k \tag{1.16}$$

with:

$$\tau_k = \hat{\tau} cos(2\pi Q_s k) \tag{1.17}$$

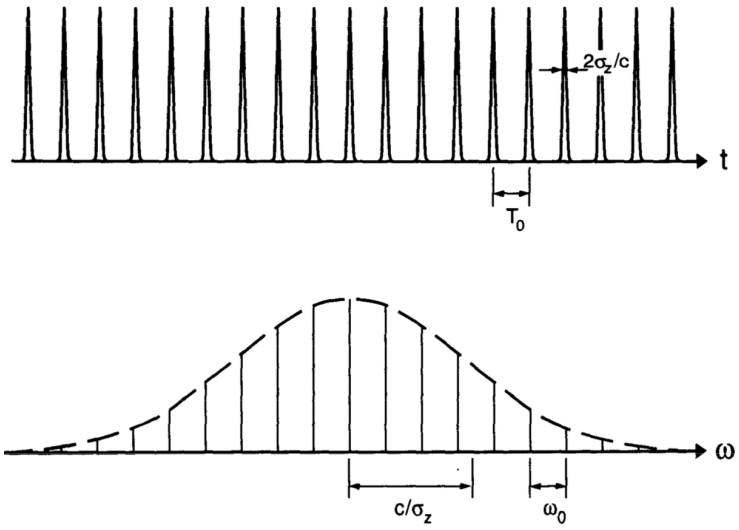

Figure 1.7. Signal of a Gaussian beam. The spectrum of the Gaussian beam consists of a series of δ-functions with an additional form factor [3].

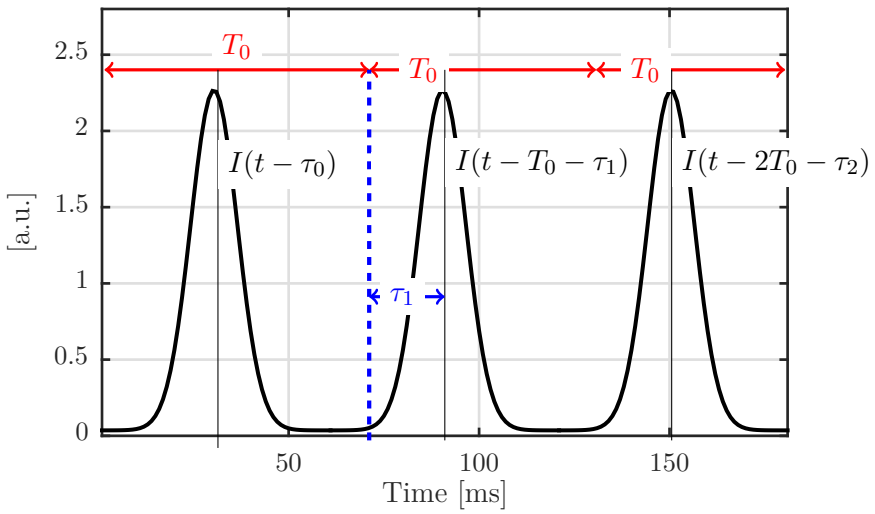

Figure 1.8. Plot of the longitudinal profile of a bunch passing multiple times at a given location and performing synchrotron oscillations.

with k the revolution number and $\hat{\tau}$ the amplitude of the modulation. It is possible to express the current in time domain as:

$$I(t) = \sum_{k=-\infty}^{+\infty} I(t - kT_0 - \tau_k) \tag{1.18}$$

In the approximation that the oscillations are small, it is possible to express the Fourier transform of the bunch current:

$$\tilde{I}(\omega) = \omega_0 \tilde{I}_\omega \left[\sum_{p=-\infty}^{\infty} \delta(\omega - p\omega_0) - j\frac{\omega\hat{\tau}}{2} \sum_{p=-\infty}^{\infty} \delta(\omega - p\omega_0 \pm \omega_s) \right] \tag{1.19}$$

Eq. (1.19) can be rewritten as:

$$\tilde{I}_k(\omega) = \omega_0 \tilde{I}_\omega \sum_m j^{-m} \; J_m(\omega\hat{\tau}) \; \sum_p \delta(\omega - p\omega_0 \pm \omega_s) \tag{1.20}$$

where J_m are the m-th order Bessel functions.

In this configuration the comb spectrum has sidebands at multiples of the synchrotron frequency which are contained within the Bessel function envelopes, as shown in Fig. 1.9. The sidebands are very similar to phase or frequency modulation sidebands on a carrier signal. Since the time modulation of the signal does not affect the total signal power, signal at the sideband frequencies comes from the signal at the rotation harmonics.

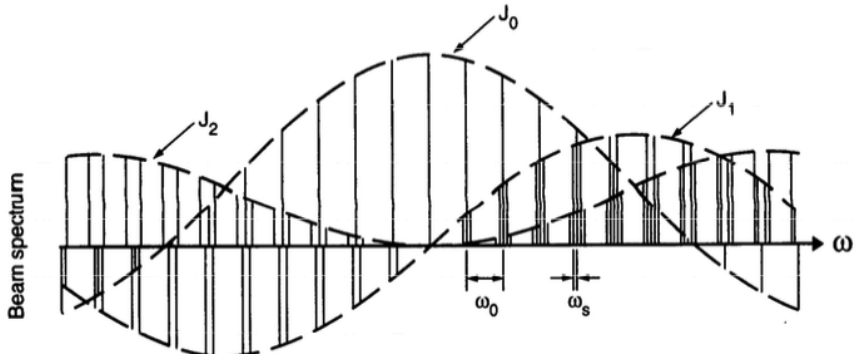

Figure 1.9. Spectrum of a point charge beam which is synchrotron oscillating. Around each $p\omega_0$ there are the sideband spaced by ω_s which have strength proportional to $J_m(\omega\hat{\tau})$.

Revolution harmonics follow $J_0(\omega\hat{\tau})$, while the first order sideband follow $J_1(\omega\hat{\tau})$. The current of the bunch is represented by spectral lines at harmonics of the revolution frequency $p\omega_0$ due to the stationary bunch motion while the sidebands are located at $p\omega_0 \pm \omega_s$ due to the modulation of the passage time with the synchrotron frequency.

1.3 Collective Effects

The collective effects are a class of phenomena in beam dynamics in which the evolution of a particle in a beam depends on both the external e.m. fields and the

extra e.m. fields created by the presence of other particles. Collective effects start playing a role when the beam density is very high (they are also referred to as “high current”, “high intensity” or “high brightness” effects).
In the frame of the LIU project, which aims to an upgrade of all the LHC injectors, in the PS it is expected an increase of the beam intensity of a factor 2. In this frame

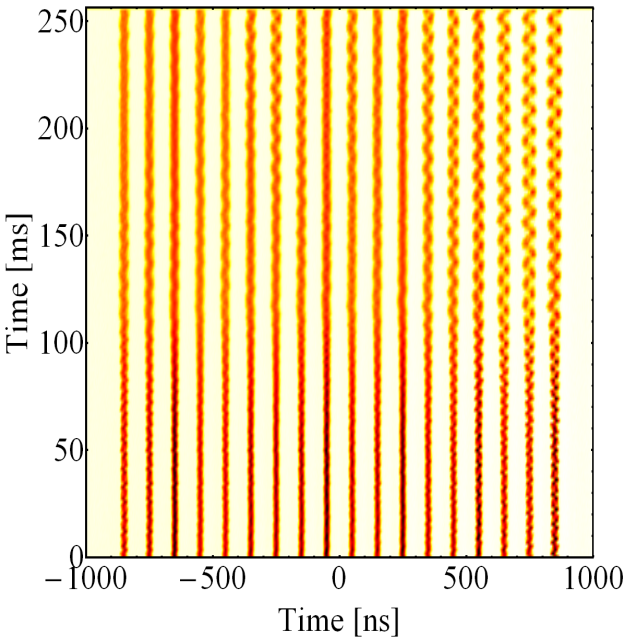

Figure 1.10. Measured bunch longitudinal oscillation observed during acceleration in the PS.

one family of collective effects, called coupled-bunch (CB) instabilities, driven by RF cavities, are considered one of the main problem in order to achieve the expected luminosity. In Fig. 1.10 we can see a typical measurements from the tomoscope: the longitudinal evolution at the flat-top along 250 ms of 18 bunches in 1 T_{rev} performing dipolar CB oscillations. In the big family of collective effects we can acknowledge three different situation.

In the first case we consider a particle of charge q, moving with constant velocity v, and interacting with the walls of a beam pipe; if the walls are far from the particles, the force which arises from the interaction, in first approximation can be neglected.

In the second case we consider a leading particle of charge q moving with velocity v, and a trailing particle q_1 of unit charge moving behind the leading one on a parallel path. In the limit of ultra relativistic particles moving parallel to each other, the electromagnetic interaction in free space vanishes.

In the third case we consider that the particles from the above example move parallel to the axis in a perfectly conducting cylindrical pipe of arbitrary cross section, they induce image charges, on the surface of the wall that screens the metal from

the electromagnetic field of the particles. The image charges travel with the same velocity v. Since both the particles and the image charges move on parallel paths

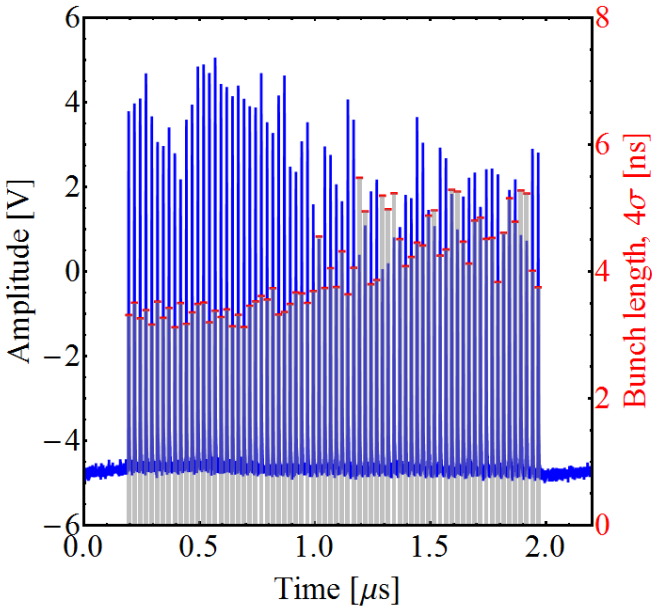

Figure 1.11. Beam longitudinal profile at last PS turn before extraction, FB OFF.

in the same direction, in the limit $v = c$, they do not interact with each other, no matter how close to the wall the particles are. Interaction between the particles in the ultra relativistic limit can occur if 1) the wall is not perfectly conducting, or 2) the pipe has discontinuities (which is usually due to the presence of RF cavities, flanges, bellows, beam position monitors, slots, etc., in the vacuum chamber).

So far we have dealt with the case of two charges, but given the linearity of the problem, we will extend the discussion to a beam which can be represented as a current that induces electromagnetic fields in the beam pipe and gives rise to image or wall currents of the same magnitude but opposite sign to the beam current, since the beam pipe itself is a conductor. The vacuum chamber where the charges are moving, has a finite conductivity and, moreover, changes its shape, cross-section, etc. along the beam path, and therefore presents an impedance to this wall current. Thus the wall current induces a voltage which gives rise to a longitudinal electric field, which may act back (accelerating or decelerating) on the bunch. Whilst the voltage is proportional to the wall current and thus to the beam current: instabilities are intensity dependent.

Since instabilities are intensity dependent, an increase of the demand of beam intensity would make them a very serious issue to be taken into account: this is the situation we are dealing with in the PS. CB instabilities in fact introduce two

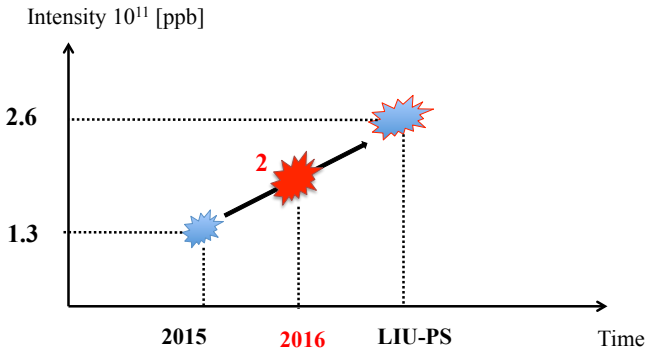

Figure 1.12. PS intensity trend: starting parameter, achievement and LIU PS requirement.

types of limitations in the production of the LHC type-beam which are summarized in Fig. 1.11 where is represented the longitudinal profile of 72 bunches at the last machine turn before extraction towards the SPS. On the y-axes are represented on the left the bunch amplitude and on the right the measured bunch length (indicated with red dots). The limitations introduced by CB instabilities are:

- **SPS bunch length limitation**: CB instabilities do not allow to reach the conditions required in terms of bunch length ($\sim$ 4 ns at extraction) to be compatible with the bucket of the SPS (200 MHz RF system); we can see in Fig. 1.11 that the bunches have different bunch lengths and the values are above the allowed threshold.
- **LHC intensity limitation**: CB oscillations prevent the smooth application of RF gymnastics (see Chapter 2 for details) in the PS and cause a reduction and a non equal splitting of the intensity between all the bunches at the last machine turn.

In Fig. 1.12 the trend of intensity in the PS during years is shown: in 2015 before the shutdown the PS was able to provide at extraction an intensity of $1.3 \cdot 10^{11}$ ppb; during 2016 it was possible to reach $2 \cdot 10^{11}$ following the installation of the CB feedback system to damp all the CB unstable modes. Detailed information concerning the project and the goals will be illustrated in Chapter2.

As highlighted the beam coherent motion becomes unstable for a certain beam intensity, which is the maximum that a machine can accelerate (performance limitation). Understanding the type of instability limiting the performance, and its underlying mechanism, is essential because it allows the identification of the source and the possible measures to mitigate or suppress the effect: this is what we are going to do in this thesis document.

1.3.1 Longitudinal Wake Function and Loss Factor

Let us refer to the configuration of Fig. 1.13, and consider a source charge q_1 traveling with constant velocity $\nu = \beta c$ on a trajectory parallel to the axis of a vacuum chamber

[12]. Let z_1 be the longitudinal position and r_1 the transverse vector positions. Let us assume that we solved Maxwell's equation [13] and found the electromagnetic field generated by the first particle. The Lorentz force acting on the charge q at a

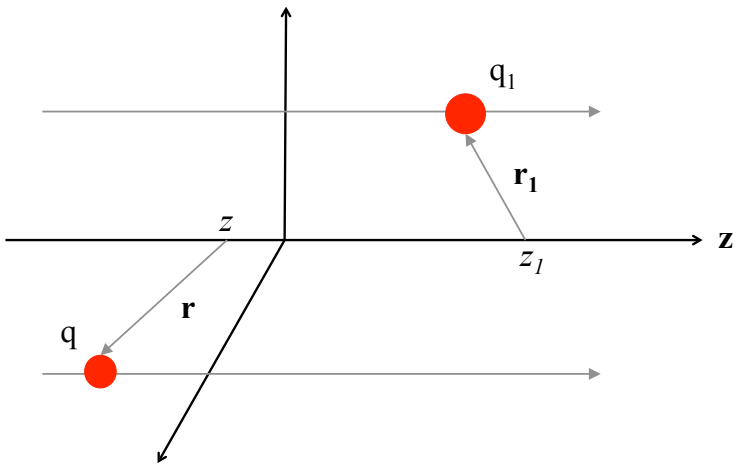

Figure 1.13. Reference system with a leading particle and a trailing one move parallel to each other in a vacuum chamber.

given position $(\mathbf{r}, z)$ is given by [12]:

$$\mathbf{F}(\mathbf{r}, z, \mathbf{r_1}, z_1; t) = q[\mathbf{E}(\mathbf{r}, z, \mathbf{r_1}, z_1; t) + \nu \times \mathbf{B}(\mathbf{r}, z, \mathbf{r_1}, z_1; t)] \tag{1.21}$$

Two are the effects on the test charge: a longitudinal force, which changes its energy, and a transverse force, which deflects its trajectory. Calling τ the time delay of the trailing charge with respect to the leading one, at any instant t the leading and trailing charges have longitudinal coordinates $z_1(t) = \nu t$ and $z(t) = \nu(t - \tau)$ respectively.
The energy lost by the charge q_1 is computed as the work done by the longitudinal e.m. force along the structure:

$$U_{11}(\mathbf{r_1}) = -\int_{-\infty}^{\infty} \mathbf{F}(\mathbf{r_1}, z_1, \mathbf{r_1}, z_1; t) \cdot d\mathbf{z}; \tag{1.22}$$

with $t = z_1/\nu$. The quantity U_{11} represents the energy loss in the resistive walls and in the diffracted fields radiated caused by the discontinuities of the vacuum pipe. The trailing charge also changes its energy under the effect of the fields produced by the leading one:

$$U_{21}(\mathbf{r}, \mathbf{r_1}, \tau) = -\int_{-\infty}^{\infty} \mathbf{F}(\mathbf{r}, z, \mathbf{r_1}, z_1; t) \cdot d\mathbf{z}. \tag{1.23}$$

with $t = z_1/\nu + \tau$. The quantity U_{21} depending on the time delay τ can be positive (energy loss) or negative (energy gain).
The longitudinal loss factor is defined as the energy lost by q_1 per unit charge squared:

$$k(\mathbf{r_1}) = \frac{U_{11}(\mathbf{r_1})}{q_1^2} \ [V/C]. \tag{1.24}$$

From U_{21} in Eq. (1.23) it is possible to derive the longitudinal wake function, defined as the energy lost by the trailing charge q per unit of both charges q_1 and q:

$$w_z(\mathbf{r}, \mathbf{r_1}; \tau) = \frac{U_{21}(\mathbf{r}, \mathbf{r_1}; \tau)}{q_1 q}, \quad [V/C]. \tag{1.25}$$

The wake function describes the impulse response of the vacuum chamber environment to a δ-function beam. Mathematically it resembles a Green's function. In general, the wake functions are solely determined by the properties of the vacuum chamber environment; they are independent of the beam properties.
The wake function, defined in Eq. (1.25), allows to compute the wake produced by any bunch distribution. Let us consider now a bunch of particles moving on a trajectory parallel to the axis, at a distance r_1, with a longitudinal time distribution function $i_b(\tau)$ such that:

$$q_1 = \int_{-\infty}^{\infty} i_b(\tau) d\tau \tag{1.26}$$

The wake function produced by the bunch distribution at a point with the time delay τ is simply given by the convolution of the Green function over the bunch distribution [12]. The wake function of a bunch distribution is defined as:

$$W(\mathbf{r}, \tau) = \frac{U(\mathbf{r}, \tau)}{q_1 q} = \frac{1}{q_1} \int_{-\infty}^{\infty} i_b(\tau`) w_z(\mathbf{r}, \tau - \tau`) d\tau` \tag{1.27}$$

An Application: the Loss Factor for the Finemet Cavity

One requirement in an accelerator is to avoid any kind of coherent instability that may cause beam losses. One of these instabilities is related to beam-environment interaction by means of the longitudinal coupling impedance and loss factor. In particular the concept of loss factor was useful to characterize the performance of the new damper cavity for the longitudinal feedback (FB) system.

Let us consider a resonant RF cavity inserted in a vacuum chamber and excited by a charged particle beam whose current is supposed to be frequency modulated. The definition of loss factor has been already introduced in Eq. (1.24), but in this practical context we want to propose a different operative definition. The study of the loss factor was applied to the longitudinal Finemet damper cavity. From simulations we observed the offset of the stable bunch with respect to the cavity; from comparison between simulations and theory we also evaluated the energy balance due to the impedance obtaining the beam power dissipated on the cavity. It is possible to compute the power dissipated by N_b equispaced bunches by [14]:

$$P = I^2 \sum_n \mathrm{Re}[Z(N_b n \omega_0)] \left| S(N_b n \omega_0) \right|^2 \tag{1.28}$$

where $\left| S(N_b n \omega_0) \right|^2$ is the single bunch spectrum. I is defined as

$$I = \frac{N_b N_p e}{T_0}. \tag{1.29}$$

The energy lost by a single bunch in one turn is given by

$$U_b = \frac{P}{N_b} T_0 \tag{1.30}$$

By substituting we obtain

$$U_b = \frac{N_b}{T_0} (N_p e)^2 \sum_n \mathrm{Re}[Z(N_b n \omega_0)] \, |S(N_b n \omega_0)|^2 \, . \tag{1.31}$$

The loss factor can be then defined as

$$k_e = \frac{N_b}{T_0} \sum_n \mathrm{Re}[Z(N_b n \omega_0)] \, |S(N_b n \omega_0)|^2 \tag{1.32}$$

since:

$$U_b = (N_p e)^2 k_e \;\Rightarrow\; U_w = N_p e k_e \tag{1.33}$$

where U_w is the energy lost by the single charge in the bunch, due to the wake effect. It is possible to evaluate the loss factor k_e starting from the shift of the synchronous phase by observing the bunches motion in simulations. In fact, as we will see in Chapter 3, the simulation code MuSiC tracks the bunches motion giving, turn after turn, information regarding the phase and longitudinal position of each bunch. The synchronous phase shift as in the simulation code is defined as:

$$\Delta\phi = -\frac{U_w}{V_{RF} \; sin(\phi_{s0})} \tag{1.34}$$

leading to the following definition of loss factor:

$$k_e = -\frac{\Delta\phi \, V_{RF}}{N_p e} \tag{1.35}$$

Through the evaluation of the synchronous phase shift, from Eq. (1.35) it is possible to evaluate the loss factor and, using Eq. (1.33) get the energy lost and compare it with the theoretical one in Eq. (1.31).
Several beam configurations *i.e.*, number of bunches and position along the cycle, were taken into account to evaluate the power loss, to ensure that during the entire period of activity the Finemet works in extremely reasonable conditions; different bunch lengths have also been taken into account to make the analysis comprehensive and a total current of $\sim$ 1.5 A has been used as well as the intensity provided by the LIU Project Upgrade of $2.6\,10^{11}$ ppb. In fact the main goal of the study was to determine whether the Finemet cavity would have problems in the interaction with the high intensity beam.
Tab. I summarizes the results obtained for the loss factor in our study. Theory and simulations gave consistent results regarding the loss factor; the average power dissipated by the beam on the cavity is harmless. These results, presented during the Finemet Review in 2014 [15] to external referees, have been considered extremely acceptable for the operation of the Finemet cavity as longitudinal damper [15].

Table I. Loss Factor for six cells of the Finemet cavity.

Settings	$\Delta\phi$ [rad]	k_e Sim. [V/C]	k_e Theor. [V/C]	Av. Power [kW]
$h = 21$, $\sigma_z = 0$ m	0.041	$4.3 \cdot 10^{10}$	$4.2 \cdot 10^{10}$	$\sim$ 10.2
$h = 21$, $\sigma_z = 2$ m	0.017	$1.8 \cdot 10^{10}$		$\sim$ 4.3
$h = 84$, $\sigma_z = 0$ m	0.0087	$3.3 \cdot 10^{10}$	$3.4 \cdot 10^{10}$	$\sim$ 2.15

1.3.2 Longitudinal Coupling Impedance

Historically, the coupling impedance concept was introduced in the early studies of the instabilities arising in the ISR at CERN [16]. The coupling impedance and wake function are the description of the same physical phenomenon and they are used to convey the complementary information in the frequency domain and time domain, respectively. The idea of representing the accelerator environment by an impedance was introduced by Sessler and Vaccaro [17]. On this subject we address to [18] where a more exhaustive review on the subject is presented.

In the frequency domain we compute the spectrum of the point charge wake function as [12]:

$$\int_{-\infty}^{\infty} w_z(\mathbf{r}, \mathbf{r_1}; \tau) e^{-j\omega\tau} d\tau \equiv Z(\mathbf{r}, \mathbf{r_1}; \omega) \tag{1.36}$$

this quantity, measured in Ohms units, is called coupling impedance. The wake function is derived from the impedance by inverting the Fourier integral:

$$w_z(\mathbf{r}, \mathbf{r_1}; \tau) = \frac{1}{2\pi} \int_{-\infty}^{\infty} Z(\mathbf{r}, \mathbf{r_1}; \omega) e^{j\omega\tau} d\omega \tag{1.37}$$

Numerous texts and references refer to the impedance and wake with different symbols, but in this context, to lighten the discussion, we will refer to the impedance and to the longitudinal wake with symbols Z and W respectively. Since the wake function is the impulse response of the beam environment, the beam impedance is the transfer function from the beam current to the wake voltage.
The coupling impedance is a complex quantity:

$$Z(\omega) = Z_r(\omega) + jZ_i(\omega) \tag{1.38}$$

with $Z_r(\omega)$ and $Z_i(\omega)$ even and odd function of ω respectively. There are several important properties that characterize the impedance, below we will just illustrate a couple.

The first property is related to the Panofsky-Wenzel theorem [19], and correlates the longitudinal wake function to the derivative of the transverse wake function, giving a relationship between the longitudinal and transverse impedances:

$$Z_\perp(\mathbf{r}, \mathbf{r_1}; \omega) = \frac{c}{\omega} \nabla_\perp Z(\mathbf{r}, \mathbf{r_1}; \omega) \ \ [\Omega] \tag{1.39}$$

The second property follows from the Cauchy theorem and states that the real and imaginary parts of the impedance must be related by the Hilbert transform [20]:

$$\int_{-\infty}^{\infty} Z_r(\omega) cos(\omega\tau) d\omega = \int_{-\infty}^{\infty} Z_i(\omega) sin(\omega\tau) d\omega \tag{1.40}$$

The coupling impedance defined by Eq. (1.36) behaves like a circuit impedance only when the causality principle applies, namely in the limit case of charges traveling with the velocity of light. Eq. (1.40) indicates that, knowing the real or the imaginary part, it is possible to reconstruct the whole impedance and then the entire wake turn after turn. The impedance of an RF cavity can be modeled as an RLC

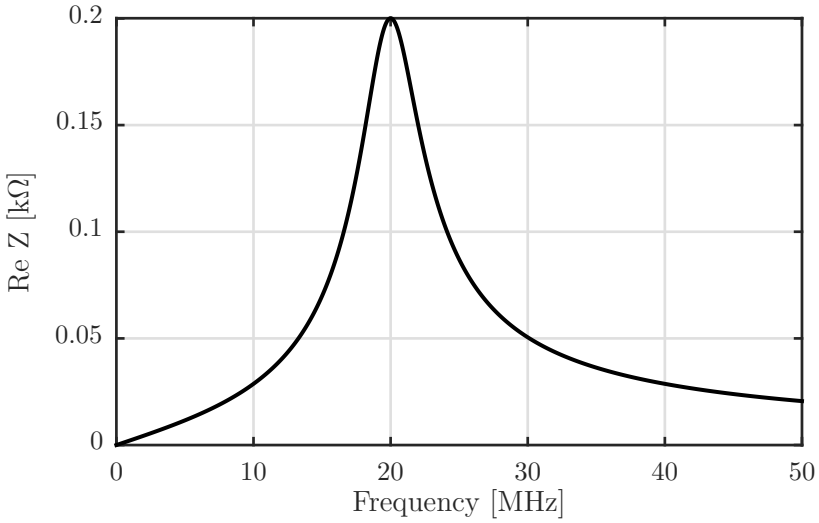

Figure 1.14. Real part of the impedance of a 20 MHz cavity in the PS.

(resistor-inductor-capacitor) band pass filter, with a longitudinal impedance given by:

$$Z = \frac{R_s}{1 + iQ(\frac{\omega_R}{\omega} - \frac{\omega}{\omega_R})}, \tag{1.41}$$

with $Q = R_s\sqrt{C/L}$ is the quality factor and $\omega_R = 1/\sqrt{LC}$ is the resonant frequency. In Fig. 1.14 is shown the real part of the impedance of one of the PS cavities. It can be modeled by using Eq. (1.41) with the following parameters: Q=4.6, R_s=200.1 Ω, ω_R=20 MHz. The corresponding wake function obtained by performing a Fourier transform of the impedance is plotted in Fig. 1.15. In Eq. (1.41) the quality factor Q determines the width of the impedance: if $Q >> 1$ the impedance is narrowband, while it is considered to be broadband if $Q \approx 1$. We want now to highlight the difference between broad-band and narrow-band impedance, notion that will be useful later in the impedance characterization of the different PS RF cavities.

Broadband Impedance

A broadband impedance corresponds to a wakefield with a short decay time, therefore a short effective range (shorter than a few RF bucket lengths). Typically this type of wakefield can only be seen by particles in the same bunch and does not affect particles in the trailing bunches. Therefore, the broadband wakefield can excite instabilities in a single bunch. A short-lived wake, decaying over the length of one bunch, can only cause intra-bunch coupling.

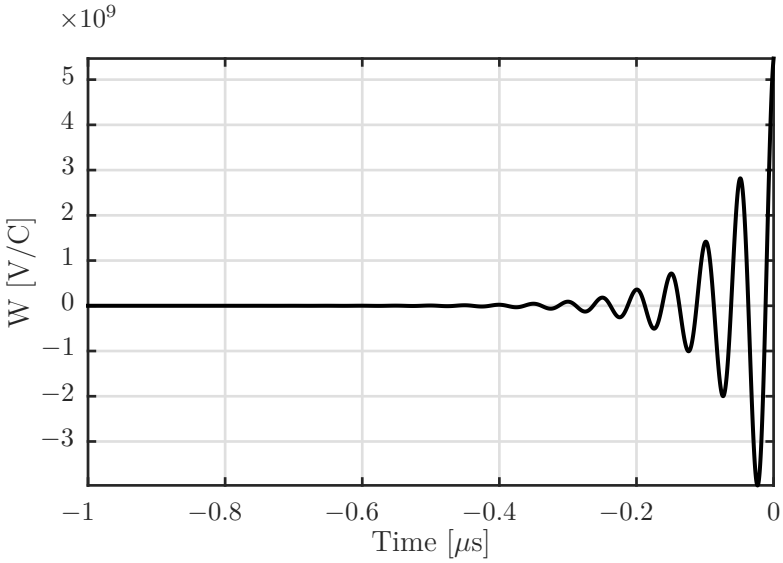

Figure 1.15. Wakefield obtained from impedance of Fig. 1.14

An example of broadband impedance is the one of the Finemet cavity, the new damper installed in the PS and designed to operate as longitudinal kicker of the feedback system. In Fig. 1.16, both measured real and imaginary part are shown. More details regarding the kicker cavity as well as all the other RF cavities will be given in the Chapter 2.

Narrow-band Impedance

A narrow-band impedance corresponds to a long range wake effect, which impacts bunches behind the source bunch. The narrow-band wakefield induces coupled-bunch motions between circulating bunches. This type of wakefield is usually excited inside an RF cavity and is dominated by high-Q resonant modes of the cavity itself, which appears as narrow peaks. A long-lived wake field decaying over the length of a train of bunches, or even several turns, causes bunch-to-bunch or multi-turn coupling. The decay time of the wake depends on how quickly the stored energy in these modes is dissipated (quantified by a quality factor Q). An example of narrow-band impedance in the PS are the 10 MHz cavities, responsible of exciting CB instabilities in the machine, that we are going to analyze in detail.

An application: The 10 MHz RF Cavities Impedance Model

Usually the knowledge of the machine impedance is established with electromagnetic simulations, theoretical computations and beam-based measurements. To build the impedance model of an accelerator it is necessary to evaluate the impedance of all the elements. The impedance model must then be bridged to beam dynamics studies. When studying the beam dynamics of the machine each wake is separately applied to the beam particles and the beam is then transported from one element to the

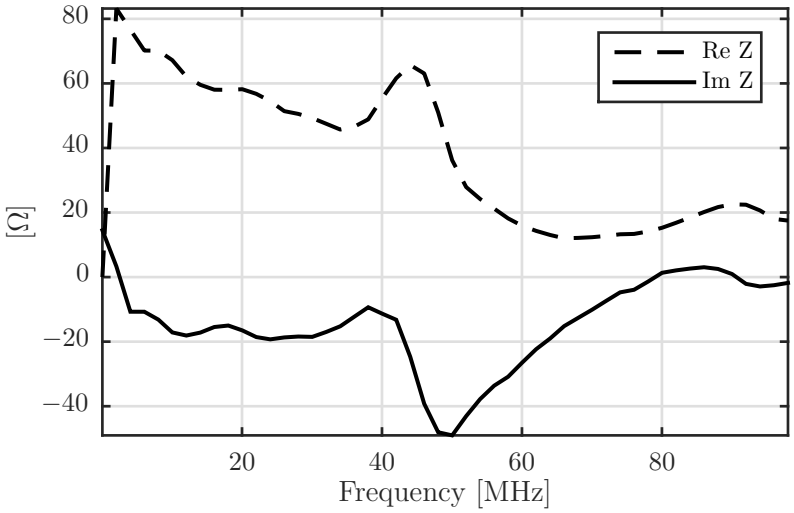

Figure 1.16. Measured real and imaginary part of the Finemet cavity longitudinal impedance.

next one with the correct phase advance. In most cases the impedance of devices can be modeled as the sum of several narrow- and broad-band resonator peaks.
In frequency domain, the cavity wakefields are described in terms of superposition of modes. Each mode can be specified by an equivalent LRC resonator impedance and wake function with its own mode frequency ω_R and R_S/Q as in Eq. (1.41). The superposition principle [21] states that a linear combination of solutions to a linear equation is again a solution, which, translated into our context, allows us to fit a generic impedance with a sum of resonant modes. In this way we do not need, as input, the wakefield, but, once we have the machine coupling impedance, we can fit it with a finite sum of different resonant modes. In principle there is no limit to the number of modes that can be used for the fit and Eq. (1.40) indicates that, knowing the real part of a coupling impedance, one can construct the imaginary part and vice versa; anyway this operation should be applied with care [3].
In this context the main purpose is to show how a single cavity impedance is manipulated to be used in the simulation code exploiting the theoretical formulation just presented. In Fig. 1.17 is shown the impedance of all the 10 MHz cavities which are used to for acceleration purpose (we refer to Chapter 2 for more details). In order to have a general model valid for all the 10 MHz cavities, we made a weighted average of the real part of the impedance for all the cavities and fitted it. A reasonable convergence has been found with 3 resonant modes:

$$Z(\omega) = \sum_{i=1}^{3} \frac{R_{Si}}{1 + iQ_i \left(\frac{\omega_{Ri}}{\omega} - \frac{\omega}{\omega_{Ri}} \right)} \tag{1.42}$$

In Tab. II are shown the values obtained from the fit and in Fig. 1.18 is represented the real part of the weighted impedance and its fit.

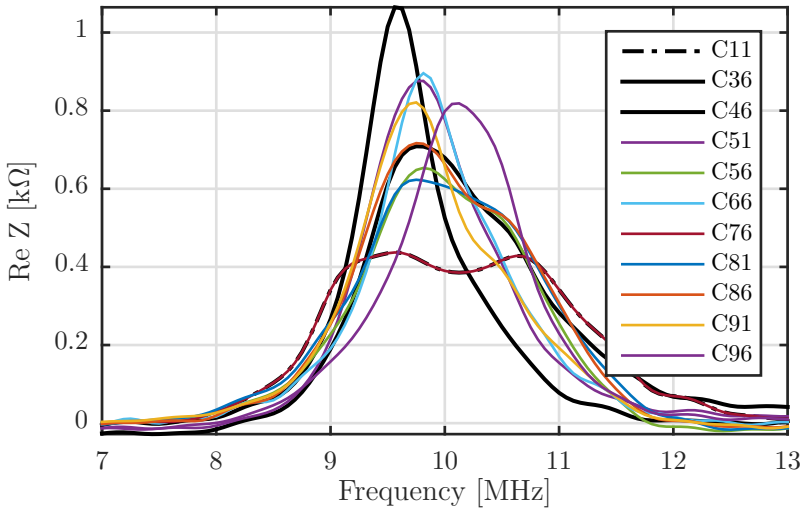

Figure 1.17. Measured real part of the longitudinal impedance of all the 10 MHz cavities in the PS.

Table II. 10 MHz cavities fit parameters .

Q	**R_S [kΩ]**	**f_{RF} [MHz]**
14	4	9.6
9.5	3.5	10
9	3.15	10.6

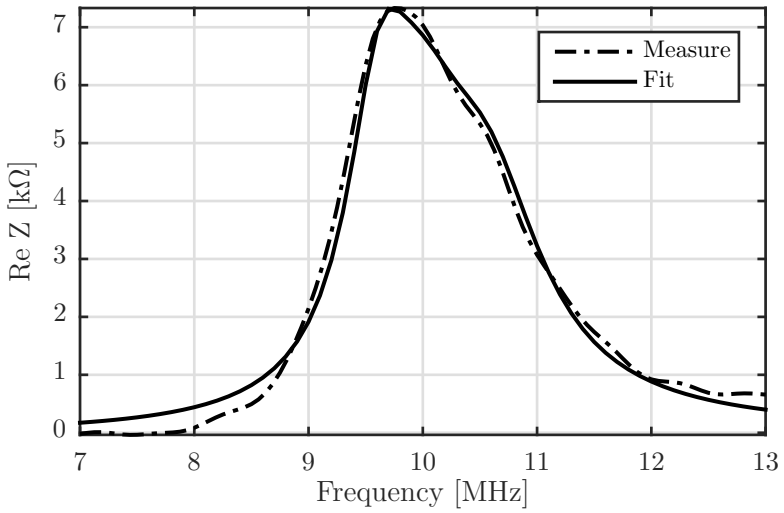

Figure 1.18. Measured real part of the total impedance of the 10 MHz cavities and its fit.

The same procedure was used to develop a simplified model for all the other PS cavities, as shown in Chapter 2. These models will be used within the simulation code to study the interaction between the beam and the machine impedance; simulations results will be presented in Chapter 3.

1.4 Beam Instabilities

A beam becomes unstable when its distribution exhibits an exponential growth resulting into beam loss or emittance growth. The onset of a beam instability usually determines the maximum beam intensity that a machine can store/accelerate. They can affect the beam on different scales:

- Single bunch effect
- Multi-bunch effects: cross-talk between bunches

We will propose an example for each category. We will first investigate the Robinson Instability which occurs for a single bunch under the action of a multi-turn field: it contains a term of coherent synchrotron tune shift and results into an unstable rigid bunch dipole oscillation. It does not involve higher order moments of the bunch longitudinal phase space distribution.
Then we will show the theory underlining the multi-bunch instability and we will propose an alternative approach to the classical one.

1.4.1 Single Bunch Case: The Robinson Instability

In this Section, we will discuss a particular type of long range longitudinal instability for a one particle beam, the Robinson Instability (RI). With this specific case we want to demonstrate how the concepts of spectrum and impedance introduced up to now may be used to describe beam instability.

The RF accelerating cavities in a circular accelerator are tuned so that the resonant frequency ω_R is very close to an integral multiple of the revolution frequency. The wake field excited by the beam in the cavities contains a major frequency component at $\omega_R \approx h\omega_0$. Above transition energy, the beam will be unstable if ω_R is above $h\omega_0$ and stable if below. This instability mechanism was first analyzed by Robinson [3]. We will recall briefly the RI mechanism.

From now on we will consider the phase space (z, δ). Let z be the longitudinal displacement of the beam in the accelerating RF cavity at the nth revolution. Introducing the external forcing factor of the field, the equation of motion can be written as [3]:

$$\frac{d^2 z_n}{dn^2} + (2\pi\nu_s)^2 z_n = \frac{N r_0 \eta C}{\gamma} \sum_{k=-\infty}^{n} W'(kC - nC + z_n - z_k) \tag{1.43}$$

with the usual parameters definitions. The summation over k is over the wake fields left behind by the beam from all previous revolutions to the nth. The argument of

the wake function is the longitudinal separation of beam positions between the nth and the kth revolution. Eq. (1.43) is a linear differential equation for z_n which can be solved in time domain but, transforming to the frequency domain simplifies the mathematics considerably. In the frequency domain z_n can be written as:

$$z_n \propto e^{-in\Omega T_0} \tag{1.44}$$

where Ω is the mode frequency of the beam oscillation. In Eq. (1.44) the term $e^{-i\Omega}$ represents the kernel of the Fourier transform, this means that it is possible to rewrite Eq. (1.43) as shown in Eq. (1.45) where two components can be identified: an algebric part and the Fourier Transform of the wake, that represents the coupling impedance. This implies that it is possible to switch from the differential equation to an algebric one as described in details in [3]. The new expression of the equation of motion is:

$$\Omega^2 - \omega_s^2 = -\frac{Nr_0\eta\ c}{\gamma T_0} \sum_{p=-\infty}^{\infty} [p\omega_0 Z^{||}(p\omega_0) - (p\omega_0 + \Omega) Z^{||}(p\omega_0 + \Omega)] \tag{1.45}$$

where $\omega_s = \nu_s\, \omega_0$ is the synchrotron frequency and the wake function is expressed in terms of the longitudinal impedance. In order to solve Eq. (1.45) it is necessary to take certain assumptions, as follows. Given the impedance, Eq. (1.45) can be solved for Ω. We assume a small deviation of Ω from the synchrotron tune and we can use the following approximation $\Omega^2 - \omega_s^2 \approx 2\omega_s \cdot (\Omega - \omega_s)$. In general, Ω is complex. The real part is the perturbed synchrotron oscillation frequency of the collective beam motion, and the imaginary part gives the growth rate (or damping rate if negative) of the motion. The solution of Eq. (1.45) can be decomposed in a mode frequency shift:

$$\Delta\Omega = \mathrm{Re}(\Omega - \omega_s) = \frac{Nr_0\eta}{2\gamma T_0^2 \omega_s} \sum_{p=-\infty}^{\infty} [p\omega_0\ \mathrm{Im}Z_0^{||}(p\omega_0) - (p\omega_0 + \omega_s)\ \mathrm{Im}Z_0^{||}(p\omega_0 + \omega_s)] \tag{1.46}$$

and an instability growth rate:

$$\tau^{-1} = \mathrm{Im}(\Omega - \omega_s) = \frac{Nr_0\eta}{2\gamma T_0^2 \omega_s} \sum_{p=-\infty}^{\infty} [(p\omega_0 + \omega_s)\ \mathrm{Re}Z_0^{||}(p\omega_0 + \omega_s)] \tag{1.47}$$

Consider now a resonator impedance of the form of Eq. (1.41). The only significant contributions to the growth rate τ^{-1} come from two terms in the summation, $p = \pm h$, assuming both the width of the impedance peak $\omega_r/2Q$, and the synchrotron frequency much less than ω_0. This gives:

$$\tau^{-1} \approx \frac{Nr_0\eta h\omega_0}{2\gamma T_0^2 \omega_s} [\mathrm{Re}\ Z_0^{||}(h\omega_0 + \omega_s)\ -\ \mathrm{Re}Z_0^{||}(h\omega_0 - \omega_s)] \tag{1.48}$$

Beam stability requires $\tau^{-1} \leq 0$. This condition implies the Robinson criteria that the resonant frequency ω_R of the fundamental cavity mode should be slightly detuned downwards from an exact integral multiple of ω_0 as we can observe in Fig. 1.19. When the Robinson criteria is met the synchrotron oscillation of the beam is damped and this damping will help in stabilizing the beam against similar instabilities due to other impedance sources.

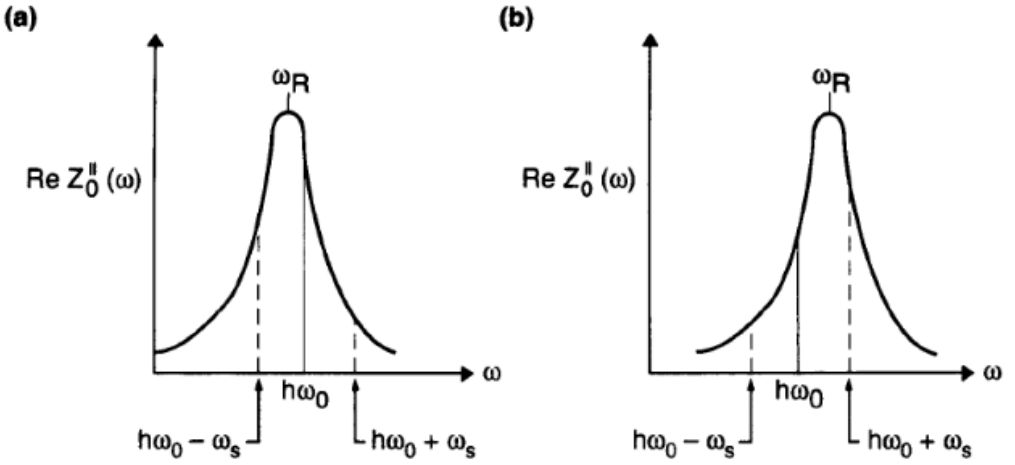

Figure 1.19. Representation of the Robinson instability criteria [3]. The RF fundamental mode is detuned so that ω_R is below (a) and above (b) $h\omega_0$. In the left figure (a) Robinson instability is damped above transition and antidamped below transition. The opposite happen in the right figure (b).

1.4.2 The Multibunch Theory

The presence of multiple bunches in a synchrotron has several interesting effects on the beam signal because of the possibility of coherent addition of signals from one bunch to another. Although the signals are the same as those in a single bunch beam, there are two effects. First, the rotation harmonic observed in the frequency domain can be significantly different in a multibunch beam, depending on the filling pattern. Secondly, the oscillations of bunches can be coupled via wakefields in resonant devices such as RF cavities, causing coherent oscillations of the beam which have a particular frequency signature in the beam signal. We now assume that the bunches are approximated as single particles and can only have dipole modes of oscillations.

The analysis that allowed to obtain the equation of motion in Eq. (1.45) can be generalized to the case of N_b equally spaced bunches, each containing a point charge. The equation of motion generalized for multiple bunches, can be rewritten as:

$$z_n''(s) + \left(\frac{\omega_{s0}}{c}\right) z_n(s) = \frac{N r_0 \eta}{\gamma C} \sum_k \sum_{m=0}^{N_b-1} W_0' \left[-kC - \frac{m-n}{N_b} C + z_n(s) - z_m\left(s - kC - \frac{m-n}{N_b} C\right)\right] \quad (1.49)$$

with $n = 0, 1, 2 \cdots, N_b - 1$, where ω_{s0} is the unperturbed synchrotron frequency. In this case of N_b equally spaced, equally populated bunches, there will be a total of N_b modes of the multibunch motion, each specified by and index μ which assumes the values $0, 1, \cdots, N_b - 1$. The amplitudes of the N_b multibunch modes is:

$$\tilde{z}_n \propto e^{2\pi i\, \mu n / N_b} \quad (1.50)$$

By redefining [3] the synchrotron frequency in terms of impedance as:

$$\Delta\omega_s \approx \frac{N_b\, N r_0 \eta}{2\gamma T_0^2 \omega_s} \sum_{p=-\infty}^{\infty} p N_b \omega_0 \,\mathrm{Im}\, Z_0^{\parallel}(p N_b \omega_0) \tag{1.51}$$

and using the same analysis of the Robinson Instability, from Eq. (1.49) it is possible to obtain the mode frequency:

$$\Omega^{(\mu)} - \omega_s = i\frac{N_b N r_0 \eta}{2\gamma T_0^2 \omega_s} \sum_{p=-\infty}^{\infty} (p N_b \omega_0 + \mu\omega_0 + \omega_s)\, Z_0^{\parallel}(p N_b \omega_0 + \mu\omega_0 + \omega_s) \tag{1.52}$$

When the fundamental RF cavity mode is peaked around $\omega_r = h\omega_0 + \Delta\omega$ (where the harmonic number h is necessarily a multiple of N_b for a multibunch operation, and $\Delta\omega$ is the amount of frequency detuning) the growth rate will be N_b times larger than the one found in Eq. (1.48).
The reason the impedance is evaluated at $\omega = pN_b\omega_0 + \mu\omega_0 + \omega_s$ can be understood below. Observed at a fixed location, the signal from a beam executing the multibunch mode is:

$$\text{beam signal} \propto \sum_k \sum_m z_n^{(\mu)}\, \delta\left(t - kT_0 + \frac{nT_0}{N_b}\right) \tag{1.53}$$

The spectrum of this signal is:

$$\text{spectrum} \propto \int dt\; e^{i\omega t}\,(\text{beam signal}) \tag{1.54}$$

$$= N_b\omega_0 \sum_{p=-\infty}^{\infty} \delta(\omega - pN_b\omega_0 - \mu\omega_0 - \omega_s) \tag{1.55}$$

The μth multibunch mode therefore samples the synchrotron sidebands of the frequencies

$$\omega_{cb} = (pN_b + \mu)\omega_0 + \omega_s \tag{1.56}$$

where $p = 0, \pm 1 \cdots \pm\infty$ and μ the mode number.

1.5 Matrix Approach to CB Instabilities

Until now we have dealt with and solved the problem of instability in the time domain. But in order to track precisely the particle's motion, matrices are a more suitable instrument given the symmetry of the system. The approach that we are going to describe allows to find the mode of the system no longer solving a differential equation. The forces due to beam coupling impedance are linear, therefore matrix formalism is appropriate to obtain the coherent spectrum in presence of wakefieds. The purpose of this section is to have a look into the theory of the circulant matrix showing that they are an appropriate tool to describe the beam evolution and interaction with the machine environment and to derive the modes of the system.

Circulant matrices belong to the class of Toeplitz matrices [22] with well known and derived properties [23], [24]. They arise, for example, in applications involving the

discrete Fourier transform (DFT) and the study of cyclic codes for error correction. Circulant matrices are a special class of matrices since inverses, products, and sums are also circulant matrices. A circulant matrix is a Toeplitz matrix with the additional property that $a_i = a_{i+n}$:

$$C = \begin{pmatrix} c_0 & c_{n-1} & c_{n-2} & ... & c_1 \\ . & . & . & . & . \\ . & . & . & . & . \\ . & . & . & . & . \\ c_{n-1} & c_{n-2} & ... & .. & c_0 \end{pmatrix}. \tag{1.57}$$

It is fully specified by one vector $\bar{c}$, the first column of C. The remaining columns are cyclic permutations of this vector with offset equal to the column index. The last row of C is the vector $\bar{c}$ in reverse order, and the remaining rows are each cyclic permutations of the last row.
The eigenvalues of such matrices can be found exactly and the same eigenvectors work for all circulant matrices. They are given by:

$$v_j = \frac{1}{\sqrt{n}}(1, \omega_j, {\omega_j}^2, ..., {\omega_j}^{n-1})^T \tag{1.58}$$

with $j = 0....n-1$ and where $\omega_j = e^{\frac{2\pi ij}{n}}$ are the n-th roots of unity and $i = \sqrt{-1}$ is the imaginary unit. The corresponding eigenvalues are then given by:

$$\lambda_j = c_0 + c_{n-1}\omega_j + c_{n-2}{\omega_j}^2 + ... + c_1{\omega_j}^{n-1} \tag{1.59}$$

Since the base of eigenvectors exists, then it is always possible to diagonalize the matrix.

1.5.1 Circulant Matrix Formalism

Any dynamic system can be described by a mathematical model which features its evolution in time, following rules that allows to bond the present and future state of the system in a deterministic way.
The evolution in the normalized longitudinal phase space of the bunches from turn n to turn $n+1$ can be linearly approximated by the following:

$$\begin{pmatrix} \tau_1 \\ \epsilon_1 \\ \cdots \\ \cdots \\ \tau_{N_b} \\ \epsilon N_b \end{pmatrix}_{n+1} = \mathbf{M} \times \begin{pmatrix} \tau_1 \\ \epsilon_1 \\ \cdots \\ \cdots \\ \tau_{N_b} \\ \epsilon_{N_b} \end{pmatrix}_{n}, \tag{1.60}$$

where M is a block circulant matrix where each block represents a rotation matrix. The matrix M can be considered a transformation matrix of the system since represents a linear transformation between vectorial space. Once M is known, the stability of the system in Eq. (1.60) can be investigated by its eigenvalues. Since we consider a perturbative approach, it is possible to assume that all the bunches in

the system have the same synchrotron tune Q_s. Therefore each bunch coordinate τ_i and ϵ_i can be written as:

$$\tau_i^{N_b} = \Re\left\{a_i e^{j\phi_i} \cdot e^{j2\pi Q_s \times n}\right\} \tag{1.61}$$

$$\epsilon_i^{N_b} = \Im\left\{a_i e^{j\phi_i} \cdot e^{j2\pi Q_s \times n}\right\} \tag{1.62}$$

where $i \in \{1, \ldots, N_b\}$, a_i and ϕ_i are the amplitude and the phase of the longitudinal bunch oscillation. The dynamic in Eq. (1.60) together with the assumption in Eq. (1.61) and Eq. (1.62) can be re-formulated in a complex amplitude space and described by the new variable $\mathbf{X_n}$:

$$\begin{pmatrix} X_1 \\ \cdot \\ \cdot \\ X_{N_b} \end{pmatrix}_{n+1} = \mathbf{X_{n+1}} = \mathbf{C} \times \begin{pmatrix} X_1 \\ \cdot \\ \cdot \\ X_{N_b} \end{pmatrix}_{n} = \mathbf{C} \times \mathbf{X_n} \tag{1.63}$$

where $X_i = a_i \cdot e^{j\phi_i}$ is the phasor representing the complex amplitude of the i^{th} bunch and C is a $N_b \times N_b$ complex circulant matrix.
As already pointed out, the eigenvectors of a circulant matrix are known from Eq. (1.58), and matrix C is diagonalizable if does exist an invertible matrix $\mathbf{P}$ such that:

$$\mathbf{C} = \mathbf{P} \times \mathbf{D} \times \mathbf{P}^{-1} \tag{1.64}$$

where $\mathbf{D}$ is a diagonal matrix of eigenvalues and $\mathbf{P}$ is the base of the eigenvectors of the system. Since $\mathbf{P}$ in invertible, the eigenvalues are independent and so they form a base in the space. It is known that [22]:

$$\mathbf{P} = \mathrm{DFT}(\mathbf{I}) \tag{1.65}$$

where I is the $N_b \times N_b$ identity matrix and DFT represents the Discrete Fourier Transform. From Eq. (1.65) follow:

$$\mathbf{PI} = \mathrm{DFT}(\mathbf{I}) \tag{1.66}$$

But, as for every system which it is subjected to a vibration / excitation, (see interaction beam-cavity), it is possible to study the dynamic behavior with the modal analysis, by evaluating the natural frequency of the different modes that are the eigenvectors of the system. It is possible to rewrite the evolution of Eq. (1.63) from the bunch space $\mathbf{X_n}$ in the modes space $\mathbf{W_n}$, yielding to:

$$\mathbf{W_{n+1}} = \mathbf{D} \times \mathbf{W_n}. \tag{1.67}$$

From Eq. (1.67) and Eq. (1.64) the expression of the modes evolution can be achieved

$$\mathbf{W_n} = \mathbf{P}^{-1}\mathbf{X_n} \tag{1.68}$$

which leads, in combination with the definition of eigenvectors for circulant matrices in Eq. (1.58), to the next relation

$$\mathbf{W_n} = \mathrm{IDFT}(\mathbf{X_n}). \tag{1.69}$$

Eq. (1.68) allows to compute amplitude, A_i, and phase, Φ_i, for each oscillation mode

$$W_i^{N_b} = A_i^{N_b} \cdot e^{j\Phi_i^{N_b}} \tag{1.70}$$

from the a_i and ϕ_i of each bunch.
This procedure shows that, once performed the modal analysis, it is possible to get the matrix **D** of eigenvectors and derive the matrix **C** from Eq. (1.64). At this point **M** can be determined by transforming each element of **C**, as an example c_{11}, in a pure rotation block of **M**:

$$\begin{aligned} m_{11} &= \Re(c_{11}\ e^{j2\pi Q_s \times n}) \\ m_{12} &= -\Im(c_{11}\ e^{j2\pi Q_s \times n}) \\ m_{21} &= \Im(c_{11}\ e^{j2\pi Q_s \times n}) \\ m_{22} &= \Re(c_{11}\ e^{j2\pi Q_s \times n}). \end{aligned}$$

Once **M** has been evaluated, the stability of the system can be studied. The application of this approach to the PS will be shown in Chapter 3, where we will evaluate the evolution matrix of the longitudinal CB motion in the PS.

1.6 Summary

In this Chapter I presented the basic equations governing the longitudinal multi-bunch dynamics in a circular accelerator as well as multiple concepts such as impedance and beam spectrum which will be used in the next Chapters. Several examples concerning the specific case of the Proton Synchrotron were introduced describing the circulant matrix approach to study the longitudinal beam dynamics and to derive the modes of the system: the application to the specific case of the PS will be shown in Chapter 3.
In the next Chapter I will go through the description of the Proton Synchrotron, the injector where the longitudinal structure of the nominal LHC beam is produced. I will analyze the complex RF system and introduce, starting from the machine impedance knowledge, the impedance model necessary to simulate the CB dynamics in the PS.

Bibliography

[1] M. Sands, "The physics of electron storage rings: an introduction," *University of California, Santa Cruz, SLAC-121*, 1970.

[2] S. Prabhakar, "New diagnostics and cures for coupled-bunch instabilities," *SLAC Report 554*, 2001.

[3] A. Chao, "Physics of collective instabilities in high energy accelerators," *John Wiley and Sons, Inc.*, 1993.

[4] J. Laclare, "Bunched beam instabilities," *11th International Conference on High Energy Accelerators*, Geneva, 1980.

[5] M. Oliphant, "The acceleration of particles to very high energies," *Classified memo submitted to DSIR, University of Birmingham Archive*, 1943.

[6] K. Hübner, "50 Years of research at CERN: from past to future accelerators," *CERN 2006-004*, 2006.

[7] J. D. Lawson, "Early Synchrotrons In Britain, and Early Work for CERN," *Rutherford Appleton Laboratory, UK.*

[8] S. Hughes, "Magnetic force, magnetic fields, ampere's law," *Massachusetts Institute of Technology, Department of Physics*, 2004.

[9] A. Hofmann and F. Pedersen, "Bunches with local elliptic energy distributions," *IEEE Trans. Nucl. Sci., Vol. NS-26, No.3*, 1979.

[10] B. Montague, "Basic hamiltonian mechanics," *CAS - CERN Accelerator School: 5th Advanced Accelerator Physics Course, Rhodes, Greececcelerator school: 5th advanced accelerator physics course, Rhodes, Greece*, 1995.

[11] S. Hancock and J. S. Alvarez, "A pedestrian guide to online phase space tomography in the cern ps complex," *CERN-PS-RF-NOTE-2001-010*, 2001.

[12] L. Palumbo, V. G. Vaccaro, and M. Zobov, "Wake fields and impedance," *LNF-94/041*, 1994.

[13] D. J. Griffiths, "Introduction to electrodynamics," *Prentice Hall, pp. 559-562.*

[14] A. Palmieri and L. Tecchio, "Cavity longitudinal loss factor measurements by means of a beam test facility," *Physical Review Special Topics - Accelerators and Beams, Volume 3, 112001*, 2000.

[15] "Finemet review," *https://indico.cern.ch/event/315998/*, 2014.

[16] V. G. Vaccaro, "Longitudinal instability of a coasting beam above transition, due to the action of lumped discontinuities," *CERN ISR-RF/66-35*, 1966.

[17] A. Sessler and V. G. Vaccaro, "Report ISR-RF/67-2," *CERN*, 1967.

[18] L. Palumbo and V. Vaccaro, "Wake fields, impedances and green's function," *CAS Advanced School*, Oxford, 1986.

[19] H. Panofsky and W. Wenzel, "Some considerations concerning the transverse deflection of charged particles in radio-frequency fields," *Rev. Sci. Instrum. 27, pp. 967*, 1956.

[20] V. Bargmann, "Irreducible unitary representations of the lorentz group," *Ann. of Math., 48 (3): 568-640.*

[21] V. Illingworth, "The penguin dictionary of physics," *Penguin Books*, 1991.

[22] R. M. Gray, "Toeplitz and circulant matrices: a review," *Deptartment of Electrical Engineering, Stanford University.*

[23] P. Lancaster, "Theory of matrices," *Academic Press*, NY, 1969.

[24] P. J. Davis, "Circulant matrices," *Wiley-Interscience*, NY, 1979.

Chapter 2

The CERN Proton Synchrotron

Nowadays 57 years old (2016), the CERN Proton Synchrotron is the world's first synchrotron based on the alternating-gradient focusing principle [1]. The history of CERN and its accelerators dates back to the early post World War II years. The successful development of CERN during more than five decades was largely due to the surprising flexibility of the alternating-gradient PS.
In this Chapter I will describe the Proton Synchrotron to characterize the central role of this machine in the LHC chain and also to introduce devices that will be further investigated in later Chapters to determine the main sources of longitudinal couple-bunch instabilities.

2.1 Historical Introduction

"We made it. Protons in the LHC: complete turn with beam 1 and beam 2". This is the entry in the log book that finally celebrates the first protons injected into the LHC on 10 September 2008. The entire world could witness the successful first turn in the LHC of the beam delivered from the injector complex. Concerning the PS, this was the successful result of the preparation of the LHC-type beams that started back in 1993, with the first injection test at 1.4 GeV. Already then, it was decided that the transverse emittances of the LHC-type beam should be defined in the PSB, whereas the longitudinal structure should be the result of a very complicated series of RF gymnastic in the PS. The beam should be cleaned by eventual tails in the SPS and the longitudinal and/or the transverse emittances increased by controlled blow-ups. The nominal LHC transverse emittances could already be produced in 1999 once the 1.4 GeV injection energy had become the standard [61], whereas the different bunch splittings leading to the 25 ns time structure could be finalized in 2001.

When the PS started its operation 1959 it was equipped with 16 ferrite-loaded cavities operating at the same frequency, on harmonic $h = 20$. An RF source was used for beam capture and during the early part of the cycle and acceleration, a phase loop and a radial loop were activated to avoid longitudinal dipolar oscillation and keep the beam centered in the vacuum chamber. The operation of the first beam allowing acceleration through transition in an alternating-gradient system was demonstrated on 24 November 1959 [1]. Then in 1972 the SPS was built,

demanding more requirements from the PS, like a high-intensity beam ($> 10^{13}$ ppp) at 10 GeV/c, bunched at the SPS frequency of 200 MHz. This required ad hoc process to transfer the bunches from the PS to the operating frequency of SPS. First tests with beam revealed an unacceptable longitudinal blow-up during debunching, due to a longitudinal microwave instability [2]. A solution was found by driving few 200 MHz cavities with a phase modulated signal at an harmonic of the accelerating RF frequency; in this way the longitudinal emittance of the bunches could be blown up in a clean and controlled way during the early part of the acceleration cycle to keep the beam below the instability threshold.
In Chapter 3 we will give an historical overview of the different type of longitudinal instabilities over the years in the PS.

2.2 The PS as LHC Injector

The PS is one of the injectors of the LHC. It is a ring of 628 m circumference made of 100 straight sections and 100 magnets units where the beam gets injected, accelerated and extracted in a magnetic cycle duration multiple of 1.2 s. We consider part of the PS accelerator complex a linear accelerator LINAC2 and four smaller circular machine, the PS Booster, LEIR (Low Energy Ions Ring), AD (Antiproton Decelerator) and ELENA (Extra-Low Energy Antiproton). A layout of the complex is shown in Fig. 2.1. Several types of beam are prepared in the PS: below there is a

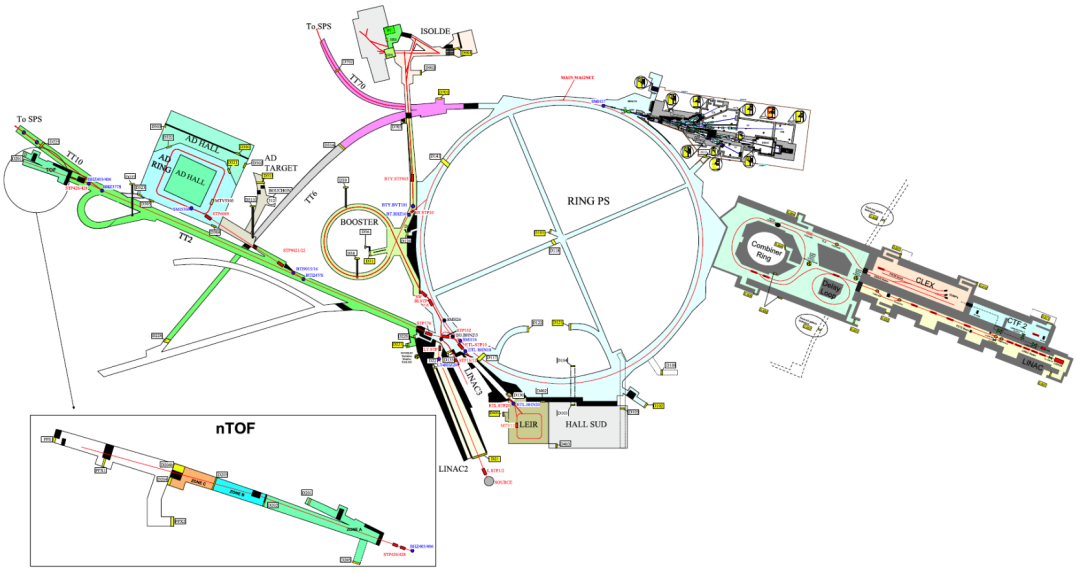

Figure 2.1. Proton Synchrotron complex layout

list and in Tab. III are shown the corresponding operational details.

- The AD beam is a 26 GeV/c proton beam, sent to the AD target, where 3.5 GeV/c antiprotons are produced and collected;
- The TOF 20.3 GeV/c beam provides beam towards the n-TOF (neutron-Time Of Flight) facility beam line at the end of FTN line;

- The SFTPRO CT is 14GeV/c proton beam used for Slow Extraction on North Targets;
- The EAST beam provides beam for the EAST experimental area;

Table III. Types and characteristics of beams produced in the PS. Harmonic number and energy are at beam extraction.

User Name	N_b	h_{ext}	E_{ext} [GeV]	I [10^{10}p]	Extraction Type
AD	4	20	26414	400	fast
EAST	1	debunched	19.4	20-50	slow
TOF	1	8	19.4	700-850	fast
SFTPRO	420	420	13	1.97	continuous
LHCINDIV	1-4	84	25	15	fast

More details regarding these schemes can be found in [3].
In the list above it was deliberately omitted to description of the nominal LHC beam, which is the operational beam for all the measurements shown in this thesis and that we are going to investigate in detail.

The nominal LHC beam has a filling scheme which requires 2808 bunches into each ring with bunches separated by 25 ns. Proton beams are produced in the LINAC 2 up to a kinetic energy of 50 MeV. Pre-accelerated proton bunches are then injected into the first synchrotron of the chain, namely Proton Synchrotron Booster (PSB). The PSB is composed of four identical rings of 157.1 m circumference stacked one on the top of the another. This acceleration stage carries the proton bunches up to 1.4 GeV ($\beta = 0.916$). To produce an LHC-beam, PSB accelerates nominally one bunch per ring at $160 \cdot 10^{10}$ protons/bunch. The protons with an energy of 1.4 GeV are injected into the PS that, with its circumference of 628.3 m, is exactly 4 times larger than a single PSB ring.
Injection in the PS for normal LHC-type beam is composed of a first injection of one bunch per PSB ring and a second injection of only two PSB bunches, that corresponds to a filling ratio in the PS of 6/7 (h_{RF}=7), leaving a gap for the extraction kickers. The role of the PS in the LHC injection scheme is to prepare the bunch structure for the LHC ($1.3 \cdot 10^{11}$ p/bunch intensity in 2014, 4 ns long bunches spaced by 25 ns for an energy of 26 GeV and $\beta = 0.999$).
The SPS is a separated function alternating gradient synchrotron of 6911.5 m circumference, 11 times larger than the PS, equipped with a traveling wave RF system at 200 MHz and with a higher harmonic system at 800 MHz, that enables special acceleration and RF manipulation features. The bunches for LHC beams are prepared in the PS so that no further RF manipulation is needed in the SPS. One SPS cycle results in 2, 3 or 4 PS cycles for the respective total beam intensity in the SPS of 1.7, 2.5 or 3.3 $\cdot 10^{13}$ p/beam. In the SPS proton beams must be accelerated further to reach the LHC injection energy of 450 GeV and additional blow-up must be applied to reach the longitudinal emittance of 0.6 eVs. Then the proton bunches are finally injected in the LHC. The filling of each LHC injection requires 12 SPS cycles. The acceleration until 7 TeV lasts 20 minutes due to the magnet current

ramp limitation, which leads to a maximum energy gain of 485 keV/turn. At the end of an LHC injection the beam is composed of up to 2808 bunches at h_{RF}=3564 with a longitudinal emittance of 2.5 eVs.

2.3 LHC Nominal Beam Production in the PS

In addition to the beam intensity preservation and the acceleration, the PS has to give its final time structure to the proton beam, transforming it into a 40 MHz bunch train (25 ns spacing between bunches) in the nominal case. The generation of the LHC bunch train with a 25ns spacing is obtained with a multiple splitting as visible in Fig. 2.2: we keep in mind this measure throughout the following explanation as in here are visible all the steps that we will describe. In Fig. 2.3 is shown the magnetic cycle for the production of the nominal LHC beam and all the steps of the process (injection, acceleration and extraction) are visible. Six bunches delivered in

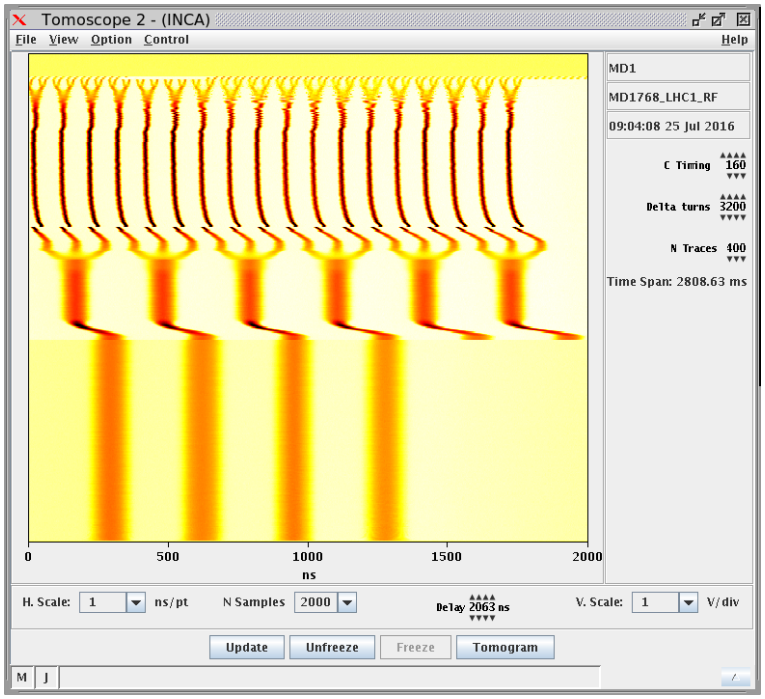

Figure 2.2. Tomoscope acquisition of the LHC25 beam production in the PS, from injection, via multiple splittings to the beam extraction.

two batches $(4 + 2)$ by the PSB are injected on harmonic $h = 7$ in the PS. Triple splitting is started after acceleration and provides 18 bunches on $h = 21$. The beam is then accelerated on this harmonic up to the 25 GeV flat- top, where each bunch is twice split into two to give 72 consecutive bunches on $h = 84$. This leaves a ∼300 ns gap in the bunch train for the rise-time of the ejection kicker.
The functioning of triple splitting is clear by observing Fig. 2.4: on the top of the image is shown the voltage behavior of the 10 MHz RF cavities (10 in total), divided in 3 groups and tuned at different harmonic, while on the bottom the evolution in the phase space as the voltage of the cavities change is represented. Starting with $h = 7$

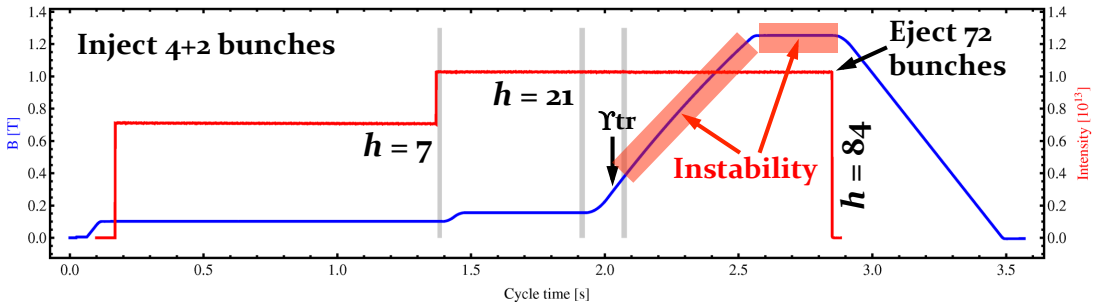

Figure 2.3. The LHC25 beam production cycle in the PS, LIU baseline.

alone, the effect of increasing the voltages on $h = 14$ and $h = 21$ is to flatten the bunch ($t = 7$ ms). In phase space, two new stable points emerge close to the initial one, encircled by three buckets. These three areas are kept equal throughout the process so that layers of increasing emittance in the initial bunch are progressively peeled off and accumulated evenly into the three new buckets. Provided that the

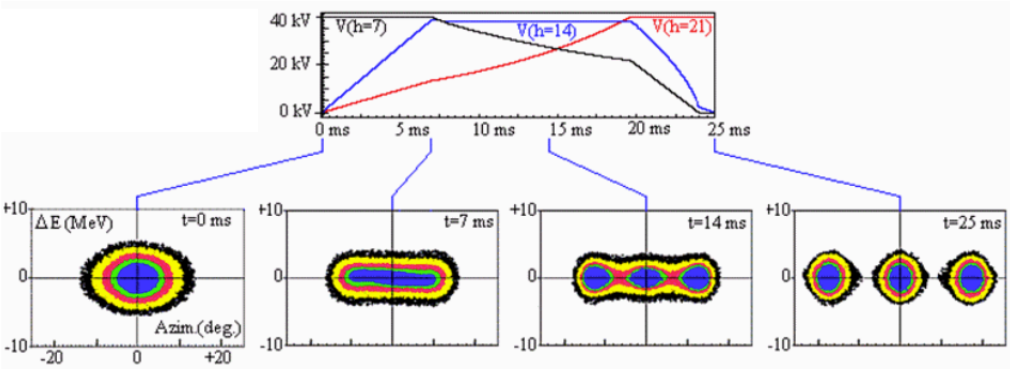

Figure 2.4. Principle of triple splitting. Top figure represents the beam voltage on $h = 7, 14, 21$. Bottom plots shows the evolution of the bunch in the phase space during the process [4].

rate of change of the voltages is sufficiently slow, the particles of the initial bunch are gradually captured in the new buckets whose area grows as the voltage decreases on $h = 7$ and increases on $h = 21$ ($t = 14$ ms). Three equal bunches are finally obtained, each with the same distribution of particle density as the initial one ($t = 25$ ms). The low-level RF generates the different harmonics, precisely controlling their relative phases. A beam phase loop is active throughout the process, controlling the sum of all harmonics whose relative phase is rigidly fixed.
Quadruple splitting at 26 GeV is obtained by cascading two double-splitting steps. Three groups of cavities are also employed, operating on harmonics 42 and 84 and 168 respectively. The relative phase between harmonics is rigidly fixed and a beam phase loop suppresses collective oscillations with respect to the RF sum voltage.

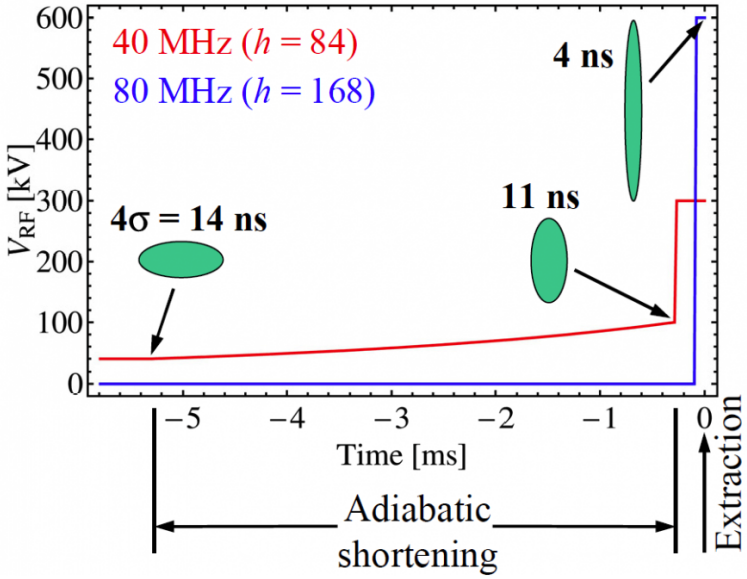

Figure 2.5. Basic representation of bunch rotation.

Short bunches (4 ns) for the LHC are required from the PS to allow for a bunch-to-bucket transfer to the SPS, which captures the beam with its 200 MHz RF system. To achieve a bunch length of 4 ns during operation a process called bunch rotation is performed. The process is described in Fig. 2.5: the bunches are first shortened from about 14 ns to 11 ns length by raising the voltage of the 40 MHz RF system ($h = 84$) from 40 kV to 100 kV within 5 ms. Then, 280 μs (∼130 turns) before extraction, the RF voltage is rapidly increased to 300 kV. The longitudinal mismatch of the bunches with respect to their buckets causes a rotation in longitudinal phase space, exchanging bunch length and momentum spread. Finally, 110 μs (∼50 turns) before extraction, an additional 80 MHz ($h = 168$) RF system further reduce the bunch length. The resulting bunch is then ready for transfer to the SPS and the empty buckets are used to ramp the ejection kicker.
The combination of the successive splittings from $h = 7$ to $h = 84$ provides the nominal bunch emittance and length, while avoiding beam loss at PS ejection during the rise-time of the ejection kicker.

The CERN PS is the first synchrotron where transition had to be crossed. The increase of energy in a medium energy proton synchrotron has two contradictory effects: an increase of the particle velocity and an increase of the length of the particle trajectory. According to the variations of these two parameters, the revolution frequency evolves differently. Below a certain energy, called transition energy, the velocity increases faster than the length: the revolution frequency increases. Above transition energy, the opposite is true (at very high energy the velocity reaches the speed of light and does not change anymore): the revolution frequency decreases. In Fig. 1.3 in Chapter 1 is shown the measured revolution frequency in the PS while

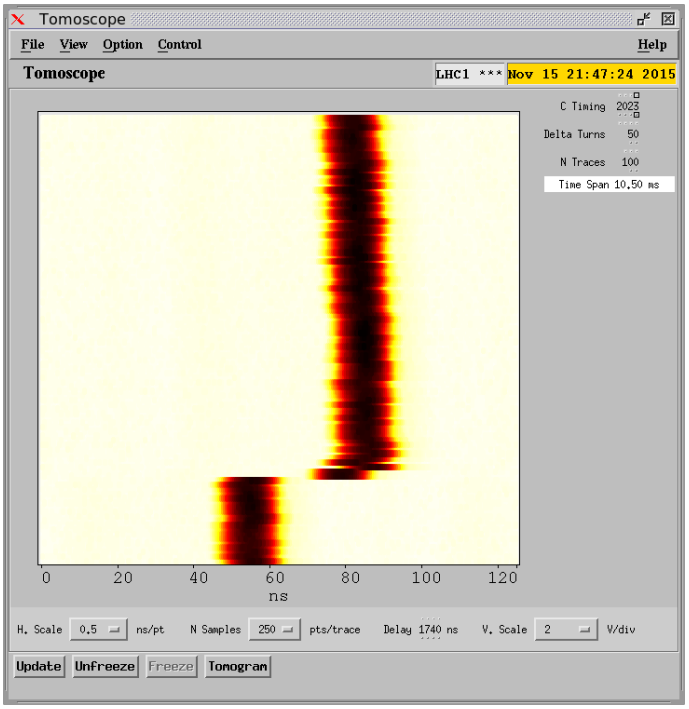

Figure 2.6. Tomoscope image of transition crossing in the PS

the transition γ_t crossing is indicated in Fig. 2.3 . At transition energy, the variation of the velocity is compensated by the variation of the trajectory. The relativistic mass factor at transition γ_t, is independent of the particle mass, its value depends only on the machine optics and geometry and is given by:

$$\gamma_t = \frac{1}{\sqrt{\alpha_p}} \qquad \text{with } \alpha_p = \frac{dC/C_0}{dp/p_0} \tag{2.1}$$

where C_0 is the path length of a particle with nominal momentum p_0 on the reference orbit (the parameter α_p is called the momentum compaction factor). In the case of a regular lattice (smooth approximation), the value of γ_t is close to the horizontal tune, $\gamma_t \approx Q_x$. In the PS the horizontal tune is $Q_x \approx 6.25$ and $\gamma_t \simeq 6.1$. In Fig. 2.6 we can observe a snapshot from the tomoscope of the beam behavior at transition crossing. Crossing transition changes the sign of the slip factor (which relates the frequency offset in the beam to its momentum offset) given by:

$$\eta = \alpha_p - \frac{1}{\gamma^2} = -\frac{\Delta f/f_0}{\Delta p/p_0} \tag{2.2}$$

As a first consequence of transition crossing, the synchronous phase has to jump rapidly from ϕ_s to $\pi - \phi_s$. If transition crossing cannot be avoided, the γ_t jump is the only method to overcome all the intensity limitations. It consists in an artificial increase of the transition crossing speed by means of fast pulsed quadrupoles. The idea is that quadrupoles can be used to adjust the momentum compaction factor α_p. These schemes were pioneered by the CERN PS group [5]. Such a γ_t jump scheme makes it possible to keep the beam at a safe distance from transition, except for the

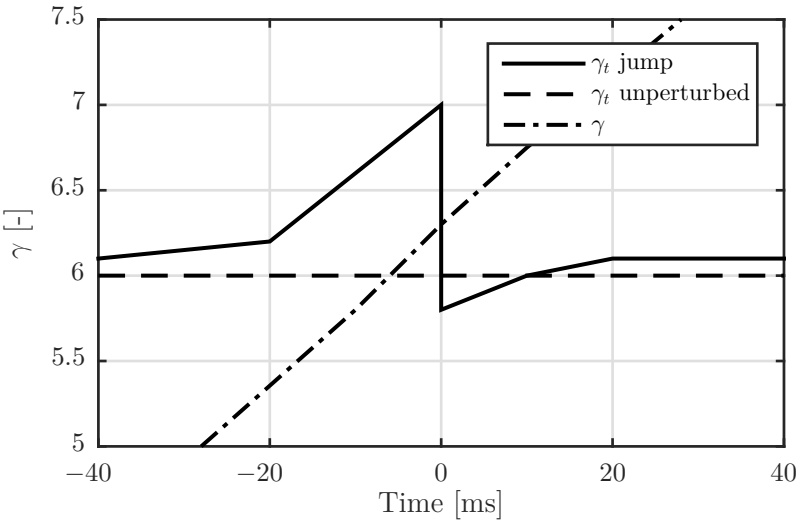

Figure 2.7. Evolution of γ_t (and of the γ of the beam) near transition crossing without and with the present PS γ_t jump [1].

very short time during which the transition region is crossed at a speed increased by one or two orders of magnitude. In Fig. 2.7 is shown the trend of γ_t in the PS with and without the γ_t scheme.
After transition crossing, during acceleration, CB instabilities are observed in the PS.

2.4 The PS Radio-Frequency System

The RF system at CERN covers a power range from the noise levels up to hundreds of MW. It is used to control momentum of the particles in the longitudinal and transverse planes or for beam diagnostics. In the longitudinal plane, electromagnetic fields create the RF buckets which allow to capture the injected beam, keep it bunched, provide the acceleration, deceleration, or keep the beam circulating at a constant energy in storage ring. The particle beams, composed of moving charges, emit electromagnetic energy so the RF systems are also widely used to measure the beam parameters. The CERN PS complex accelerates beams which are not relativistic. This means a relatively large change of velocity and implicit RF frequency variation. The RF systems perform complex beam manipulations, as described in the previous section, that require large frequency swings. The PS uses tunable, ferrite-loaded cavities and several fixed frequency cavities which are listed in Tab. IV. In Fig. 2.8 are shown the frequency range covered by the cavities and the different behaviors: 10 MHz cavities (C10) which are tunable; 20,40,80 and 200 MHz cavities which operate at fixed frequency (C20-C40-C80-C200); the lately installed Finemet cavity which is a wideband cavity. For further details we address to [6]. ge of the longitudinal impedance of the machine is important in order to understand the

Table IV. Summary of PS RF systems/cavities.

Name	N° of Cavity	h	Freq. Range [MHz]	Peak Volt. [kV]
C10	11	7-21	from 2.7 to 10	20
C20	2	28,42	13 or 20	15
C40	2	84	40	350
C80	3	168,169	80	350
C200	6	420,433	200	30
Finemet	1	.	0.4-5.5	5

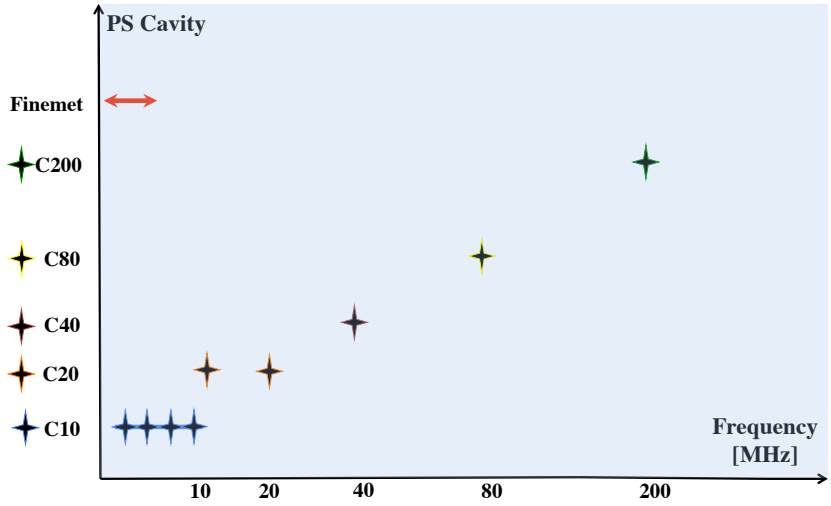

Figure 2.8. Summary of cavities frequency behavior.

machine limitations in terms of longitudinal instabilities. The detailed study of the PS longitudinal impedance was carried off for the first time in 1970 [7] then in 2012 [8] new studies were realized to identify the main sources of longitudinal impedance. In the following we will go through a detailed description of the RF system involved in the gymnastic described in this Chapter to understand purpose and functionality of each one along the PS magnetic cycle. In Fig. 2.9 we report an image of the PS ring indicating the straight sections where the different cavities we are going to describe are located. The knowled

10 MHz RF System

The PS is equipped with 10 (+1 spare) accelerating cavities: the 10 MHz cavities are located in straight sections SS11/36/46/51/56/66/76/81/86/91/96; in Fig. 2.10 we can see the picture of one of them. These cavities capture the bunches after injection, accelerate them to the desired energy and perform gymnastics such as bunch splitting. The cavities are programmable in phase, in voltage (0.5 kVp to 10 kVp), in frequency (2.8 MHz to 10.01 MHz) and in the way they work in groups during the PS super-cycle. Since it is not possible to control the parameters of each cavity individually, the 10 cavities were divided into three groups and for each

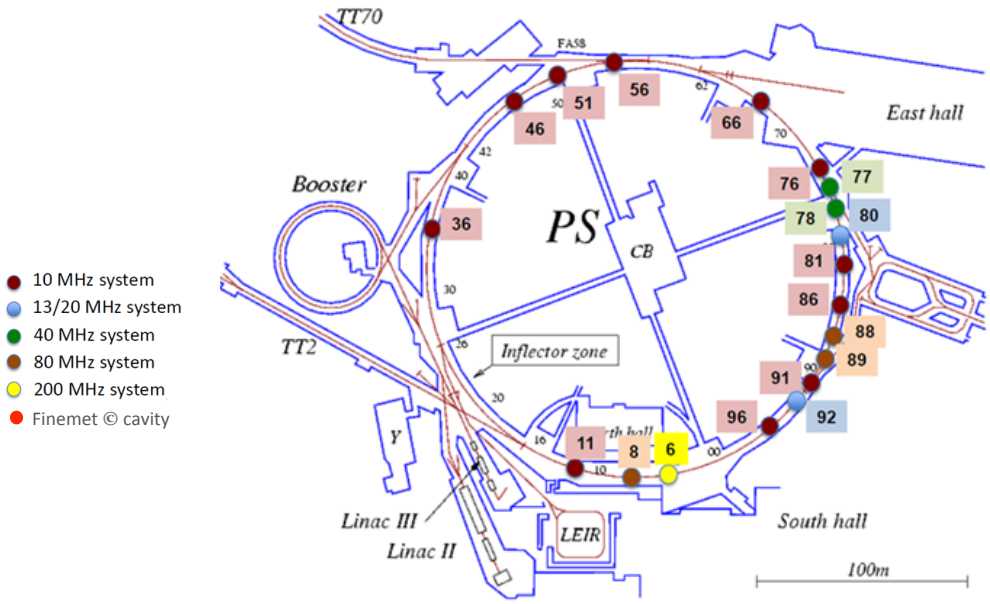

Figure 2.9. Disposition of the 25 RF cavities in the PS ring.

Figure 2.10. One of the accelerating radio frequency cavities of the 10MHz system. The actual ferrite loaded tunable cavity is in the top, under the red hatch. The blue base contains the power amplifiers.

group voltage and harmonic number program are defined. Fig. 2.11 and Fig. 2.12 summarize the measured harmonic and voltage program during the nominal LHC beam cycle production. Each programmed cavity group is tuned by the DC biased

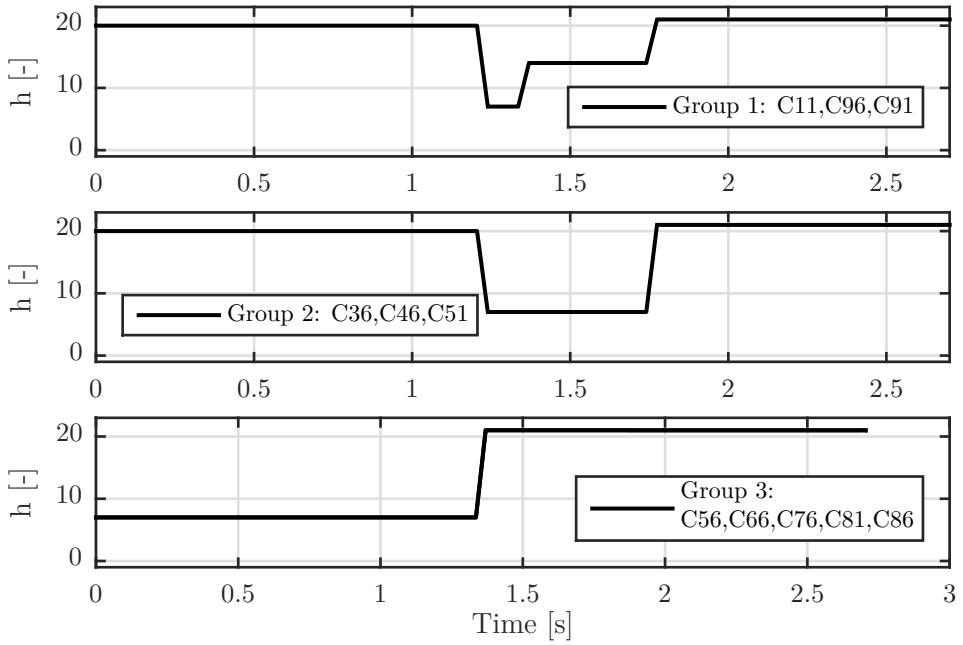

Figure 2.11. Tuning program for the 3 groups of 10 MHz cavities along the cycle.

ferrite rings and each cavity consists of two ferrite loaded $\lambda/4$ wave lines with the capacitive gap at the input end. The gaps are in series for the beam but are fed in parallel from the RF power amplifier. As seen from each cavity gap a bunched beam in the PS ring constitutes a current source with a frequency spectrum which depends on the bunch width, the spacing between bunches and the number of particles in each bunch. Several feed-back loops, closing around the beam are used to maintain a stable beam and lock the RF phase (phase loop, radial loop, coupled-mode and multi-harmonic instabilities). For this purpose, signal processing circuits, by means of specific filters, calculate a correction value which is sent to the system as a phase, frequency or amplitude modulation. Controls and low-level RF have to provide all the necessary signals, and the ferrite cavities had to operate in groups tuned at different frequencies and with different voltage programmes. The low-level RF has to be able to provide all these harmonics with the correct phasing.

As we explained in Chapter 1, CB instabilities appear at those frequencies where the interaction between the beam spectrum and the impedance is maximum. They appear in the cycle after transition during acceleration, just when all the 10 MHz cavities are active, providing in this way an high impedance contribution in $h = 21$. The first thing to do in such cases is to reduce the impedance of the cavity. In 2016 some major modification have been applied to the amplifiers of one of these cavities (application to the others will follow), the spare cavity C11 [9]; these modifications

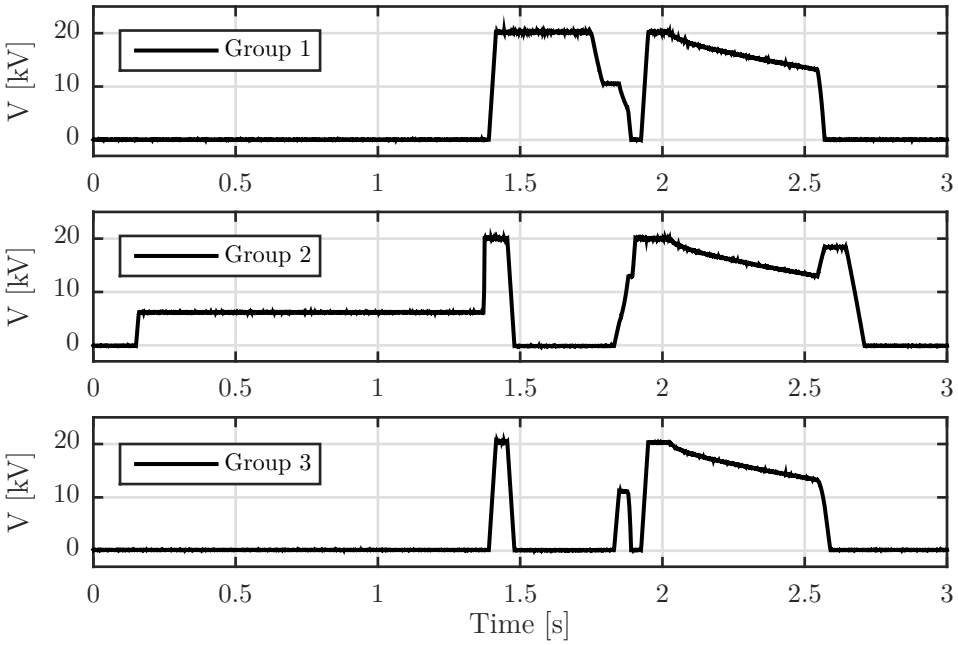

Figure 2.12. Measured voltage program for the 3 groups of 10 MHz cavities along the cycle.

have led to a reduction of a factor 10 of the closed loop transfer function of the cavity as visible in Fig. 2.13. We can see the resulted impedance (with the factor 10 of reduction) in Fig. 2.14 compared with the impedance of C81, as representative for all the other 10 MHz cavities. It is clear that the reduction of the closed loop transfer function have helped to reduce the impedance of C11.

During the RF gymnastic the performance in the PS is limited by the periodic transient beam loading induced in the cavities because of the partial filling of the machine with particles. The beam induced voltage in a cavity is about 8 kV [10]. The first three revolution frequency harmonics of the the beam current on each side of the RF are responsible for this cavity voltage. Even if each high power amplifier is provided with a fast feedback, a one-turn-delay feedback has been introduced as a complementary system to reduce the cavity impedance. This feedback design is able to cope with a wide frequency range due to particle acceleration (15% velocity variation) and choice of harmonic number. Loop gain is above 0 dB in the vicinity of revolution frequency harmonics over an instantaneous bandwidth of 3 to 4 times the 3 dB bandwidth of the original RF system. A reduction factor of 3.3 is measured with the feedback system for the peak voltage induced (from 8 to 2.4 kV). Detailed features description of the one-turn-delay feedback can be found in [10].

We already showed in in Section 1.3.2 the description of the process to extrapolate a simplified impedance model for the 10 MHz RF system to be used in simulations.

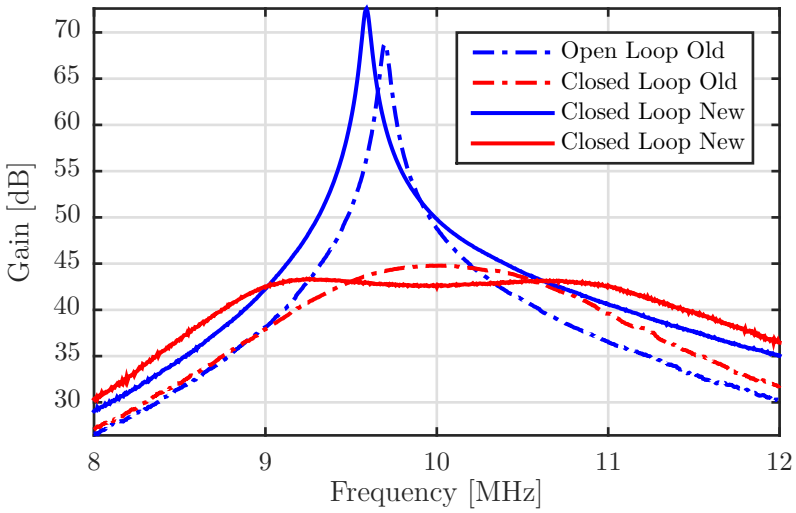

Figure 2.13. Transfer function of C11 with and without the amplifier modification [9]. The closed loop gain has been reduced considerably.

Tunable Cavities 13.3 MHz - 20 MHz

The PS is equipped with two 20 MHz RF cavities in SS80/92; they have a power amplifier driving one cavity and occupy a single short straight section. Each system delivers 16 kV nominal gap voltage and operates either 13.3 or 20 MHz. When not in use, high voltage relays short circuit the resonator while when in use the relays are open and RF feedback reduces the quality factor to 10 and the shunt impedance accordingly (20 dB reduction). During the cycle for the production of the nominal LHC beam, the cavity gap is open for 10-20 ms, so its impedance contribution has to be considered in simulations to investigate CB instabilities. One of the two cavities is shown in the next Section in Fig. 2.16; details and technical characteristic can be found in [11]. Fig. 2.17 shows the resonator parameters used to fit the measured impedance.

The 40 and 80 MHz Cavities

The PS is equipped with two 40 MHz and three 80 MHz cavities. They are always active during the cycle for the production of the LHC25.
The 40 MHz cavities in Fig. 2.18 are installed in SS77/78 and they have been designed and built at CERN as a part of the preparation of the PS as injector for the LHC. These cavities provide the necessary bunch spacing of 25 ns prior the injection into SPS. In order to fit a short section (1 m) of the PS the cavity has a strong capacitive loading (low R/Q). In Fig. 2.19 the cavity resonant expansion to be used in simulations is presented.
The PS is equipped with three 80 MHz cavities in SS08/88/89 that produce the required nominal bunch length of the LHC beam; one of them is showed in Fig. 2.20. The mechanical design is similar to that of the 40 MHz cavity with many commons

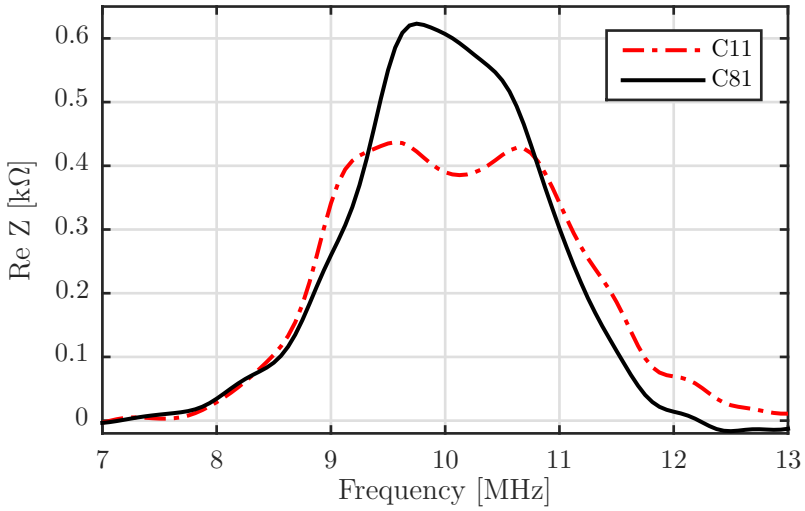

Figure 2.14. Measured real part of longitudinal impedance for C11 and C81.

part. Fig. 2.21 shows the resonator parameters used to fit the measured impedance.

The bunch compression scheme needs both adiabatic and non-adiabatic cavity gap voltage variations. The dynamic range of the 40 MHz system is required to be [3...300] kV. For the non-adiabatic part (bunch rotation), both the 40 MHz and the 80 MHz cavities should be able to be filled in 20 μs. Short pulses of up to 10 ms at duty cycles below 1 % are required for the 40 MHz system – the 80 MHz system is also capable of delivering long pulses. Beam loading is strong (nominal beam current at 40 MHz is 1.24 A) and the impedance must be kept as small as possible in order not to perturb other beams. For the accelerating mode, this impedance can be drastically reduced with fast RF feedback. For cavities design and more detailed information see [12] and [13].

The 200 MHz Cavities

The 200 MHz RF system in SS06 is shown in Fig. 2.22 and it is an essential tool for the preparation of the high-intensity beams. Presently, six RF cavities are operated to control the longitudinal bunch emittance and to rebunch beam before the transfer to the SPS. Cavities are selected for the various processes with a dedicated hardware matrix, switching the individual timing pulses and voltage programs per cavity. In Fig. 2.23 is shown the impedance resonant expansion with the correspondent parameters. In [14] [15] technical description and details regarding the control structure for the 200 MHz RF system can be found.

Longitudinal Damper Cavity: the Finemet

In 2014 a new cavity has been designed and installed in SS02 to operate as longitudinal kicker for the feedback system to damp coupled-bunch instabilities. The design of the new damper, driven by a solid state amplifier, is based on the wideband frequency characteristics of Finemet magnetic alloy. It is equipped with 6 RF cells each providing a fraction of the total RF voltage; the CST model of the cells is shown in Fig. 2.15. Each cells consists of a ceramic gap with a Finemet magnetic

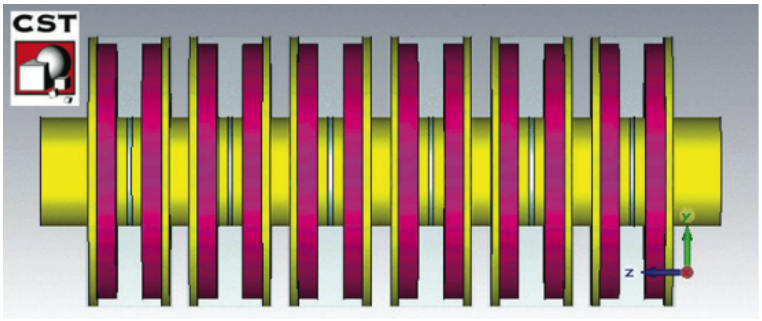

Figure 2.15. CST model of the six cells Finemet loaded longitudinal damper [16].

alloy core being powered by solid state amplifier. All details regarding the design and specifics of the damper can be found in [16].

The impedance model in Fig. 2.24 has been obtained as a sum of 17 resonant modes (see Tab.V) given the particular shape of the impedance. The fit of the real part matches the measured curve, although the fitted imaginary part doesn't correspond to the measured one as well. We need to specify that Eq. (1.40), that relates the impedance real and imaginary part, is valid between plus and minus infinity; measurements, on the other hand, can be performed in a limited frequency range. This means that when we fit the impedance in a limited frequency range, we are assuming that it is zero outside our measuring window. This explain the difference between the fitted and measured imaginary part. In Chapter 4 we will show the commissioning of FB system and the Finemet cavity.

2.4.1 The PS RF Cavities: Impedance Models

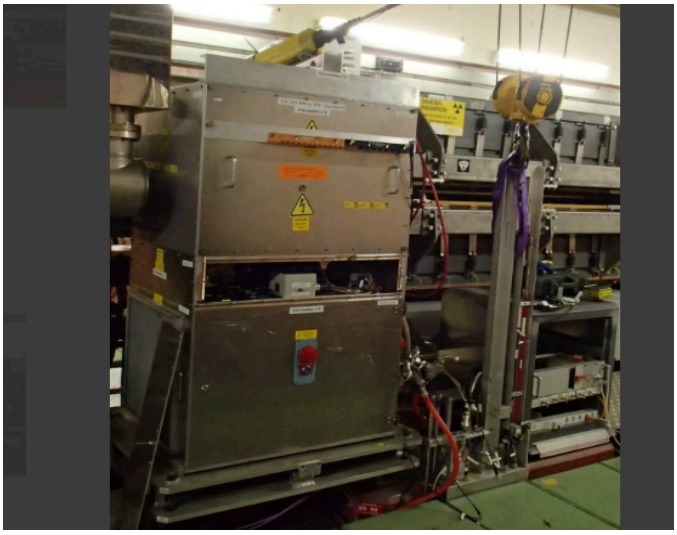

Figure 2.16. The 20 MHz RF cavity.

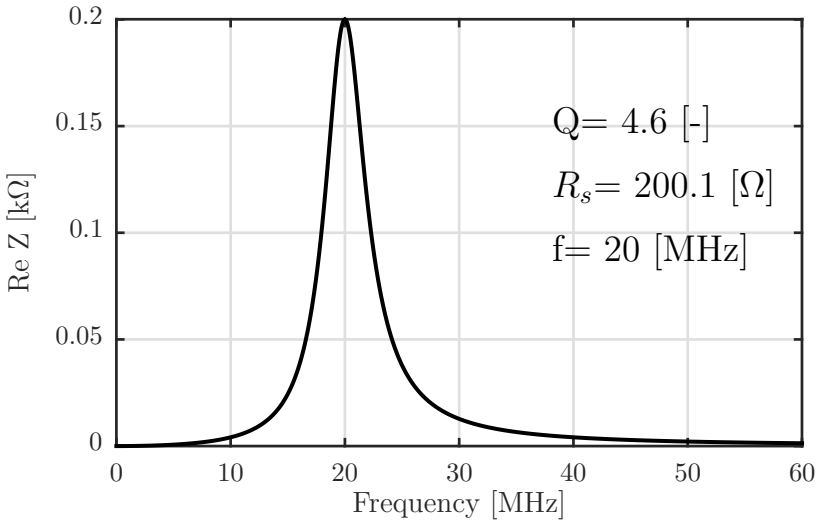

Figure 2.17. The 20 MHz simplified impedance model with the corresponding parameters.

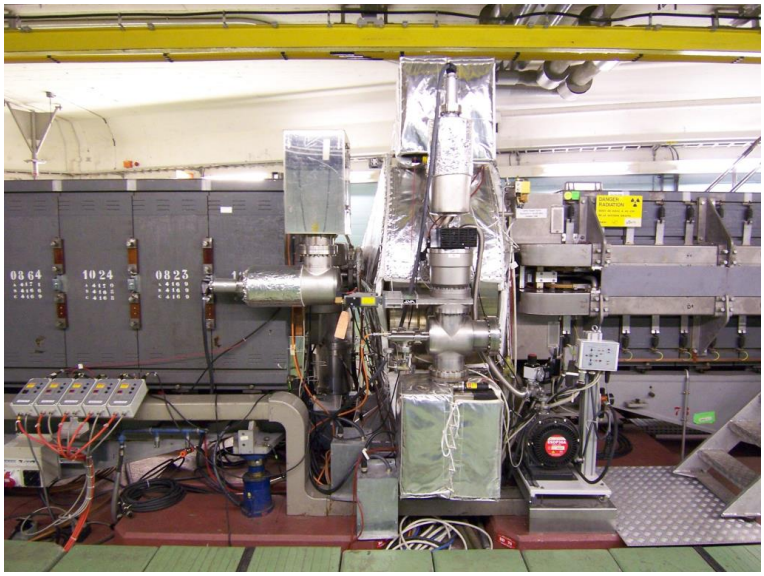

Figure 2.18. The 40 MHz radio frequency cavity 'Susan'.

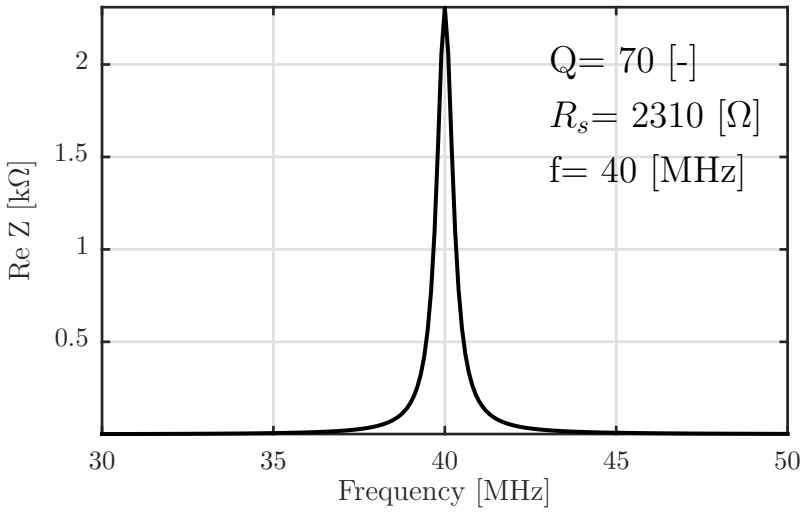

Figure 2.19. The 40 MHz simplified impedance model with the corresponding parameters.

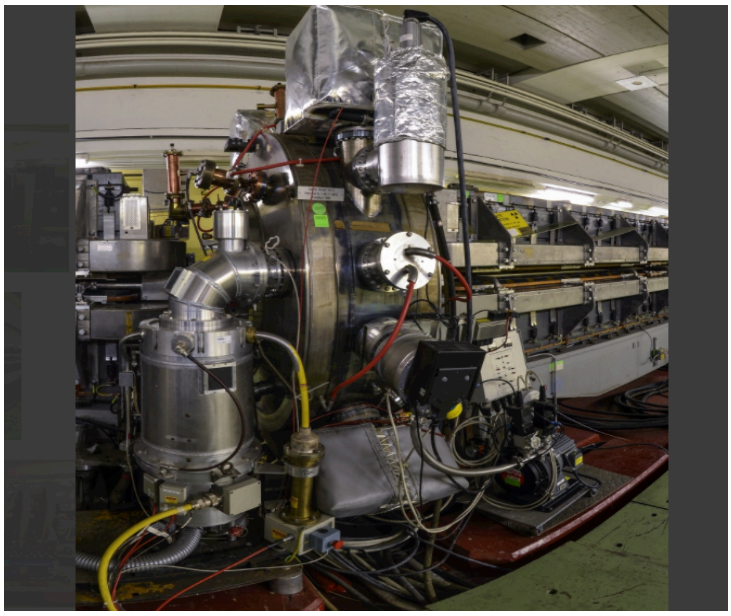

Figure 2.20. The 80 MHz radio frequency cavity 'Anne'.

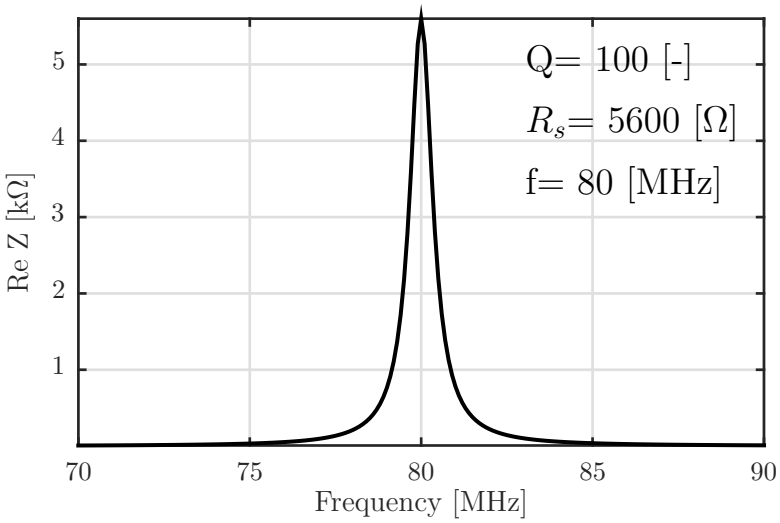

Figure 2.21. The 80 MHz simplified impedance model with the corresponding parameters.

Figure 2.22. Six 200MHz radio frequency cavities.

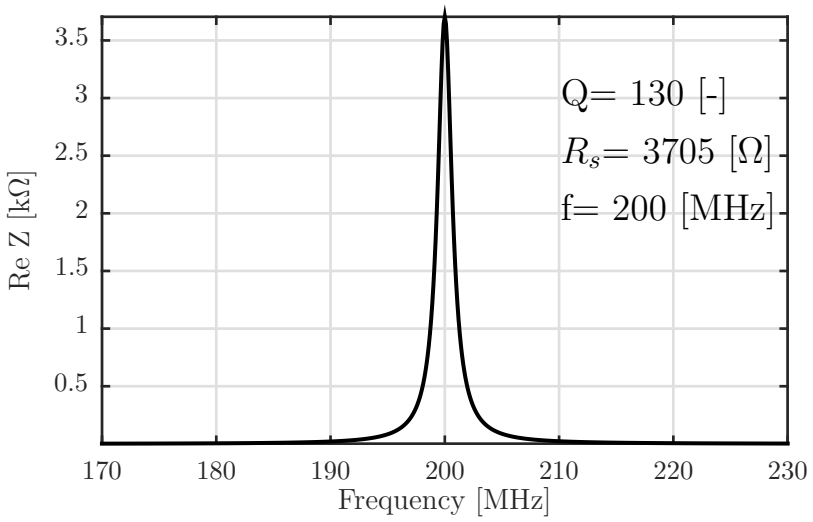

Figure 2.23. The 200 MHz simplified impedance model with the corresponding parameters.

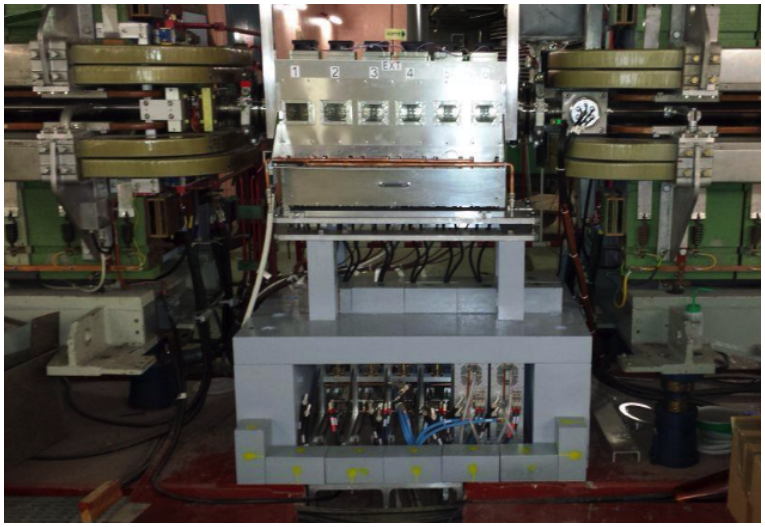

Figure 2.24. 6 cells Finemet cavity installed in the PS.

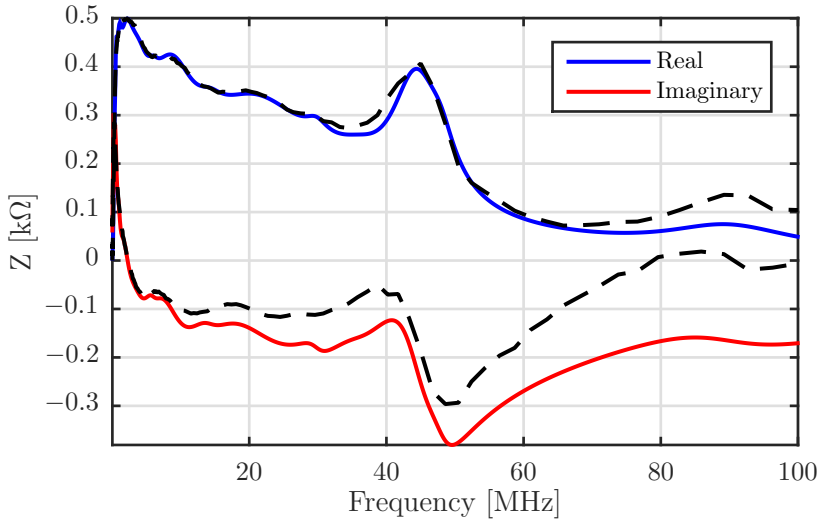

Figure 2.25. Measured real and imaginary part of the Finemet cavity impedance (6 cells). The proposed fits is indicated in black dashed lines.

Table V. Parameters used to fit the Finemet cavity impedance.

Q	$\mathbf{R_S}$ [Ω]	**Freq.** [**MHz**]
5	258	44
10	60	48
4	48	90
0.7	354	2.2
1	324	0.6
1	276	9
1	252	22
1	162	4.2
7.4	30	30
2	42	35.5
5	18	35.6
1.2	180	1.1
1.8	132	0.3
3	33.6	14.4
3	30	6

2.5 The LHC Injectors Upgrade Project

In early 2013 the CERN accelerator complex shut down for two years of planned maintenance and consolidation, with the so called First Long Shutdown (LS1). The main priorities in LS1 were to prepare the machine for high-energy operation and to ensure reliable operation through the second long run, *i.e.*, up to the next long shutdown scheduled for 2018. From the LHC design report the machine is expected

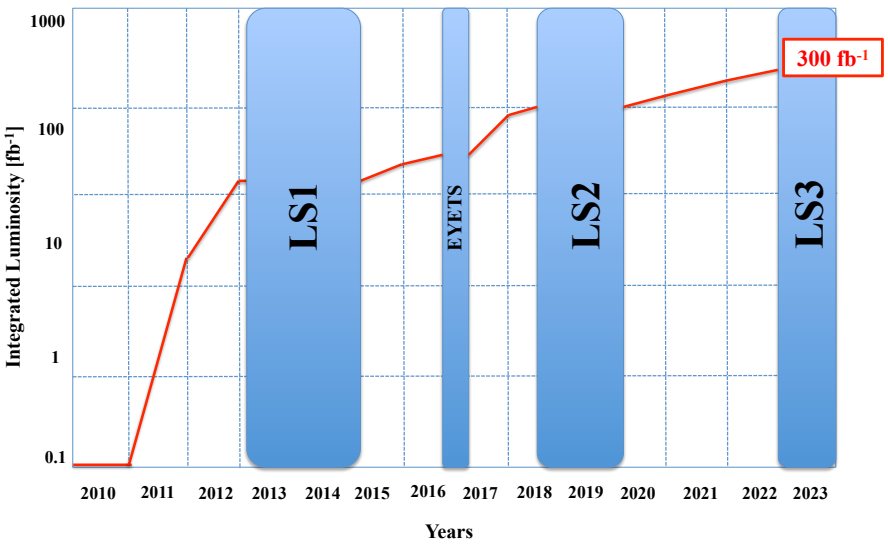

Figure 2.26. Expected trend for the LHC integrated luminosity along years. EYETS stays for Extended-Year-End-Technical-Stop.

to reach 7 TeV at collision [17]. The foreseen trend for the integrated luminosity is shown in Fig. 2.26.

HL-LHC Project

The High Luminosity LHC (HL-LHC) project aims to reduce the statistical error in the measurements that are carried out by the four experiments. This error is proportional to $1/\sqrt{N}$ with N the number of observations for a given event. The aim is to achieve an increase of the number of collisions per second in order to improve the statistical significance of the data.
The luminosity L [$\mathrm{cm}^{-2}s^{-1}$], is the figure of merit which connect the physical parameters σ [b] (1barn=10^{-24} cm^2), the cross section for the event, and N_{event} which is the number of collision per second. It is defined as:

$$\dot{N}_{\mathrm{event}} = \sigma \cdot L \tag{2.3}$$

According to this relation the number of events can be increased only by increasing the luminosity, operationally defined as:

$$L = \frac{N_p^2 N_b f_{rev} \gamma_{rel}}{4\pi\sqrt{\varepsilon_x \beta_x^* \varepsilon_y \beta_y^*}} \cdot F, \tag{2.4}$$

with N_p the number of protons per bunch, N_b the number of bunches, f_{rev} the revolution frequency, $\sqrt{\varepsilon_i \beta_i^*}$ the transverse beam dimension at the interaction point and F the geometric factor which takes into account the crossing angle between the colliding beams.

This year (December 2016) the maximum integrated luminosity reached is about 40 fb^{-1}, exceeding the initial expectations.
In Tab.VII are quoted the values of integrated luminosity reached in October 2016 for each experiment. Since April 2016, the LHC has delivered more than 30 fb^{-1}

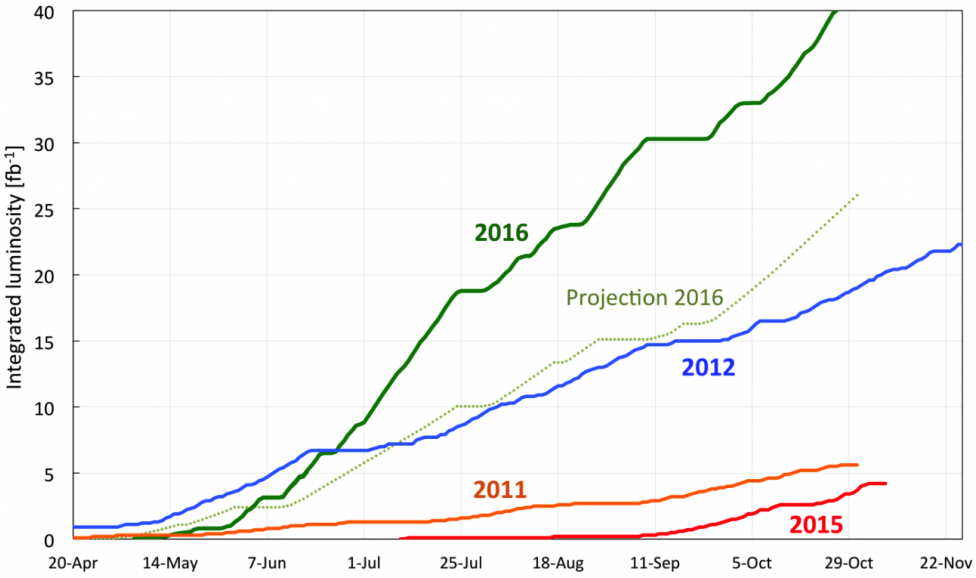

Figure 2.27. The integrated luminosity of the LHC with proton-proton collisions in 2016 compared to previous years. The integrated luminosity achieved by the LHC in 2016 far surpassed expectations and is double that achieved at a lower energy in 2012. The maximum reached is about 40 fb^{-1} (average CMS/ATLAS) compared with the 25 fb^{-1} originally planned. [18].

Table VI. Integrated luminosity at 6.5 GeV on October 3rd 2016.

Experiment	Integrated Luminosity	Unit
ATLAS	31.93	fb^{-1}
ALICE	12.05	pb^{-1}
CMS	32.62	fb^{-1}
LHCb	1.59	fb^{-1}

to both ATLAS and CMS. This means that around 2.4 quadrillion collisions have been seen by each of the experiments this year. This compares with the total of 33.2 fb^{-1} produced between 2010 and 2015. The unprecedented performance this year is the result of both the incremental increases in collision rate and the sheer amount of time the LHC has been up and running [18]. These values have to be compared with the final goal of the HL-LHC project which requires 250-300 fb^{-1}, achieving a luminosity of 10^{35} cm$^{-2}s^{-1}$, ten times higher of the design values of the LHC.

The LIU Project

The HL-LHC luminosity parameters can only be reached with a major upgrade of the LHC injector chain, therefore the LHC Injectors (LIU) project has been started in 2010 with the objective of providing reliable beams with the challenging characteristics required by HL-LHC until 2030. The injectors are expected to produce 25 ns proton beams with about double intensity than nowadays. Tab.VII summaries the achieved beam parameters at LHC injection, those estimated achievable with the current baseline LIU upgrades and finally the ultimate HL-LHC target parameters. To reach this goal, a cascade of improvements is needed across the whole injectors

Table VII. Proton Beam Parameters at LHC Injection. These parameters translate into 2.6·10^{11} at the PS extractions.

Project	**N** $[10^{11}]$ p/b
Achieved	1.2
LIU	2
HL-LHC	2.3

chain. We refer to the PS TDR [19] for a summary of the upgrade intervention in the PS. An important ingredient to reach the required intensity in the PS is the newly installed longitudinal feedback to suppress coupled-bunch instabilities. In the next Chapters we will present the studies carried out to find the impedance source of CB instability and to commission the FB as well as the new longitudinal damper. We will also present the tools used during the research *i.e.*, the simulation code and the data analysis algorithm.

2.6 Summary

In this Chapter I introduced the CERN Proton Synchrotron, a very versatile synchrotron, with a complex system RF, that produces different kind of beam in a large spectrum of parameters. I analyzed in detail the production cycle of the LHC nominal beam explaining the different phases and underlining the role of each RF cavity in this production process. Starting from the present impedance model of each cavity I adopted the fitting procedure presented in Chapter 1 to obtain the resonant expansion that we will need in the next Chapter for the simulation studies. Finally I introduced the upgrade projects of the LHC complex showing the integrated luminosity obtained during the run of 2016 and the goals to be reached.

Bibliography

[1] S. Gilardoni and D. Manglunki, "Fifty years of the CERN Proton Synchrotron," *CERN-2011-004*, 2011.

[2] D. Boussard, "Observation of microwave longitudinal instabilities in the CPS," *CERN/LAB/II/RF/75-2*, 1975.

[3] G. A. et al., "Beam parameter at LHC Injection," *CERN-ACC-2014-0006*, 2014.

[4] R. Garoby, S. Hancock, and J. Vallet, "Demonstration of bunch triple splitting in the CERN PS," *Proceedings of EPAC, Vienna, Austria*, 2000.

[5] W. Hardt, "Gamma-transition-jump scheme of the CPS," *Proceedings of the Ninth International Conference on High Energy Accelerators, SLAC, USA*, 1974.

[6] D. Valuch, "Radio frequency systems of the CERN synchrotron accelerators," *RADIOELEKTRONIKA, 19th International Conference*, 2009.

[7] D. Boussard, "Proc. of pac'79," *San Francisco, California, 1979, p. 3568.*

[8] M. M. et al. *Phys. Rev. ST Accel. and Beams, Vol. 16, p. 031001, 2013.*

[9] G. Favia, "Study of the beam-cavity interaction in the cern ps 10 mhz cavities and investigation of hardware solutions to reduce beam loading," *CERN Thesis*, 2017.

[10] F. Blas and R. Garoby, "Design and operational results of a one-turn-delay feedback for beam loading compensation of the CERN PS ferrite cavities," *CERN/PS 91-16(RF)*, 1991.

[11] M. M. et al., "The PS 13.3-20 MHz RF system for LHC," *20th IEEE Particle Accelerator Conference, USA, Ed. J. Chew (JACoW, Geneva, 2003), pp. 1724–6*, 2003.

[12] R. Garoby, "The PS 40 MHz bunching cavity," *CERN/PS/97- 039, Proc. PAC '97, Vancouver*, 1997.

[13] D. G. et al., "The PS 80 MHz cavities," *CERN/PS/98-021(RF), Proc. EPAC '98, Stockholm*, 1998.

[14] D. Boussard, "The PS 200 MHz RF system present situation and future prospects," *CERN-SPS/ARF/78-6.*

[15] H. Damerau and S. Hancock, "New control structure of the 200 MHz RF system in the CERN PS," *AB Note 2009-015 (RF)*, 2008.

[16] S. P. et al., "Impedance studies for the ps finemet longitudinal damper," *5th International Particle Accelerator Conference, Dresden, Germany, p. 1708*, p. 1708, 2014.

[17] "LHC Design Report Volume I."

[18] M. Giovannozzi and J. Wenninger, "LHC Operation Meeting."

[19] "LIU-PS Technical Design Report Webpage," *https://test-liu-ps-tdr.web.cern.ch/test-LIU-PS-TDR/*.

Chapter 3

Simulations and Analysis of Coupled-Bunch Instabilities

During the last years the CERN PS became a key-accelerator with a central position in the LHC accelerator chain and with the largest number of beam destinations in the CERN Complex; a significant part of its working time is dedicated to provide beams to LHC and particular attention is given to high intensity beams. As the intensity per bunch has increased over the years, limitations directly related to high intensity beams were discovered and constrained the number of particles that can be accelerated. Therefore, an effort was done to understand these limitations and several studies are under way to improve the beams required for the different experiments.
In this Chapter I will first give an historical note on the issue of longitudinal instability in the PS and I will show how, during the years, the type of instabilities observed has changed. Then I will introduce the simulation code used for this study as well as an example application to show not only how the code works, but to demonstrate in practice some of the theoretical concepts introduced in Chapter 1 (*i.e.*, frequency spectrum, impedance model, rise time). The results of the simulations obtained with the impedance model shown in Chapter 2 will be presented to confirm that the 10 MHz cavities are the main cause of CB instability and to check that the longitudinal damper impedance (Finemet cavity) does not affect in any way the stability of the beam. The predictions for the HL-LHC beam parameters will be proposed.
Finally it will be explored the new algorithm implemented to analyze the measured data and resolve the CB mode analysis as well as its application to the PS to find the system evolution matrix and study its stability.

3.1 Evolution of Longitudinal Instabilities in the PS

Microwave Instabilities

The longitudinal beam parameters in high energy colliders are in general given by downstream machines and they are selected to attain the highest possible luminosity that can be handled by physics experiments. The task of the injection chain is to satisfy these requirements in terms of longitudinal emittance, number of particles

per bunch and distance between bunches. During the design plan of the LHC beam in the PS the proposed method to produce the longitudinal structure of the beam was to debunch it by lowering in an iso-adiabatic way the voltage, and to rebunch with another RF frequency. The iso-adiabaticity was needed to minimize the emittance blow-up and the voltage variation over a large dynamic range. This technique presents a number of drawbacks: RF voltages must be controlled down to small amplitudes in the presence of beam-loading, while drifting the beam is left uncontrolled, the full circumference is filled with particles, the beam has a very small $\Delta p/p$ which makes it prone to microwave instability [1].
The microwave instability is one important manifestation of collective effects in accelerators. The result of this instability is a significant increase in longitudinal emittance of the beam, leading to a serious performance limitation. The name microwave (μw) instability was first introduced by D. Boussard in 1971 to describe the very large momentum blow-up suffered by proton bunches during debunching in the CERN PS seen together with microwave signals (above 1 GHz).
Due to the mentioned considerations and observations the option of debunching (at 10 MHz) and rebunching (at 40 MHz) was abandoned due to microwave instabilities on the PS flat-top. This required the development not only of triple splitting (see Chapter 2), but also a crash programme to make a 20 MHz (h =42) cavity to bridge the gap between 10 MHz and 40 MHz via double splitting process [2]. Bunch splitting have therefore been developed as alternative method that allow the number of bunches to be changed without passing via debunched state. This alternative process was first proposed in preparation of the LHC beam; when the CERN accelerator complex re-started in March 1998, this technique became a routine operation.

Coupled-Bunch Instabilities

With the introduction of the bunch splitting technique, microwave instability became a minor issue, while it became increasingly important to precisely control the phases of the bunches to prevent oscillation and makes the splitting optimal. With the introduction of the triple splitting in the nominal beam production, CB instabilities became one of the main problems to be addressed since they do not allow a precise control of the bunch phase.
The first observation of dipolar longitudinal instabilities can be found in a paper of 1975 [3].

> "In the CPS it is a parasitic accelerating cavities which is responsible for the instability. Each bunch leaves in the cavity a wake that will excite the next bunch. If we do not use Q-jump at transition, the bunches are longer so that the instability is Landau damped by RF non-linearities. We succeeded in damping this instability by powering at half RF frequency one of our cavities. This provides a bunch to bunch synchrotron frequency spread which decouples the bunches. This stabilization however is not powerful enough. When half of the available power at $\omega_{RF}/2$ is applied the bunches still oscillate. At full power the stabilization is barely sufficient. We cannot increase the number of cavities that we use for this purpose. For these reasons we are now

> looking into an active feedback, but with the large harmonic number of the PS ($h = 20$) one has to be careful not to excite other modes."

During the years, changing the machine parameters (*i.e.*, beam intensity) and the kind of RF gymnastic, the problem of CB has always been of major interest. An analog feedback system was used for study purpose until 2014 to suppress the instability as well as a spare 10 MHz cavity was used as a longitudinal damper [4]. Machine development (MD) studies have been performed during the machine run in 2006 with a high intensity proton beam, comparable to the intensity of the LHC-type beam, to identify possible impedance sources for these instabilities [5]. As we mentioned in Chapter 2, within the HL-LHC Project, the intensity target has been increased and it is expected to double in the PS. CB instabilities, since intensity dependent, have been recognized as one of the main problem to deal with.

3.2 MuSiC: Multibunch and Multiparticle Simulation Code

The theory underlying CB instabilities as well as the methods for observing and determining the modes of oscillation were introduced in Chapter 1. In this section we want to show the results obtained with the MuSiC [6] simulation code which has been used both to confirm the impedance model of the PS and to make predictions of the beam behavior with the new HL-LHC parameters. We will start with the introduction of some details about the code and its operation to make easier the understanding and the interpretation of the simulation's results.

Simulations of the beam dynamics in presence of collective effects require a strong computational effort to take into account the wakefields acting on a given charge and produced by all the others. Generally this is done by a convolution integral or sum, as illustrated in Chapter 1, Eq. (1.43). Moreover, if the electromagnetic fields consist of resonant modes with high quality factors, responsible for example of CB oscillations, a charge is also affected by itself in previous turns and a very long record of wakefield must be properly taken into account.

MuSiC (Multibunch and multiparticle Simulation Code) is a code developed by M. Migliorati, for the longitudinal beam dynamics in a circular accelerator [6], which exploits an alternative approach to the currently used convolution sum, reducing the computing time and avoiding the issues related to the length of wakefield. With this approach it is possible to simulate, without the need of a large computing power, simultaneously, the single and multi-bunch beam dynamics including intra-bunch motion. The method that MuSiC proposes does not need the wakefield as input, but a particular fitting of the coupling impedance requiring the use of resonator impedance model, thus avoiding issues related to the knowledge of the wake. The algorithm is quite light and does not need high computing power, even with the inclusion of intrabunch motion. The details regarding the original approach developed for this code are described in [6].
The only requirement of the code, as stated, is to represent the machine impedance

as a sum of resonant modes, method introduced and explained in Chapter 1 using the 10 MHz impedance model, Eq. (1.42). In addition to the tracking the code reconstructs from the dipolar oscillations of the center of mass of the bunches, turn after turn, amplitude and phase of the coherent modes of oscillations of the whole beam in the canonical base.

Application: Single Resonator Impedance

We want now to propose an example application of the simulation code. We consider

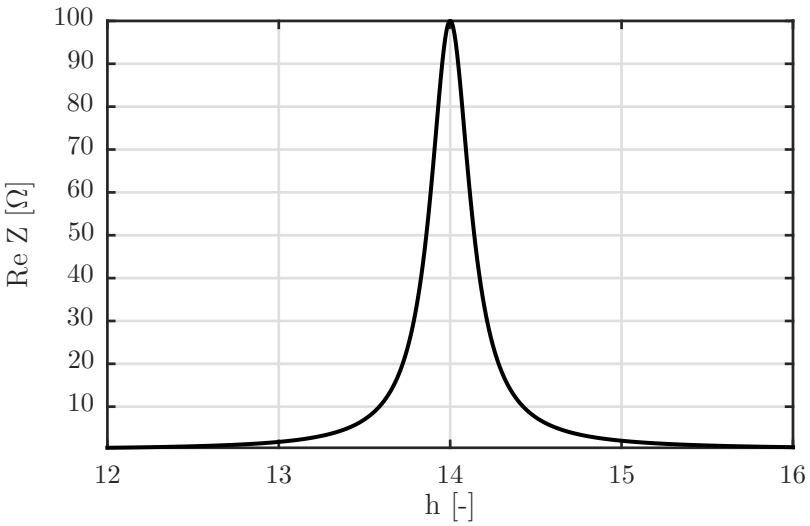

Figure 3.1. Test impedance parameters: $Q = 5 \times 10^5$, $R_s = 50\ k\Omega$, $\omega_r = 1.93 \times 10^9$.

as reference machine the PS, and perform simulations at a fixed energy (in the code acceleration is not implemented yet) above transition in h =21 with 21 bunches. The other parameters used in the simulation are summarized in Tab. VIII. In this particular case, I consider a test impedance, modeled as a single resonator centered around the $14th$ revolution frequency as shown in Fig. 3.1 where, on the x-axis, is represented $h = \omega/\omega_0$.

For the LHC-type beam in the PS with h =21, 21 different modes of oscillations show up as sidebands of the revolution frequency harmonic and the indication of CB oscillations are the spectral lines of the beam as from Eq. (1.56). As we explained in Section 1.4, above transition energy, positive sidebands of the beam spectrum, evaluated at multiples of $\omega_0+\omega_s$ are unstable, while the negative sidebands, evaluated at multiple of $\omega_0 - \omega_s$ are stable. In this case the impedance is centered around $14\ \omega_0 + \omega_s$, and the unstable CB mode associated with the upper sidebands is μ =14. Fig. 3.2 shows the outcome of the simulation code: the mode $\mu = 14$ is unstable, increasing exponentially in time while all the other oscillation modes are unaffected by the resonator. In Fig. 3.3 the excited mode was isolated from the others. From the exponential fit we obtain $\tau^{-1} = 0.23\ \text{ms}^{-1}$ which is in line with the theoretical

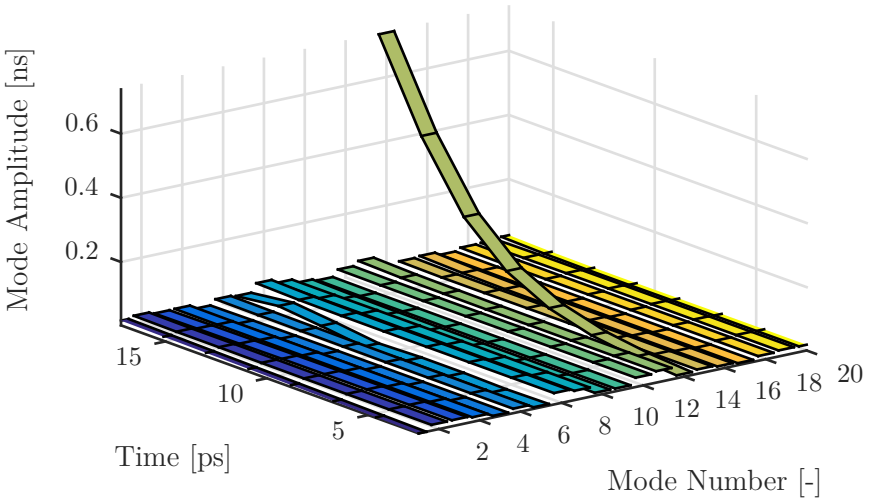

Figure 3.2. 3-D representation of the evolution of the CB mode amplitude excited by the impedance in Fig. 3.1.

Table VIII. Machine parameters used for simulations.

Parameter	Value	Unit
N_b	21	-
I	2.6×10^{11}	ppb
L	628.32	m
E	15	GeV
V_{RF}	168	kV
σ	2	m

one $\tau_{th}^{-1} = 0.22$ ms^{-1}.

3.3 Coupled-Bunch Simulation Studies

In the simulation studies that are shown in the next Sections, we are going to accomplish three different tasks:

- Test the simulation code by comparing its output, in term of growth rates, with the ones evaluated from measurements;
- Show that the 10 MHz system is the main source of instabilities, confirm the negligible contribution of the Finemet cavity as well as the other high frequency cavities to CB instability and test the impedance model derived in Chapter 2;
- Provide prevision within the HL-LHC parameters space (double intensity).

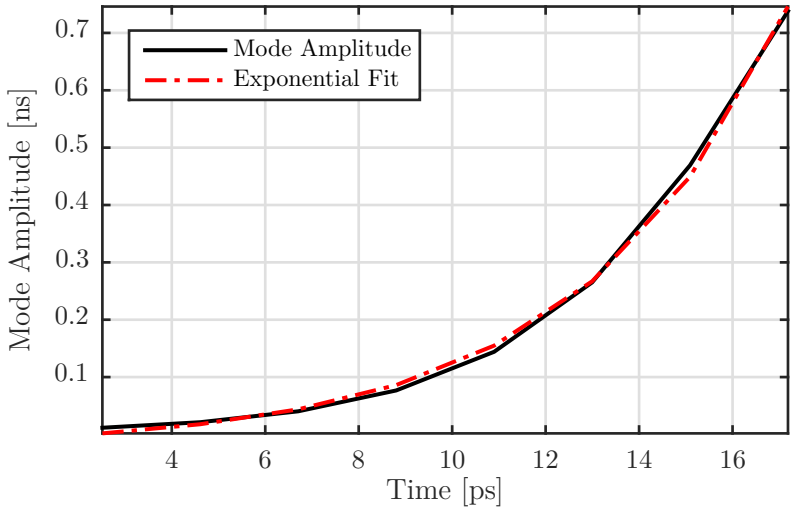

Figure 3.3. Evolution of μ =14 amplitude extracted from Fig. 3.2 and correspondent exponential fit.

3.3.1 Benchmarking of the MuSiC Code in the PS

In order to understand the CB excitation mechanism and the source of impedance numerous machine development (MD) studies were performed during 2006 with a high brightness proton beam, comparable to the brightness of the LHC-type beams in the PS [4]. At that time, to simplify the mode identification, seven bunches have been injected and accelerated at $h = 7$. The 20, 40 and 80 MHz RF systems were switched off with their gaps short circuited. Other machine settings are shown in Tab. IX. The CB instabilities were observed shortly after transition crossing and developed during acceleration. Firstly, growth rates were measured by analyzing the

Table IX. Parameters used for simulations for $h = 7$.

Parameters	Value	Unit
Beam energy	13	[GeV]
Harmonic number	7	[-]
Number of bunch	7	[-]
RF voltage	165	[kV]
Total beam intensity	$9 \cdot 10^{12}$	[ppp]

beam signal around a specific harmonic of the revolution frequency and secondly, the spectrum of the CB modes has been extracted from mountain range measurements. The mode spectrum was very reproducible and the $\mu = 2$ oscillation mode was excited first and had the maximum amplitude. At that time rise times from measurements were compared with the ones from theory, showing a good agreement [4]. CB growth rate from the theory are shown in Tab. X.

Table X. Comparison between CB growth rates in $h = 7$ for 7 bunches.

Mode Number μ	$\mu = 1$	$\mu = 2$	$\mu = 3$
CB Growth Rate from Theory	400 ms	333 ms	1 s
CB Growth Rate from Simulations	544 ms	467 ms	1.91 s

I performed simulations in the same machine conditions, as Tab. IX, to test the simulation code vs measurement. By an exponential fit on the simulated mode amplitudes I evaluated the growth rates and compared them with the theoretical ones. Simulations are consistent with the measurements results obtained in 2006, the mode pattern obtained is the same and confirm that in this machine configuration mode $\mu = 2$ grows unstable stronger than the others. Both measurements and simulations gives results in line with the theory as in Tab. IX.

3.3.2 Source of Coupled-Bunch Instability

Longitudinal CB instabilities are observed after transition crossing, causing asymmetries of the various bunch splittings used to establish the required bunch spacing and compromising the quality of the delivered bunch train.
Results from measurements analysis for the nominal LHC beam in 2006 pointed to the 10 MHz cavities as main contribution to the longitudinal impedance driving these instabilities [5]. This hypothesis can be confirmed considering both the RF system configuration during the cycle as shown in Chapter 2 and the simulation results: during acceleration in fact all the 10 MHz cavities are active and tuned in $h = 21$, thus maximize their impedance. I performed several simulation with a bunch intensity of $1.3{\cdot}10^{11}$ ppb at extraction and a kinetic energy of 15 GeV, which is used as a reference value to observe the instability during acceleration only. At the time of these simulation studies the code was not provided yet with the multiparticle internal distribution feature, so we performed simulations with the single macroparticle model. As pointed out in Chapter 2, the PS has a total of 25 RF cavities that follows this setup during the nominal LHC beam cycle:

- **10 MHz**: all the cavity gaps are open during acceleration and some are short circuited on the flat-top. At the start of the splitting to $h = 42$ only one 10 MHz is left with gap open;
- **Finemet**: the impedance of this cavity is always present since there is no possibilities to close the gap;
- **20 MHz**: the cavity gap only opens when the cavity is in use; it takes ∼10-20 ms to open/close;
- **40 MHz**: the impedance is always present;
- **80 MHz**: even in this case the impedance is always present;

I set up multiple simulations with each single cavity to observe the CB mode pattern: whilst with the 10 MHz system only, modes start to become unstable as observed in

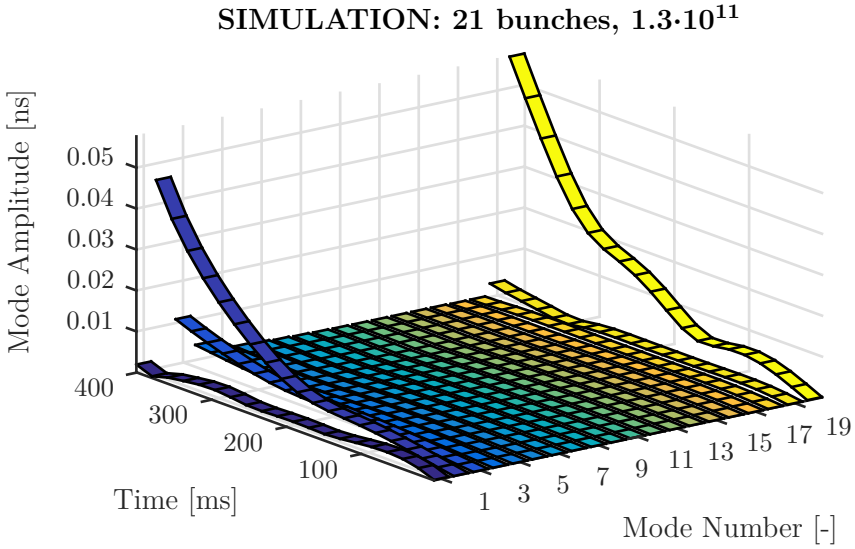

Figure 3.4. Simulated CB modes evolution in $h = 21$ with 21 bunches with $1.3 \cdot 10^{11}$ ppb. These simulations have been performed with the bunch modeled as a single macroparticle.

measurements, using the other cavities mentioned above individually, the modes do not show any unstable behavior.
Afterwards, using as a basis the model of the 10 MHz, I started adding all the other cavities one by one: the mode pattern was not changed by the contribution of the other impedances. A detailed description of these simulations can be found in [7]. In Fig. 3.4 the simulated CB modes evolution in $h = 21$ with 21 bunches is shown. Mode $\mu = 2$ and $\mu = 20$ grow unstable, the first stronger than the other. For mode $\mu = 2$ has been evaluate a growth rate of $\tau_{Old} \sim 130$ ms. This value can be compared with the one evaluated in measurements in 2007 for the same mode, $\tau_{2007} \sim 165$ ms [4].
A remark is mandatory. When we consider the bunch stationary distribution, for a Gaussian bunch of rms length σ_z, the growth rate for the multi-bunch case (see Eq. (1.52)) has to be corrected with a factor [6]:

$$G_m(x) = \frac{2}{x^2} e^{-x^2} J_m(x^2), \qquad x = \frac{(p\omega_0 \pm m\omega_s)\sigma_z}{c} \tag{3.1}$$

with J_m the modified Bessel function of the first kind. Since in these simulations we are modeling a bunch as a single rigid macroparticle, the growth rate evaluated from simulations needs to be corrected by a factor $f = e^{-x^2} = 0.84$ if we consider a $\sigma_z \sim 1$ m (close to the measured one in the machine of 1.4 m). To be noticed that the correction factor f does not take into account the Landau damping for the non linearity of the RF voltage that can influence the τ value. Following this consideration, we can say that there is a good agreement between the simulations and measurements by comparing τ_{Old} and τ_{2007}.

The simulated modes configuration can be confirmed even by observing the 10 MHz

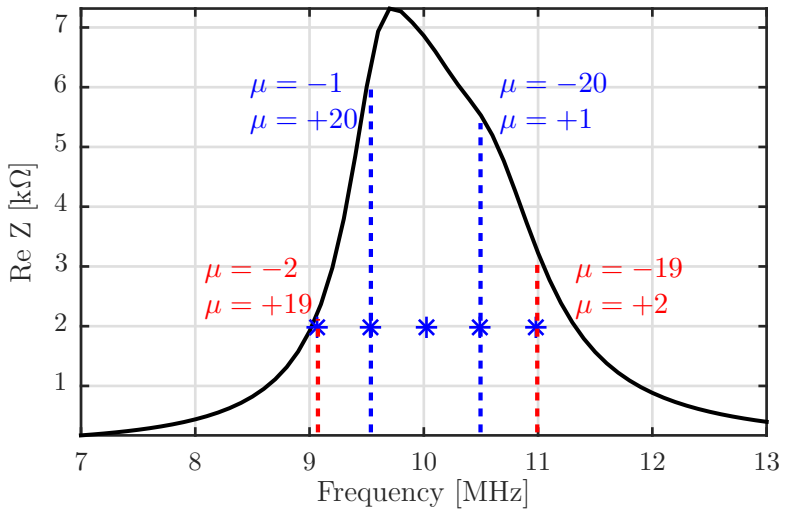

Figure 3.5. Real part of the 10 MHz system cavities impedance. With the dashed lines are represented the spectral lines at the revolution frequency harmonic and the related CB modes associated. With − and + signs are indicated the modes correlated to the lower and upper sidebands: the − is the stable one and the + is the unstable one.

cavities impedance in Fig. 3.5. As highlighted in Chapter 1, CB modes corresponds in frequency to the upper and lower sidebands of the revolution frequency; the mode associated with the upper sideband (+ sign in Fig. 3.5) is unstable, while the the mode associated with the lower sideband (− sign in Fig. 3.5) is stable. If we observe the location of the sidebands associated with mode $\mu = 2$ and $\mu = 20$ we can see that the unstable sidebands are positioned where the real part of the impedance is higher and does not get compensated from the correspondent stable ones; this implies that these two modes grow unstable. For the other modes, upper and lower sidebands balanced themselves and the modes result stable. In addition the difference between the lines $+2$ and -2 is higher than that for $+20$ and -20, confirming that the mode $\mu = 2$ has a stronger instability with respect to mode $\mu = 20$ as it was observed during measurements.

These simulation study allowed to confirm the efficiency of the MuSiC code to simulate the longitudinal dynamics in the PS and of the impedance model developed as resonant expansion. Simulated growth rates are in line with the measured ones once we take into account the correction factor for the bunch distribution.

3.3.3 Prediction for the HL-LHC Beam

In view of the operation with the new beam parameters planned within the HL-LHC Project, I have performed simulations to provide predictions on the beam stability. I have provided to the simulation code MuSiC the impedance model inclusive of the

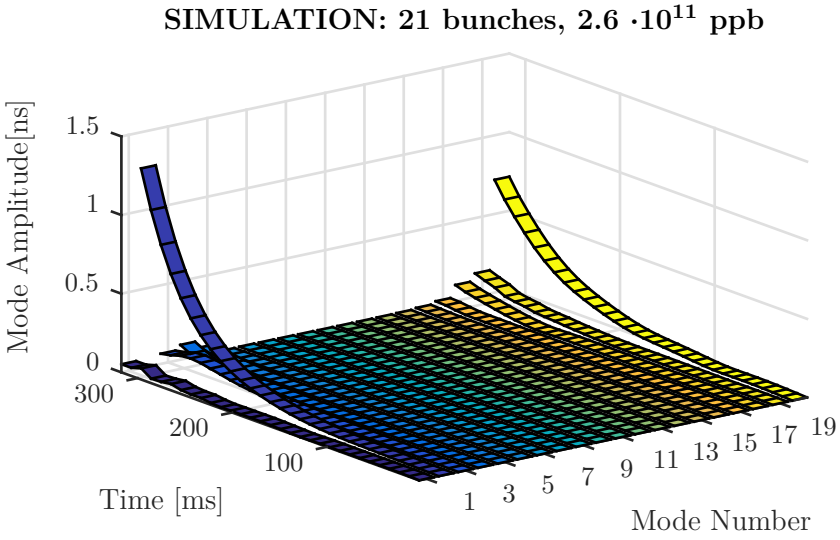

Figure 3.6. Simulated CB modes evolution in $h = 21$ with 21 bunches with all the cavities and $2.6 \cdot 10^{11}$. These simulations have been performed with the bunch modeled as a rigid macroparticle.

10 MHz system, the Finemet cavity as well as the 20, 40 and 80 MHz systems; with an kinetic energy of 15 GeV to reproduce the instability during acceleration and an intensity of $2.6{\cdot}10^{11}$ ppb at extraction. In order to compare these new results with the one showed in previous section, in first instance, the single macroparticle model was adopted. The resulted CB mode evolution is shown in Fig. 3.6 for 21 bunches in $h = 21$. We can compare this evolution with the one in Fig. 3.4. In both cases the mode pattern turns out to be the same, with modes $\mu = 2$ and $\mu = 20$ growing unstable whilst the others are not influenced, as expected. From an exponential fit on mode $\mu = 2$ we obtain $\tau_{New} \sim 50$ ms; this result is in agreement with the expectation from theory: since in the two simulations we are doubling the intensity, we expect that τ decreases by half accordingly. If we correct the τ_{New} obtained with the single macroparticle model, with the factor f, we obtain approximately $\tau^{C}_{New} =$ 60 ms: this is the mode growth rate that we expect to observe in the machine for a bunch 1 m long with the new beam intensity.

Once available the multiparticle internal distribution feature of the code we performed a scan of the bunch length σ_z between 0 m (single macroparticle model) and 1 m. Fig. 3.7 shows the CB modes evolution for σ_z =1 m. Mode $\mu = 2$ is clearly unstable with $\tau^{1m}_{New} \sim 67$ ms: as we expected this value is compatible with τ^{C}_{New} which was corrected by the factor f.
The mode $\mu = 20$ is not as unstable as in the single macroparticle simulations confirming the observation in the machine. As from Fig. 3.5, the shape of the impedance lines predict the mode $\mu = 2$ being stronger than $\mu = 20$, and these simulations with a bunch length comparable to the measured one, confirm the direct observation in the machine [4] which address the mode $\mu = 2$ as the most unstable in $h = 21$.

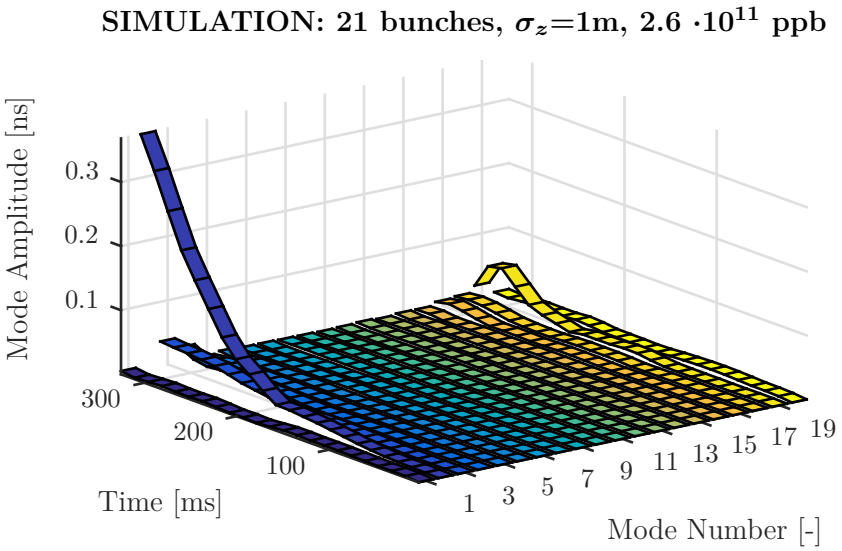

Figure 3.7. Simulated CB modes evolution in $h = 21$ with 21 bunches, σ_z =1 m and $2.6 \cdot 10^{11}$ ppb.

Simulations with the new LIU intensity, with the single macroparticle first and with the internal distribution, are in line with the expectation and the theory and allow to have an estimation of the τ_{New}^{1m} for the most unstable CB mode. This estimation will be used in Chapter 4 to make important consideration for the FB system.

3.4 Coupled-Bunch Modes Analysis

Besides simulations, which are definitely a powerful tool to extrapolate predictions and to study on the beam behavior, numerous dedicated MD session have been performed to confirm the simulations results and to commission the new FB system, as it will be discussed in the next Chapter.
Starting from the measurements of the longitudinal profile of the bunches along the cycle, it is possible to obtain the motion of the center of mass of each bunch and to derive the information on the coherent modes of oscillation of the system. There is a technique that was used previously at CERN to study the CB modes, nevertheless I developed my own tool to extrapolate the CB modes from the longitudinal profile with the aim to overcome the limitations of the existing algorithm and to provide a more precise results. In the next sections both techniques will be introduced highlighting weaknesses and strengths

3.4.1 Standard Analysis Technique and Limitations

Before I developed and proposed the algorithm to analyze the bunch train and to perform the mode analysis, a technique to serve this purpose already existed. In the following I will give a brief overview of this method and highlight the limitations

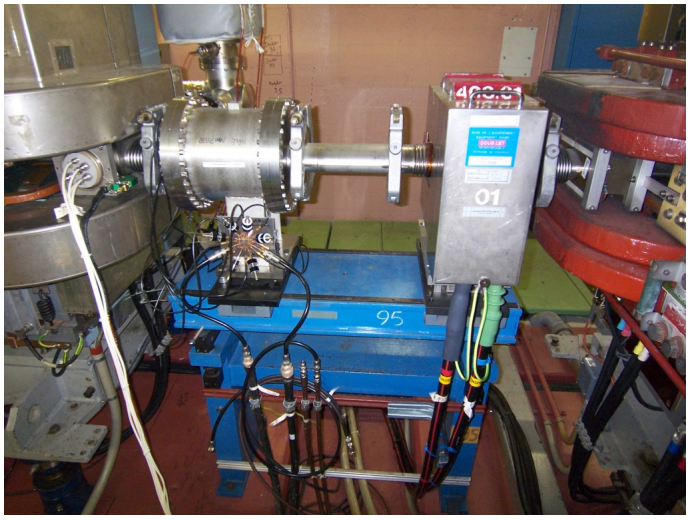

Figure 3.8. Pickup in SS95 used to acquire data for longitudinal measurements.

that brought me to develop a new approach.
The beam signal, coming from the longitudinal pickup in Fig. 3.8, is acquired and recorder in the PS Central building with an oscilloscope (Tektronix TDS5104) which delivers up to 5 GS/s real-time sample rate and 8 MB record length in a bandwidth up to 1 GHz. During the acquisition the trigger event defines the point in time at which a repeating "window" of waveform information is recorded. Triggering allows for an acquisition to begin when a condition is met. The oscilloscope works in a multi-trigger acquisition mode, it acquires multiple points for each trigger event, *i.e.*, the trigger is activated whenever the cycle appears in the supercycle. A PS

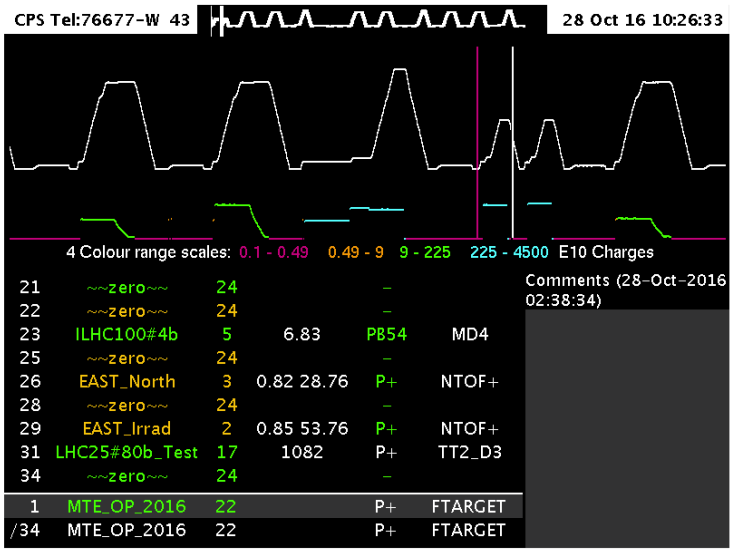

Figure 3.9. Example of a supercycle used in the PS during operation.

supercycle [8] is made of various magnetic cycles being allocated to each user; an example is shown in Fig. 3.9. The first column in white represents the position of

the user in the supercycle, in this case the supercycle was composed of 34 cycles (see bottom line); the second column is the cycle name which is usually related to the beam characteristics and the fourth one represents the intensity per particle in 10^{10} ppp. For further details we address to [9].
The rearm time, or the time when the instrument is not ready for a trigger, is extremely small, often from 1 to 100 μs, depending on the record length and the oscilloscope. This allows to capture data if the triggers occur 100 μs apart. This kind of acquisitions allows to acquire numerous triggered waveforms quickly and we are always synchronized with the beam. From each acquired window, it is possible to rebuild a limited number of turns but it is not possible, in principle, to capture the entire evolution of the beam in the cycle. In theory, one could push to the limit the conditions of measurement increasing the number of windows up to acquire the entire cycle but the trigger rearming time (*i.e.*, the distance between two successive windows) can not be ignored. The mathematical procedure to analyze the data contemplates an FFT of centroid of each bunch.
The inability to acquire the entire cycle as well as a fragmentary capture of the beam evolution is the main weakness of this technique. CB instabilities have rise times of the order of ms and they need to be identified when they still have a small amplitude oscillation in order to be damped. For these reasons during my research study I have developed an algorithm that allows to identify with a sub-ns precision the oscillation modes: a detailed description of the acquisition technique and the algorithm will now be presented.

3.4.2 My Approach to the CB Motion Analysis

1) Data Acquisition

The idea behind this approach is to use a Matlab interface to acquire and analyze beam spectra using a large memory digitiser instead of an oscilloscope. The device,

Figure 3.10. ADQ14 digitiser [10].

shown in Fig. 3.10, is the ADQ214 [10] produced by SP Devices. It is a large memory digitiser capable to work at high frequency. The large memory is of special importance since many comparable digitisers can acquire data at rates in the GHz range but due to memory limitation they can explore only limited time span. This digitiser was considered suitable for PS since it can cover a whole cycle with sufficient sampling rate.
Some of its features are summarized in the following:

- 2 channels
- 14-bit resolution
- Memory of 64 Msamples for each of the two channels
- Sampling frequency 800/n MHz n=2,. . . ,20
- 400 MS/s sampling rate
- AC/DC coupling
- 850 MHz analog bandwidth.
- Clock reference input and internal clock source as well as a connector for direct external clock.

According to the user requirements, it is possible to acquire the data in the triggered streaming mode, optimized for data transfer to host computer, or in the multi-record mode, optimized for real time capture of large amount of data. The ADQ214 is provided with an easy-to-use API that allows easy integration into any application, software tools for application development include Matlab for Windows. At CERN, a Matlab class and a Matlab GUI were previously developed for data acquisition with this instrument [11].

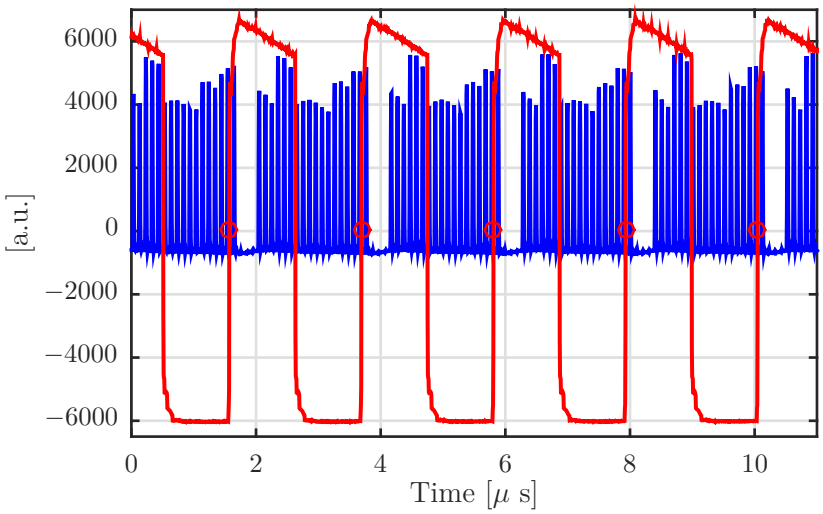

Figure 3.11. T_{rev}(red) and longitudinal bunch signal (blue) as acquired from a wall current monitor.

The typical setup used in acquisition consists in the beam signal from the wall current monitor acquired on Channel 1, the T_{rev} signal recorded on Channel 2 and the internal clock. As external trigger we used the one provided by the accelerator central system to be synchronous with the machine cycle; the sampling frequency is f_s= 400 MHz (841 points to reconstruct one revolution period). This choice allows,

with 64 Msamples memory, to record 160 ms, about ∼80k turns. This time range of acquisition is acceptable since it is of the same order of magnitude of the CB time constants observed in the PS.

2) Data Analysis

Now that we have introduced the instrument setup, we will go into the details of the different steps of the data analysis: load and synchronize the beam signal, gate and upsample each T_{rev}, evaluate the centroid evolution of each bunch and finally use the matrix formalism introduced in Chapter 1 to evaluate the CB modes amplitude and phase.

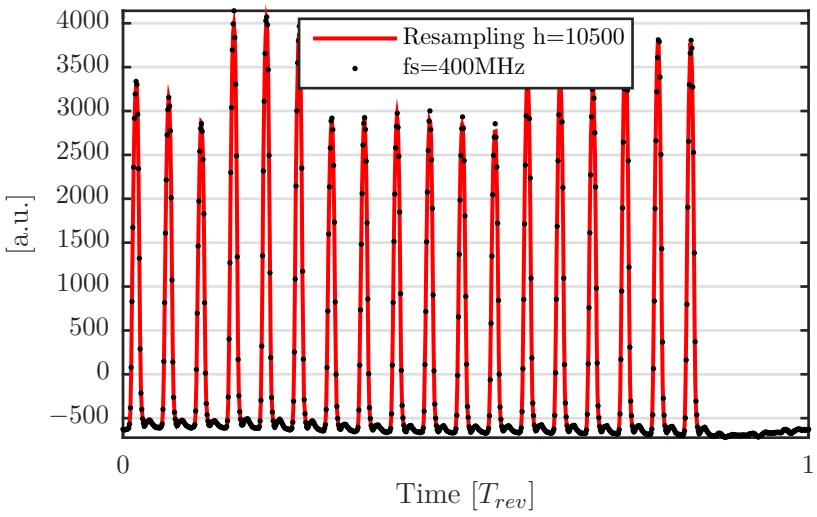

Figure 3.12. A single revolution period normalized between 0 and 1; in red is shown the resampled longitudinal profile signal in h =10500, in black dots the original signal in h =841.

Step 1: Load and Synchronize the Beam Signal. We start the signal acquisition during acceleration immediately after transition crossing. The Matlab interface loads both the T_{rev} and beam signal as in Fig. 3.11. By using the 400 MHz clock of the ADQ21 we need to resynchronize the beam signal to the revolution frequency. This is achieved by using Channel 2, where we read the T_{rev} (h =1 $\simeq$ 435 MHz): the even zero-crossing of the T_{rev} (rising edge) is selected to reconstruct each revolution period in the machine. For this kind of measurements it would be easier to use an external clock locked to the RF of the machine but, at present, this type of hardware solution is not available.
The target, in the algorithm development, was to observe the centroids oscillations in the sub-ns range to intercept these oscillations when their amplitude was still small, about $\sim 1^\circ$ of the RF bucket, which is approximately in the range of $\sim$ ns. The technique described in Section 3.4.1 does not allow to observe the centroids

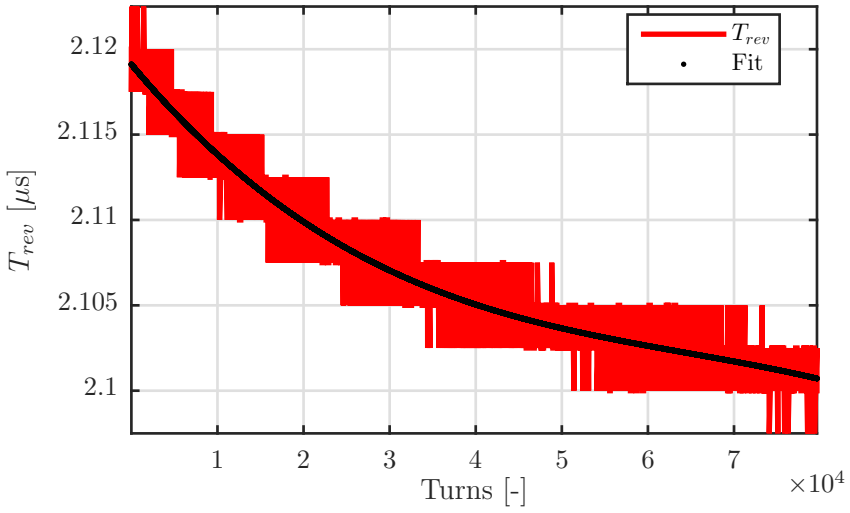

Figure 3.13. T_{rev} signal along turns as from analysis and its fit.

oscillations with this accuracy since in that case the acquisition is fragmentary and the instrument does not allow to record such a huge amount of data.

Step 2: Gating and Upsampling each T_{rev}. Once the T_{rev} and the beam signals are sampled in $h \simeq 841$, the next step is to normalize each T_{rev} respect to $h = 21$. At this step in fact each T_{rev} has a different number of samples, which is not even multiple of the harmonic 21. For a proper gating of the 21 buckets we decided to perform an upsampling of the beam signal. We made a study and found a convergence from $h = 10500$: with this number of points, multiple of 21, it is possible to reconstruct with precision the centroid oscillations.
Subsequently each revolution period is normalized to T_{rev}. In Fig. 3.12 we can see one revolution period in the machine; the longitudinal beam profile is represented with both curves: the resampled one, with 10500 points, in red and the acquired one, with $\simeq 841$ points, in black. The resampled curve has a number of points that allows to describe with sub-ns precision the oscillations of the centroids.

Step 3: Evaluate the Centroid Evolution of Each Bunch. From the algorithm it is possible to reconstruct the evolution of the revolution period in the machine as during the acquisition. The computed T_{rev} is shown in Fig. 3.13. It is possible to notice a stepped behavior, where each step is $\sim$2 ns width: this error value can be associated to the sampling at 2.5 ns. The error in the revolution period induces an high frequency jitter on the centroids oscillations, one example is plotted in black in Fig. 3.14. To remove this unphysical component of the oscillations we first fit the T_{rev} signal, as in Fig. 3.13, and find the best approximation, than evaluate the error in the period by subtracting the fit and the original T_{rev} and use this error to correct each centroid evolution. Fig. 3.15 shows the resulted centroid

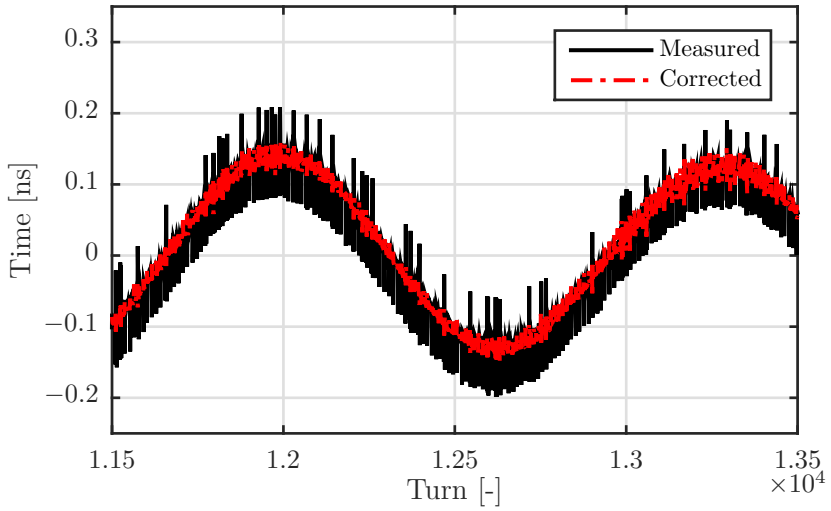

Figure 3.14. Centroid evolution for a single bunch before (in black) and after (in red) removing the dilatation motion due to the error in the T_{rev} signal.

oscillation for 4 bunches: we observe, for each bunch, a longitudinal oscillation of the centroid up to 1 ns peak, with a precision well below the limit of 2.5 ns of the sampling.

Therefore with this technique we can, not only acquire a large time interval and observe the evolution of the centroid up to 160 ms but, with the proposed post-processing, we can reach a precision in the observation of the bunch centroid motion in the sub-ns range. Achieving this kind of precision is an excellent tool to understand the CB oscillation underlying beam physics.

Step 4: Evaluate the CB Modes Amplitude and Phase. Once the centroid evolution has been corrected and smoothed, it is possible to fit it with a function of the kind: $y_{fit} = b + a \cdot cos(2\pi Q_s N + \phi)$, by using moving windows that covers about two synchrotron oscillations (∼2000 turns) with a Δ offset of 100 turns between two consecutive windows (∼700 windows in total). This non linear fit reveals a limited numerical stability, so as a first iteration we evaluate Q_s and ϕ to use as initial conditions in the second fit iteration that returns amplitude a_i and phase ϕ_i of each bunch centroid turn after turn.
At this point we recall the matrix formalism introduced in Section 1.5.1. Once evaluated a_i and ϕ_i, we can calculate X_i, the phasor representing the complex amplitude of the i^{th} bunch and, using Eq. (1.68), we move in the mode space and obtain the complex matrix $\mathbf{W_n}$ which contains the information of amplitude and phase for each CB mode.
This algorithm has been used to analyze all measured data that will be shown in Section 3.5 and Section 4.2.

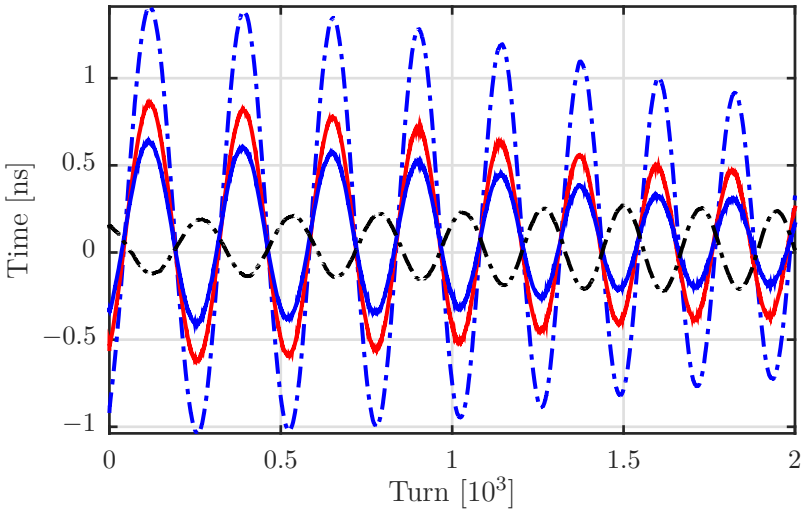

Figure 3.15. Longitudinal oscillation of bunch centroid. We can observe the sub-ns precision in the oscillation of each centroid.

3.5 Circulant Matrix Approach: Application to the PS

In this Section we will show the application of the circulant matrix algorithm within the PS. We will first study the Proton Synchrotron as a dynamic system in free evolution for an uneven fill configuration and we will determine the matrix that describes the evolution of the system and study its stability/instability. Afterwards we will focus on the forced evolution: we will open the PS longitudinal feedback loop and inject an external excitation to observe how the system reacts.

3.5.1 The Evolution Matrix of Longitudinal CB Motion

The concept of dynamical system has its origins in Newtonian mechanics. The evolution rule of a dynamical systems is an implicit relation that gives the state of the system for only a short time into the future; to determine the state for all future times requires iterating the relation many times. If the system can be solved, given an initial point it is possible to determine all its future positions, a collection of points known as a trajectory or orbit. At any given time, a dynamical system has a state given by a vector that can be represented by a point in an appropriate state space. The modal analysis is the study of the dynamic evolution of the system.

When studying the dynamical behavior of the Proton Synchrotron, two different situations can be addressed:

- **Circulant problem**: the train of bunches is regularly distributed along the machine azimuth. In this case independently from the machine impedance

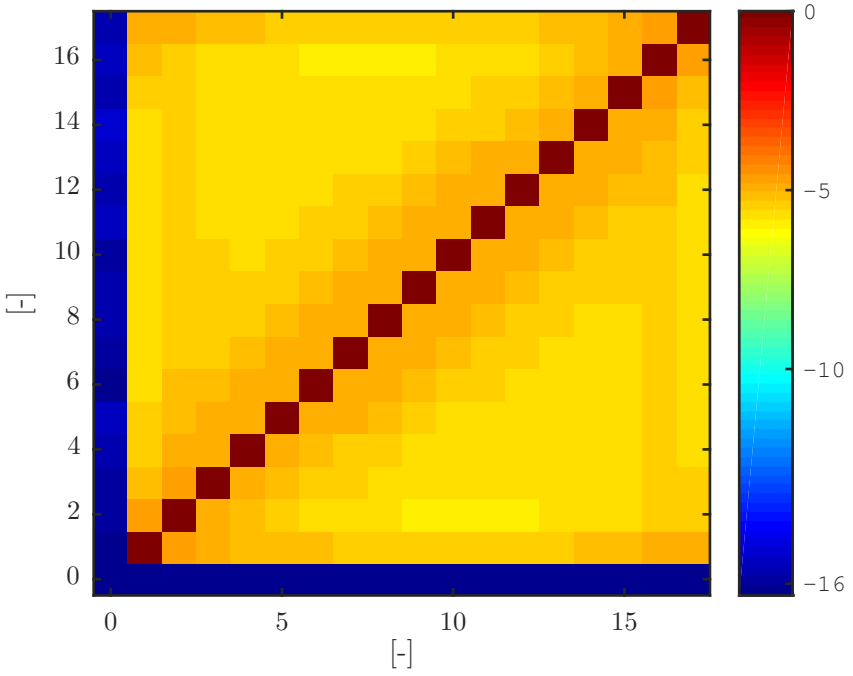

Figure 3.16. Color plot of the simulated $\mathbf{PS_{1\ turn}}$ matrix for 18 bunches in $h = 21$ after 1000 turns. The colorbar represent the $log(abs(\mathbf{PS_{1\ turn}}))$.

all the modes of the system are well known since eigenvectors are known and eigenvalues can be evaluated as explained in Section 1.5.

- **Non − circulant problem**: there is one (or multiple) gap in the train of bunches, the circularity of the problem is lost and the modes depend on the machine impedance.

In the following we address the situation of a non-circulant system by using the configuration of the nominal LHC beam with 18 bunches in $h = 21$. The aim of the study is to evaluate the matrix $\mathbf{PS_{1\ turn}}$ which describes the evolution of the system in the mode space and study its stability/instability by the eigenvalues analysis.

In Chapter 1 we introduced the equation Eq. (1.67) which describes the evolution of $\mathbf{W_n}$ (complex modes vector) in an arbitrary base (not an eigenvectors base) between turns n and n+1. It is possible anyway to rewrite this vector equation in a matricial form by substituting the vectors $\mathbf{W_{n+1}}$ and $\mathbf{W_n}$ with two matrices $\mathbf{A}$ and $\mathbf{B}$, defined as

- $\mathbf{A} = [\mathbf{W_2}, \mathbf{W_3}, \ldots, \mathbf{W_N}]$;
- $\mathbf{B} = [\mathbf{W_1}, \mathbf{W_2}, \ldots, \mathbf{W_{N-1}}]$.

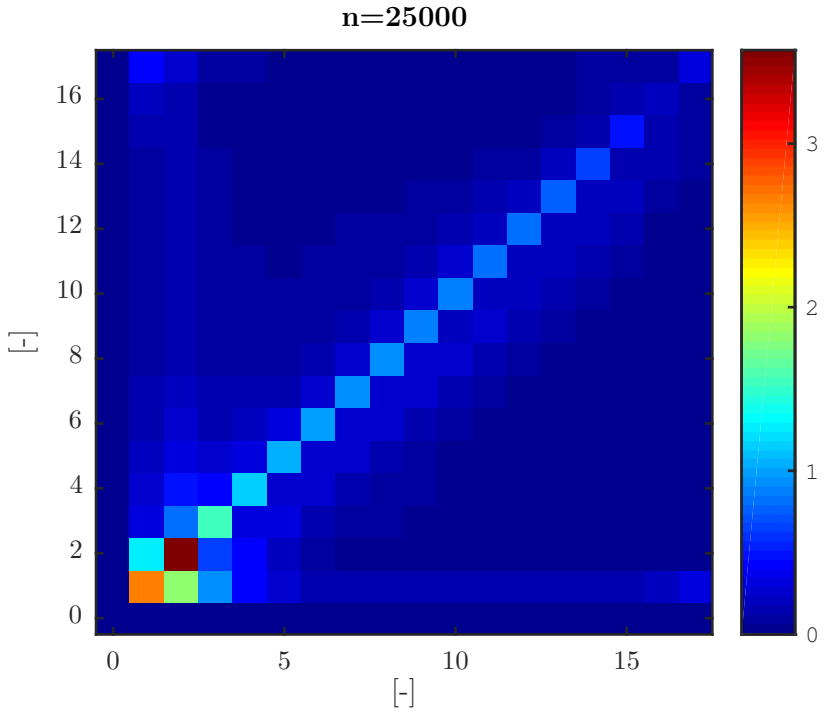

Figure 3.17. Simulated $\mathbf{PS_{1\ turn}}$ matrix for 18 bunches in $h = 21$ after 25000 turns. The colorbar represent the $log(abs(\mathbf{PS_{1\ turn}}))$.

with N the number of simulations/measurements of the modes evolution. Using this approach one can write:

$$\mathbf{A} = \mathbf{PS_{1\ turn}} \times \mathbf{B}. \tag{3.2}$$

where:

$$\mathbf{PS_{1\ turn}} = \mathbf{A} \times \mathbf{B}^{+}. \tag{3.3}$$

The matrix $\mathbf{PS_{1\ turn}}$ describes the evolution of the CB coordinates between turns n and n+1.
We performed N=100 simulations with independent initial conditions and extrapolated the modes matrix $[\mathbf{W_1}, \ldots, \mathbf{W_{100}}]$ to obtain the $\mathbf{PS_{1\ turn}}$ matrix.
The matrix $\mathbf{PS_{1\ turn}}$ is represented in Fig. 3.16 after 1000 turns to appreciate the fact that the matrix is not diagonal. The mode $\mu = 0$ has been set to zero as input of simulations.
It is interesting to observe the evolution of the $\mathbf{PS_{1\ turn}}$ matrix after many turns, since it will give an idea on how the base of vectors of the system evolves in time and which vector is the most unstable. We show, as an example, in Fig. 3.17 the matrix $\mathbf{PS^{n}_{1\ turn}}$ after 25000 turns: only the unstable vectors are visible with their elements on the diagonal, while the other vectors are less unstable or naturally damped.

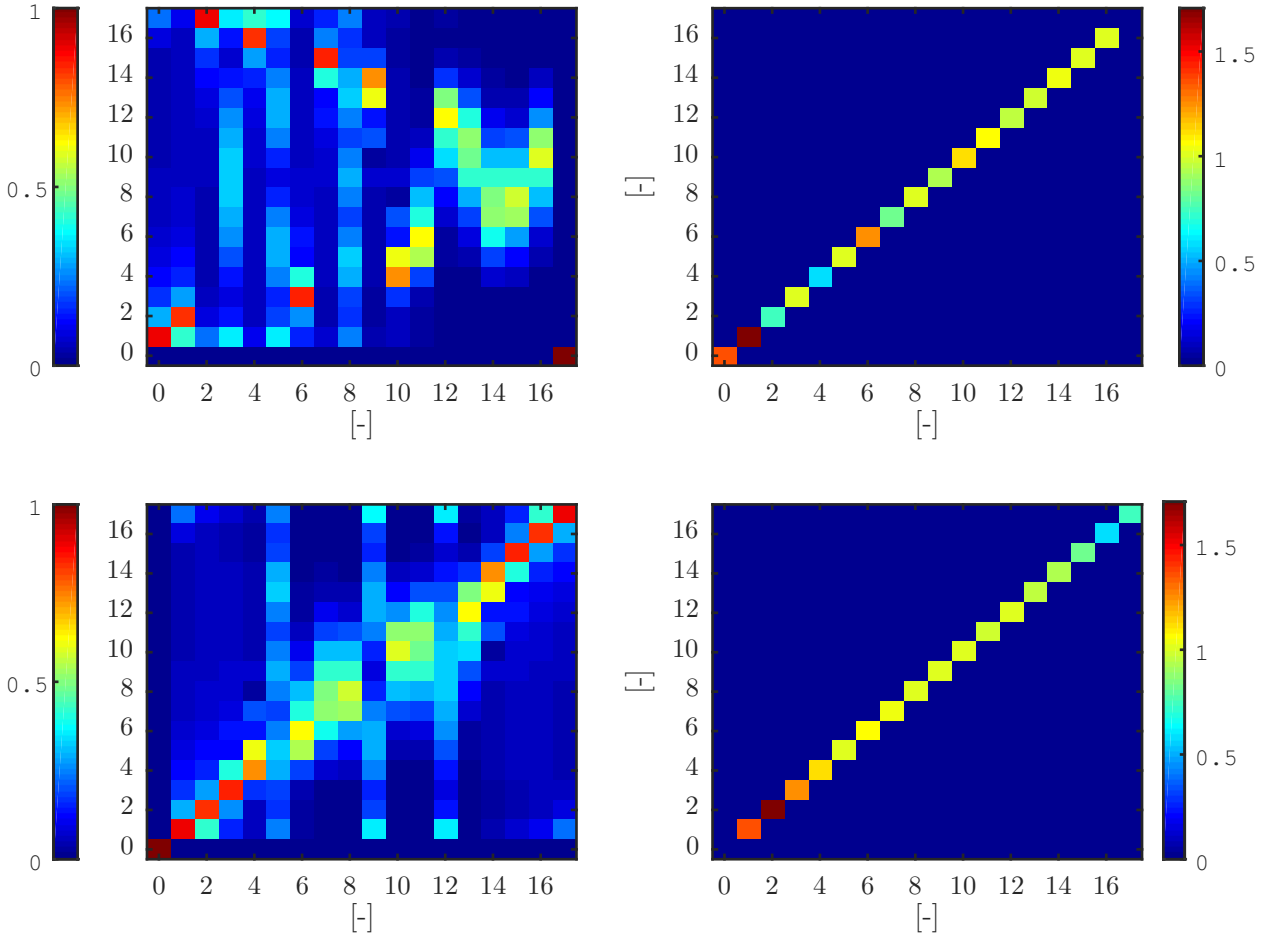

Figure 3.18. Simulated eigenvectors (top left) and eigenvalues (top right) of **PS**. The bottom figures represent the eigenvectors and eigenvalues matrices re-ordered.

The $\mathbf{PS_{1\ turn}}$ matrix describes how the frequency coordinates in this particular base of vectors get transformed due to the impedance turn after turn in the machine. If the matrix $\mathbf{PS_{1\ turn}}$ is diagonalizable it will be possible to obtain the eigenvalues $\mathbf{D}$ and consequently the real base of modes of the system. From matrix $\mathbf{PS_{1\ turn}}$ we evaluated in Fig. 3.18 the eigenvectors $\mathbf{T}$ (top left) and eigenvalues $\mathbf{D}$ (top right) matrices. $\mathbf{T}$ is a non-singular square matrix such that $\mathbf{T^{-1}\ PS_{1\ turn}\ T}$ is the diagonal matrix $\mathbf{D}$. Let multiplying both by $\mathbf{T}$, $\mathbf{PS_{1\ turn}\ T = T\ D}$. Each column of $\mathbf{T}$ is an eigenvector of $\mathbf{PS_{1\ turn}}$ whose eigenvalue is the corresponding diagonal element of $\mathbf{D}$.
The eigenvectors of $\mathbf{PS_{1\ turn}}$ form a basis if and only if $\mathbf{PS_{1\ turn}}$ is diagonalizable. A matrix that is not diagonalizable is said to be defective. For defective matrices, the notion of eigenvectors generalizes to generalized eigenvectors and the diagonal matrix of eigenvalues generalizes to the Jordan normal form. We tried to diagonalize the matrix $\mathbf{PS_{1\ turn}}$.

From Fig. 3.18 we can see that the eigenvectors are not ordered and they are grouped in clusters, symptom that with this bunch configuration (18 bunches in $h = 21$) there is not just a single correspondence between the CB mode and the sideband of the f_{rev}, but each CB mode gets excited by a cluster of frequencies.
We re-ordered the eigenvector matrix to put it in a diagonal form (Fig. 3.18 bottom left) and consequently re-ordered the eigenvalues matrix $\mathbf{D}$ (Fig. 3.18 bottom right). Once re-ordered they still verify the condition: $\mathbf{PS_{1\ turn} = T\ D\ T^{-1}}$.

This procedure allows to determine the coordinates of the modes in the generic base. We can see that the spectrum lines are not clear and isolated but there are cluster of frequencies that excite one single mode.

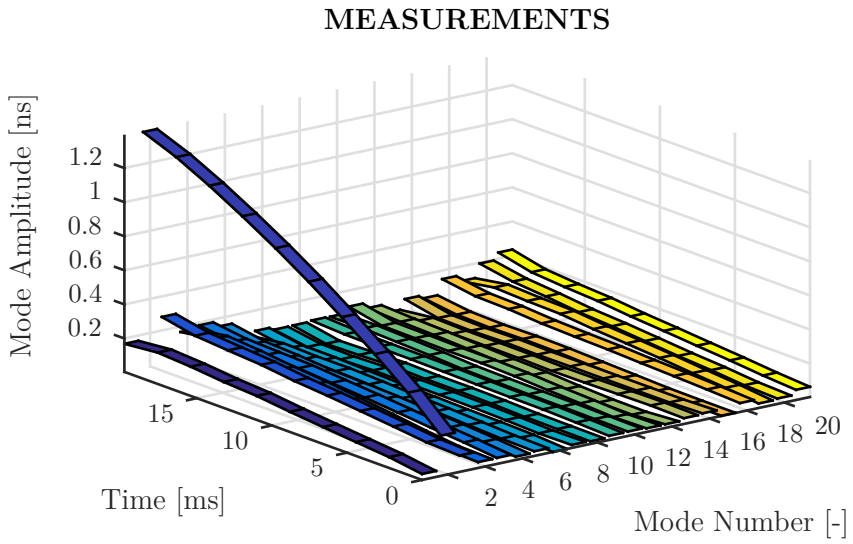

Figure 3.19. Measured excitation of mode μ =1 for 21 bunches in h =21. All the other mode are not effected since the excitation acts only on the selected synchrotron sideband.

In this case we used simulations as input but in principle it is possible to use measurements of the longitudinal beam profile. It is necessary, of course, to qualify the system above the noise level and for this purpose the measurement analysis algorithm presented in the previous Section is an optimum tool since it allows a sub-ns precision in the observation of the centroid oscillations. Then using the circulant matrix approach it is possible to obtain the modes amplitude and phase and then create the matrix $\mathbf{PS_{1\ turn}}$ to study the stability of the system.

3.5.2 The CB Excitation Matrix

In physics, for a dynamical system, a mode is a standing wave state of excitation, in which all the components of the system will be affected sinusoidally under a specified fixed frequency. Most dynamical system can be excited under several modes. Each mode is characterized by one or several frequencies, according to the modal variable

field. For example, a vibrating rope in the 2D space is defined by a single-frequency (1D axial displacement). For a given amplitude on the modal variable, each mode will store a specific amount of energy, because of the sinusoidal excitation. In this

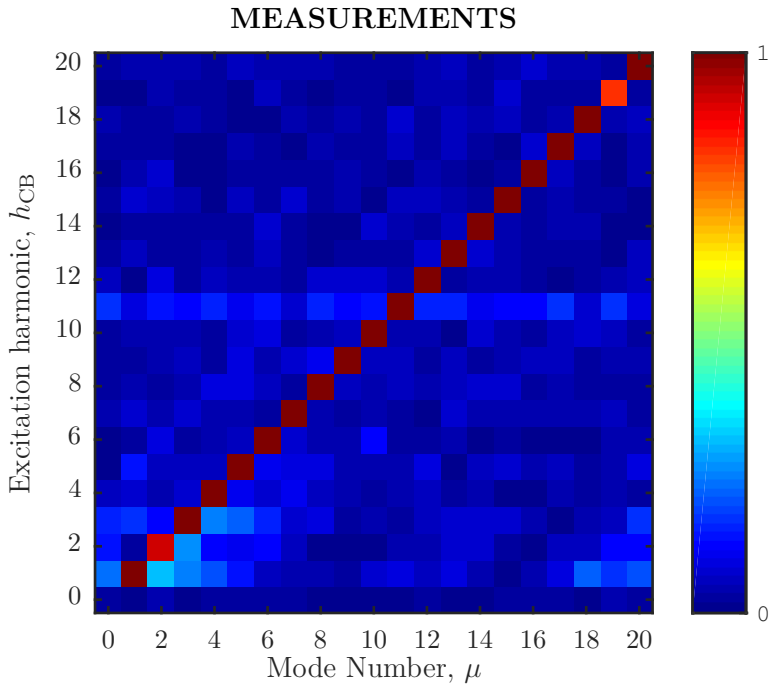

Figure 3.20. Measured matrix **F** in h =21 and 21 bunches.

Section we describe how our system reacts to an external excitation injected into the PS loop by the FB system. We will describe this behavior by the matrix **F**.

The FB system has been used to excite each synchrotron frequency sideband (upper sideband in this case) and the response of the system has been observed. We fixed a base with a well established frequency representation (in our case a single vector corresponds to one frequency line); then we excite each vector of this base and read the output (**F**) of the system in the same base. If the resulting matrix **F** is diagonal then the base we are using is a base of modes, otherwise it is just a base, and we cannot call them modes.

We will now propose two different situation. In the first one we will propose a beam configuration of 21 bunches in $h = 21$ and we will refer to it as **circulant case**: we expect the matrix **F** to be diagonal.
In the second case we will propose the nominal LHC-type beam configuration with 18 bunches in $h = 21$ and we will refer to it as $\mathbf{non - circulant\ case}$: as already obtained for the matrix $\mathbf{PS_{1\ turn}}$, we expect the matrix **F** to be non diagonal.

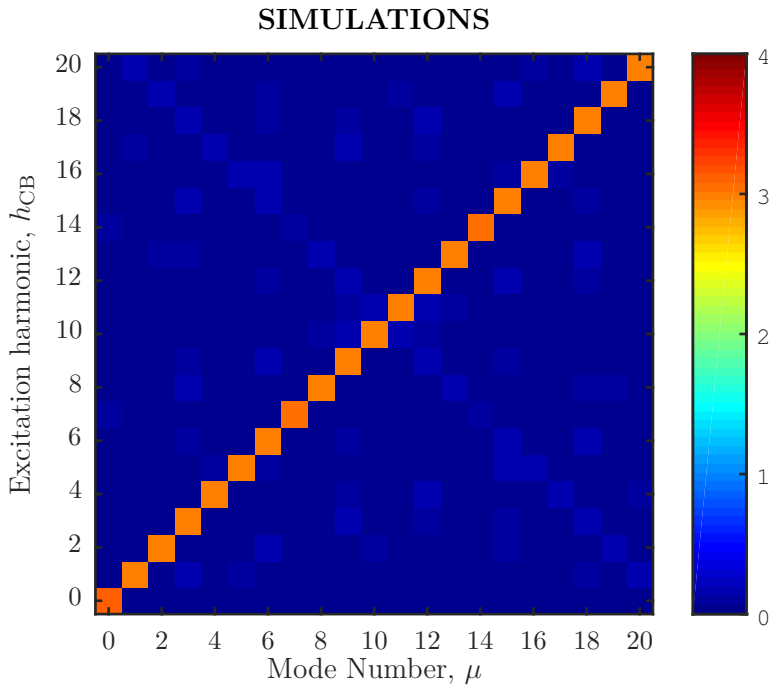

Figure 3.21. Simulated matrix **F** in h =21 and 21 bunches.

Circulant case

The result of the analysis for the excitation of a single vector is illustrated in Fig. 3.19: only the selected vector corresponding to the harmonic h_{CB} =1 is excited and all the others are not affected. We want to stress that the vector grows linearly since it is externally excited, instead an unstable one in free evolution would grows exponentially.
The excitation measurement has been repeated for $h_{CB} = [1, \ldots, 20]$ and, at the end of the process, we had 21 matrices ($21 \times N_{turns}$) in this base of representation. Then we selected from each of these matrices a vector containing the complex $\mathbf{W_i}$ information at the same turn, and we created the 21×21 **F** matrix shown in Fig. 3.20.

On the y-axis of the matrix are represented the vectors excited whilst on the x-axis are represented the vectors observed after the excitation. As expected, since the system is circulant, there is a direct correspondence between the mode we excite and the mode we observe (we can call them modes since the matrix is diagonal).

Simulations have been used to crosscheck this behavior. Using one feature of simulation code we have simulated the FB excitation voltage and we have repeated the same procedure as described above. Fig. 3.21 shows the summary of the simulations: even in this case, as in Fig. 3.20, there is a direct correspondence between the mode excited and the one observed. For both simulations and measurements, the rise

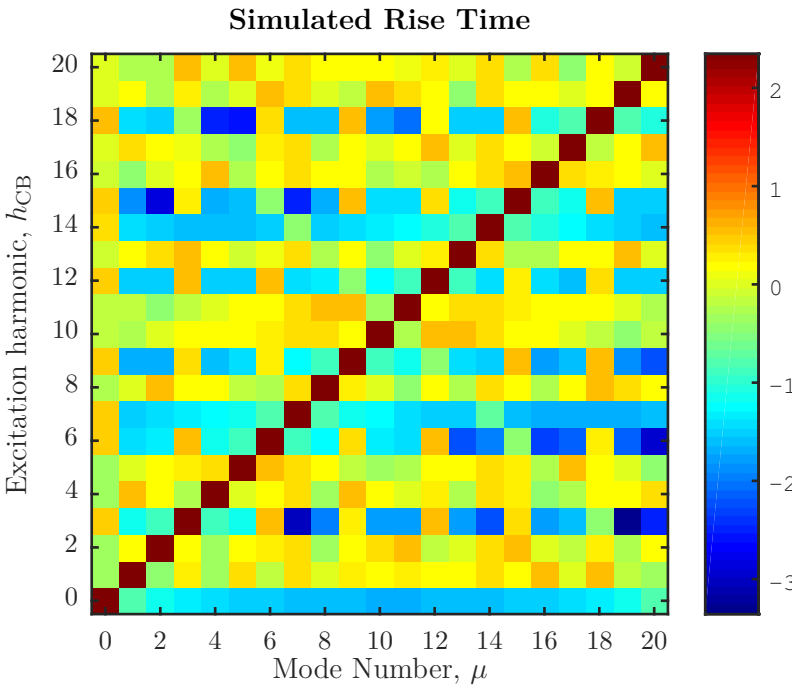

Figure 3.22. Summary of simulated rise time for each CB mode in h =21 with 21 bunches.

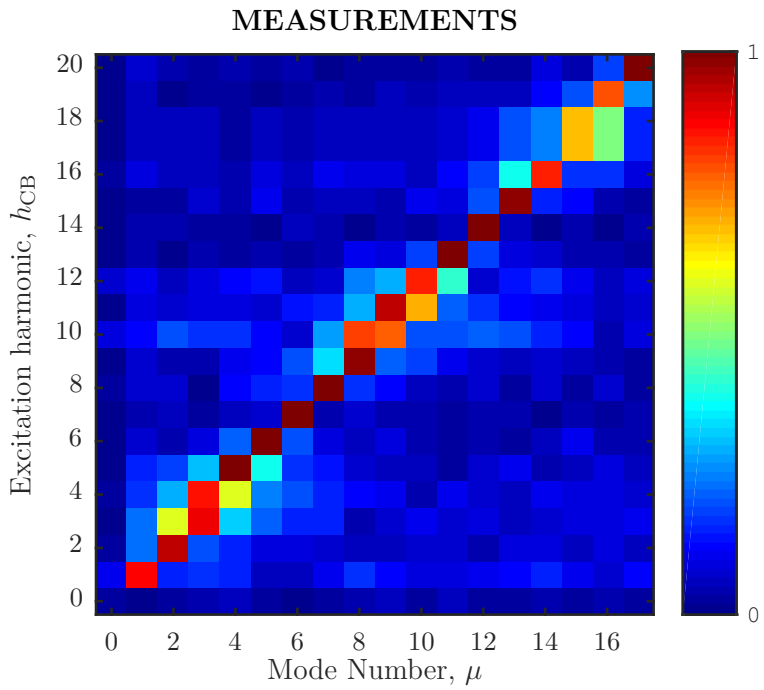

Figure 3.23. Measured **F** matrix in h =21 with 18 bunches.

time (by a linear fit) of each excited mode has been evaluated: since all the modes have been excited with the same strength and given the linearity of the system, we expected the same (linear) growth rate for each (excited) mode. In Fig. 3.22 we can see a color plot matrix of the simulated growth rates: on the matrix diagonal appears the growth rates of the excited mode and they all have the same $\tau \simeq 165$ ms, in line with the measured one, $\tau \simeq 145$ ms, while the growth rates for the other modes have negligible amplitude.

Non Circulant case

The same procedure was repeated for the nominal filling pattern configuration, 18 bunches in $h = 21$. Again we repeated the excitation procedure with the FB system and obtained the matrix **F** in Fig. 3.23. For a non circulant configuration, when the bunches are not equally disposed along the machine azimuth, if we excite a single sideband in the beam spectrum (h_{CB}), we observe a cluster of excited "modes" disposed on the matrix diagonal; we can consider this measured base close to a base of modes. Even in this case the measurements have been crosschecked with simulations, showing a good agreements in terms of the excited modes and rise times.

3.6 Summary

In this Chapter I presented the tools used during my analysis to study the CB motion in the PS. I have described the simulation code MuSiC and its application to the PS machine to extrapolate the modes and their evolution in different machine configurations.

The impedance contribution of the RF equipment was analyzed and from simulations it was possible to show that the 10 MHz system is the main source of instabilities. It was confirmed that the contribution of the Finemet cavity to the couple-bunch instability is negligible compared to the stronger effect of the 10 MHz cavities. Simulations with the new intensity provided by the LIU project are in line with expectations.

I presented an original algorithm that allows a sub-nanosecond detection of the bunch oscillations and allows to perform the mode analysis to study the system stability. This approach has been applied to the PS for the nominal filling pattern to evaluate the evolution matrix of the system and the base of modes for this non circulant configuration.

Bibliography

[1] D. Boussard, "Observation of microwave longitudinal instabilities in the PS," *LabII/RF/Int./75-2*.

[2] R. Garoby, "Bunch merging and splitting techniques in the injectors for high energy hadron colliders," *CERN/PS 98-048 (RF)*.

[3] Y. B. et al., "High intensity phenomena observed in the CPS ," *4th IEEE Particle Accelerator Conference, Chicago, USA, pp.1027-1031*, 1971.

[4] H. Damerau, "Longitudinal coupled-bunch instabilities in the CERN PS," *Proceedings of PAC07, Albuquerque, New Mexico, USA*, 2007.

[5] H. Damerau, "Longitudinal performance with high-density beams for the LHC in the PS," *Proceedings of HB2010, Morschach, Switzerland*, 2010.

[6] M. Migliorati and L. Palumbo, "Multibunch and multiparticle simulation code with an alternative approach to wakefield effects," *Phys. Rev. ST Accel. Beams 18, 031001*, 2015.

[7] L. Ventura, "Study of longitudinal multibunch instabilities for LHC-type beams at the CERN Proton Synchrotron," *CERN Thesis*, 2014.

[8] D. J. Simon, "The CERN PS complex: a versatile particle factory," *Proceedings of the fifth European Particle Accelerator Conference, Barcelona, Spain, p. 295*, 1996.

[9] "CPS Vistar."

[10] "SP Devices, ADQ214," *http://spdevices.com/index.php/adq214*.

[11] A. Valimaa, "A Matlab Interface to Acquire and Analyse Beam Spectra Using a Large Memory Digitiser ," *CERN-STUDENTS-Note-2014-147*, 2014.

Chapter 4

The Longitudinal CB Feedback System and its Performance

In this Chapter we will review the keys parameters of the PS coupled-bunch feedback system, starting from a description of the signal chain including signal pickup, signal processing and wide-band kicker. We will report on the commissioning experience and performance of the FB system. Finally we will show the achieved beam performance with LHC-type beams in 2016.

A feedback system is based on sensors capable of detecting the unwanted beam motion and actuators that apply the feedback correction to the beam. The advances in electronic technology now allow the implementation of feedback loops using programmable digital systems; besides important advantages in terms of flexibility and reproducibility, digital systems open the way to the use of novel diagnostics tools and additional features. Depending on how a feedback system detects and controls instabilities, there are two main feedback categories: 'mode-by-mode' and 'bunch-by-bunch' feedbacks. The former are often referred to as 'frequency-domain', the latter as 'time-domain' feedbacks [1].

A **bunch by bunch feedback** (time domain) individually kicks each bunch by applying small kicks every time the bunch passes through the kicker. The result is a damped oscillation. There are as many processing channels as the number of bunches. Since the bunch oscillation is sinusoidal, the turn-by-turn position of the bunch measured at a given location is a sampled sinusoid. Consequently, the kick signal applied by the actuator to each bunch can be generated by shifting by $\pi/2$ the signal of the position of the same bunch when it passes through the kicker.

In a **mode by mode feedback** (frequency domain) each mode is identified with the help of a special narrow band filter centered around one of the revolution harmonics. Each mode is then processed individually leading to a feedback that consists of many narrow band systems running in parallel. With a mode-by-mode feedback each coupled-bunch oscillation mode is detected separately with a pass-band tracking filter centered around the revolution harmonic corresponding to the mode number. Additionally, the spectral component at the revolution frequency is removed by a

narrow-band notch, keeping only the synchrotron frequency side-bands. The filtered synchrotron frequency side-band signals are then de-phased, amplified and fed back to the beam via a longitudinal kicker. Historically in the PS a mode-by-mode FB

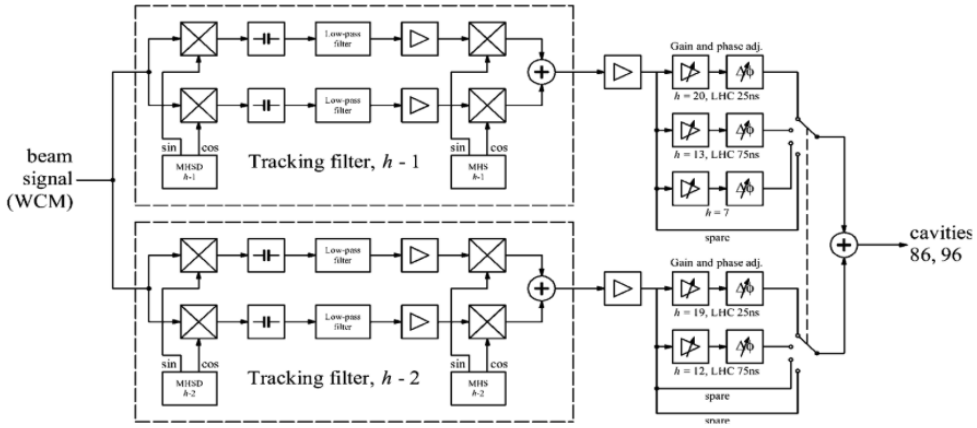

Figure 4.1. Analouge signal processing for the PS FB system as it was until 2014 [2].

system has been the primary tool to address the CB instability issue; in fact while a time domain FB requires precise synchronous phase measurements, sweeping the T_{rev}, to know a priori the exact position of each bunch, a frequency domain FB is insensitive to the bunch phase and to the filling pattern since the FB acts on the sidebands of the revolution frequency. During the commissioning of the PS as a pre-injector for LHC, to improve longitudinal beam stability, a first dedicated coupled-bunch feedback was installed in 2005. Lacking a separate longitudinal kicker two 10 MHz accelerating cavities, C86 and C96, driven by the signal from the feedback low-level electronics were used as longitudinal kickers. In addition to the 20 kV of voltage at the acceleration harmonic $h = 21$, they produced a few kilovolts at once and twice the revolution frequency (∼470 kHz and ∼940 kHz) below their resonance frequency for the damping of coupled-bunch oscillations. The analog signal processing is shown in Fig. 4.1. With this configuration it was possible to cover only two adjacent unstable modes due to the bandwidth shape of the RF cavity. To overcome these limitations at least for studies in preparation of the coupled-bunch FB, the spare 10 MHz cavity has been operated as a FB kicker; this allowed to make an accurate study program before installing the new damper. The detailed simulation and measurements study of this stage can be found in [3].

In the framework of the LIU Project, it has therefore been decided to remove the reduced bandwidth limitation by installing a dedicated, wideband kicker based on the wideband frequency characteristics of Finemet magnetic alloy and driven by solid-state amplifiers. A new fully digital LLRF has been designed [4] to substitute the analog signal processing.

The Longitudinal Wide-Band Kicker and FB Signal Processing

We introduced the Finemet cavity already in Section 2.4, giving technical details and proposing the impedance model. In this Section we want to give additional

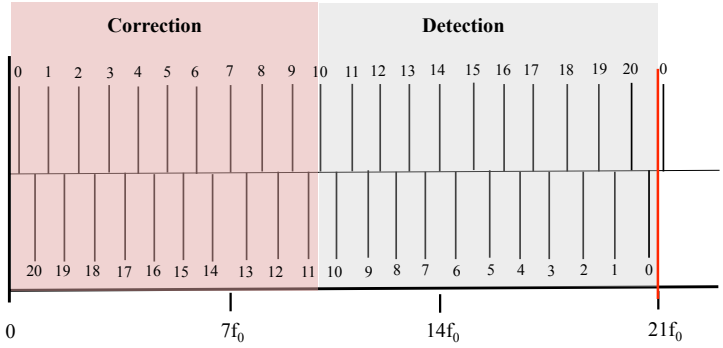

Figure 4.2. Sketch of beam frequency spectrum in $h = 21$ and Finemet cavity preferred damping and kicking frequency choices.

information regarding its role as a damper. All CB modes appear twice in a band between two revolution frequency harmonics (see Fig. 4.2 for the specific case of the PS in $h = 21$), once as upper sidebands and once as lower sideband in a band $N_b f_0/2$ from one bunch harmonic to the symmetry point between two bunch harmonics. This involves that all modes can be damped with a feedback system bandwidth equal to half the bunch frequency.
In the PS CB oscillations are observed during acceleration in $h = 21$, at 10 MHz; due to the symmetry of sidebands, the kicker cavity should cover the frequency range either from ∼0.4 to 5.5 MHz or from ∼4.5 to 10 MHz. The lower frequency range has been adopted for the kicker cavity (from f_{rev} to $10 f_{rev}$); for the detection of the weak synchrotron frequency sideband close to the revolution frequency harmonics, the upper frequency is preferred (from $11 f_{rev}$ to $21 f_{rev}$), as in Fig. 4.2.
This avoids the need to extract the synchrotron frequency sidebands close to the first few harmonics of the revolution frequency, while the Finemet kicker cavity can operate in an optimum frequency regime for this cavity type. The low-level (LL) RF system uses the feedback board originally developed for the one-turn delay feedback [5], avoiding the need for dedicated hardware. The system provides two major functionalities:

- i) reduce beam loading by impedance reduction of the Finemet-type wideband kicker cavity at the revolution frequency harmonics;
- ii) detect and damp synchrotron frequency sidebands associated to the presence of coupled-bunch oscillations.

The two distinct loops are visible in Fig. 4.3. The CB FB has as input the signal from the wall current monitor, and drives its output signal to the Finemet cavity; for the beam-loading compensation, the FB to reduce the cavity impedance at the revolution frequency harmonics takes as input the gap return signal from the cavity and feed the output signal back to the cavity itself. A simplified block diagram of the signal processing implemented for the longitudinal CB feedback only is shown in Fig. 4.4. Since the revolution frequency varies during acceleration cycle, precise tracking and phase control of the filters are required. This is achieved by means of pass filters where a low pass to band pass transformation take place, and the center

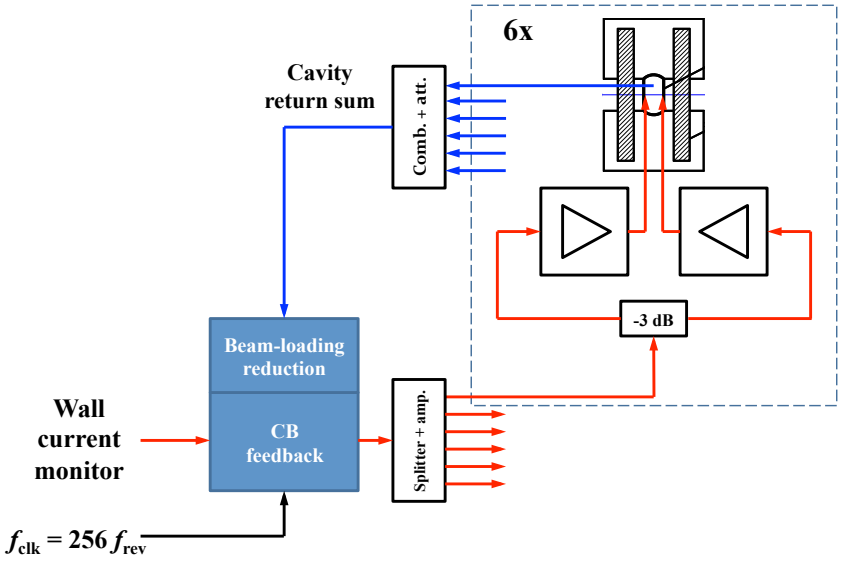

Figure 4.3. Basic sketch of the LLRF for the wide-band kicker [4].

frequency is determined by the frequency of the local oscillator signals applied to the mixer in quadrature. The beam phase is detected and then down-converted through

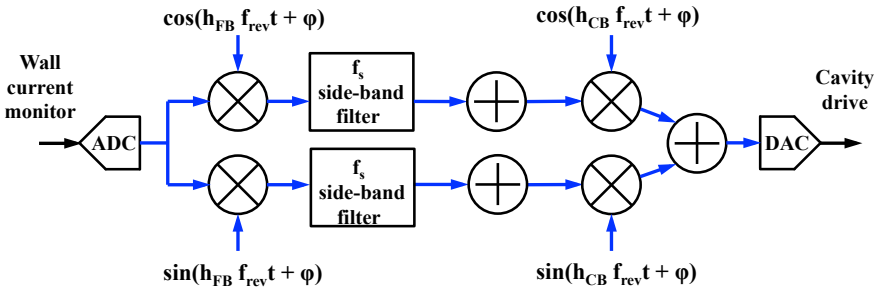

Figure 4.4. Coupled-bunch feedback system signal processing [4].

a local oscillator at harmonic h_{FB}. A bank of narrow-band pass filters allows a sharp attenuation to separate $\pm f_s$ of sidebands from the f_{rev} harmonics. In Fig. 4.5 the measured transfer function for one of the signal processing chains is shown; the center frequency is 10 MHz, corresponding to the $h = 21$ at f_{rev} =500 kHz. The f_{rev} harmonics are attenuated by more then 40 dB compared to the sidebands at $\pm f_s$ (∼300 Hz) and a precise 180° phase jump at center frequency is visible. The same behavior is repeated for all f_{rev} in $h = 21$. Due to the symmetry of the beam spectrum the signal can then be up-converted at harmonic h_{CB} so that the sum of down and up conversion harmonics becomes $h_{FB} + h_{CB}$ =21, the RF harmonic. The resulting signal is sent to the longitudinal kicker.

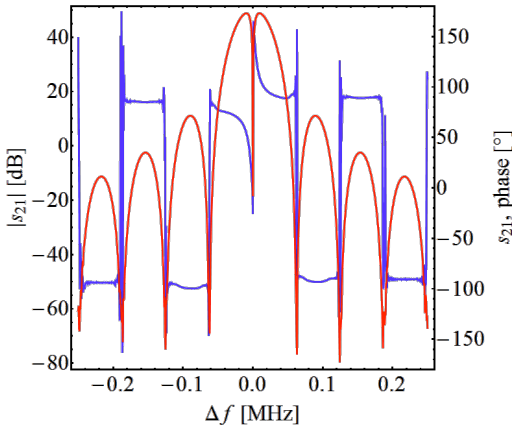

Figure 4.5. Transfer function measurements for one signal processing chain [4].

After its installation in early 2014 an extensive machine development program has been carried out to qualify the new Finemet wide-band damper cavity and its digital coupled- bunch LLRF FB system. The complete prototype feedback chain of pick-up, digital processing and Finemet kicker has been commissioned. Full tests and characterization are presented in the following Section.

4.1 Commissioning of the CB Feedback

To explore the functionality of the Finemet cavity and the correct behavior of the new digital FB system, during 2015 a dedicated measurement campaign has been performed. CB oscillations have been excited with the cavity around each harmonic of the revolution frequency with both a uniform and nominal filling pattern. In the following the measurements procedure and results are presented.
For the CB FB commissioning phase it was decided to fully explore the FB functionality and its interaction with the beam; as shown in Fig. 4.6 the initial part of the chain of the signal processing in Fig. 4.4 (down-conversion and f_s filtering) has been substituted by an external perturbation: a low frequency numerical oscillator (DDS) in the firmware of the LLRF was used to excite the beam with the Finemet cavity. During the measurement campaign we used an intensity of $\sim 1.3 \cdot 10^{11}$ protons per bunch (ppb) (this is the intensity at extraction energy, for measurements performed during acceleration, the intensity is 4 times this value) and we excited the beam for 25 ms. After having switched off the excitation, the longitudinal position of the bunches has been recorded using the digitiser introduced in Chapter 3 with the already illustrated setup. The mode analysis technique with circulant matrix approach has been adopted to extract the evolution of amplitude and phase of the dipolar modes. The system illustrated in Fig. 4.6 allows to inject an excitation RF signal at a frequency:

$$f_{CB} = h_{CB} f_{rev} \pm f_{exc}, \tag{4.1}$$

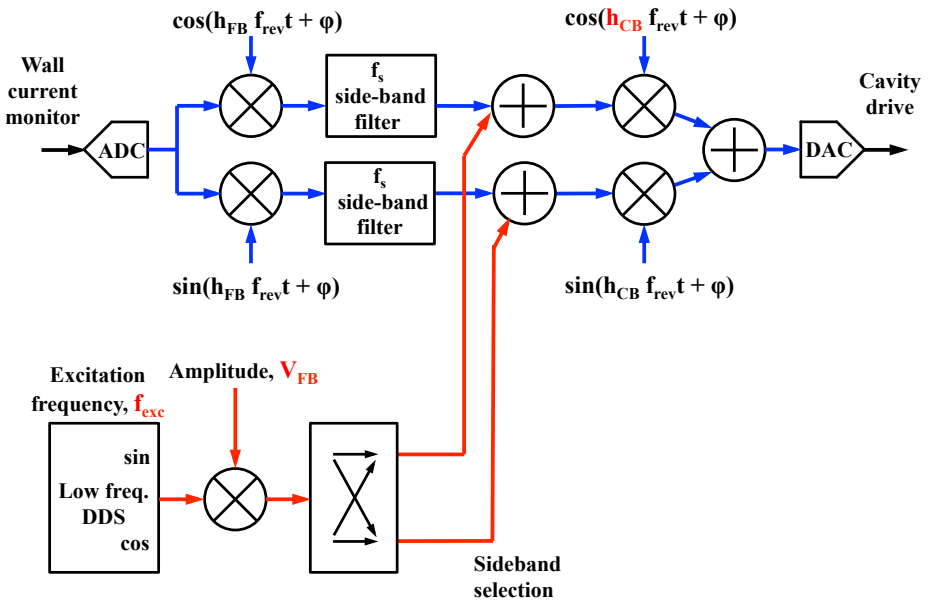

Figure 4.6. Coupled-bunch feedback system signal processing and excitation setup.

where $h_{CB} = 0 \cdots h-1$, and f_{exc} is the parameter that allows to select the synchrotron frequency sideband. We performed scan measurements on each system's key parameter (see Fig. 4.6):

- f_{exc}: to explore the sensitivity of the excitation
- h_{CB} to verify that the Finemet cavity could excite independently all the dipolar modes
- V_{FB} to test the linearity of the excitation.

In the following measurements, results and conclusions are presented.

4.1.1 Excitation Frequency Scan

A preliminary set of measurements was necessary to explore the sensitivity of the excitation with the new wide-band cavity.
Keeping the voltage, V_{FB}, constant and choosing a specific CB oscillation mode, h_{CB}, the excitation frequency f_{exc} was scanned between 0 Hz and 440 Hz with a 50 Hz step for all the modes in $h = 21$.
An emblematic measurement is shown in Fig. 4.7 where the amplitude evolution of $h_{CB} = 1$ mode versus time for two different values of f_{exc} is represented. As expected, for f_{exc} =0, no excitation was observed since we were exciting the beam at the revolution frequency harmonic $h_{CB} f_{rev}$. During the frequency scan CB oscillations appear as f_{exc} approaches the synchrotron frequency and actually a beating behavior

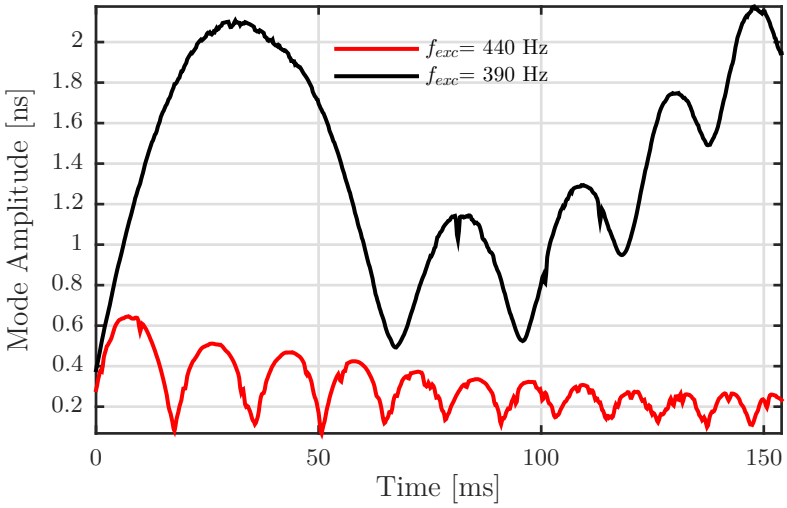

Figure 4.7. Plot of $h_{CB} = 1$ mode amplitude versus time for two different values of f_{exc}.

of excitation versus synchrotron frequency is detected for the mode amplitudes. We can observe that at $f_{exc} = 390$ Hz, the oscillation mode amplitude grows almost linearly for about 25 ms until a beating behavior appears while at $f_{exc} = 440$ Hz, a beating at approximately $f_{exc} - f_s$ is observed. This behavior can be modeled as an excited harmonic oscillator. In this particular case, we are applying a constant excitation but in the meantime the tune Q_s in the PS is changing since we are measuring during acceleration: each time we approach the correct f_{exc}, the tune changes and we are out of resonance. We can conclude that the Finemet cavity interacts with the beam as expected since as f_{exc} approaches f_s ($f_{exc} = 390$ Hz case) we start to observe a linear growth of the mode amplitude. In all the other cases (*i.e.*, $f_{exc} = 440$ Hz), we still observe the correct oscillation mode excited but the beating has an additional component since we are out of resonance ($f_{exc} \neq f_s$).

4.1.2 Excitation Oscillation Mode Scan

During the commissioning of the system one important test was to validate that the Finemet cavity could excite independently all the dipolar modes. Keeping V_{FB} constant and choosing a specific CB oscillation mode, h_{CB}, lower and upper sidebands (LSB, USB) have been excited and a mode analysis was performed.
In this case, using a constant V_{FB}=3 kV and with $f_{exc} = f_s$, we performed a scan of h_{CB} in $h = 21$ for the lower ($-f_s$) and upper ($+f_s$) sidebands (see Eq. (4.1)). Here we discuss of two emblematic examples.
During measurements we excited $h_{CB} = 18$. From the beam spectrum in Fig. 4.2 we expect to observe $\mu = 18$ if the USB is excited and $\mu = 3$ if the lower sideband is excited. The histogram plot in Fig. 4.8 represents the measured mode amplitude at a fixed machine turn for the excitation of bot upper and lower sideband. The expectation are fully confirmed and modes 3 and 18 are the most unstable.

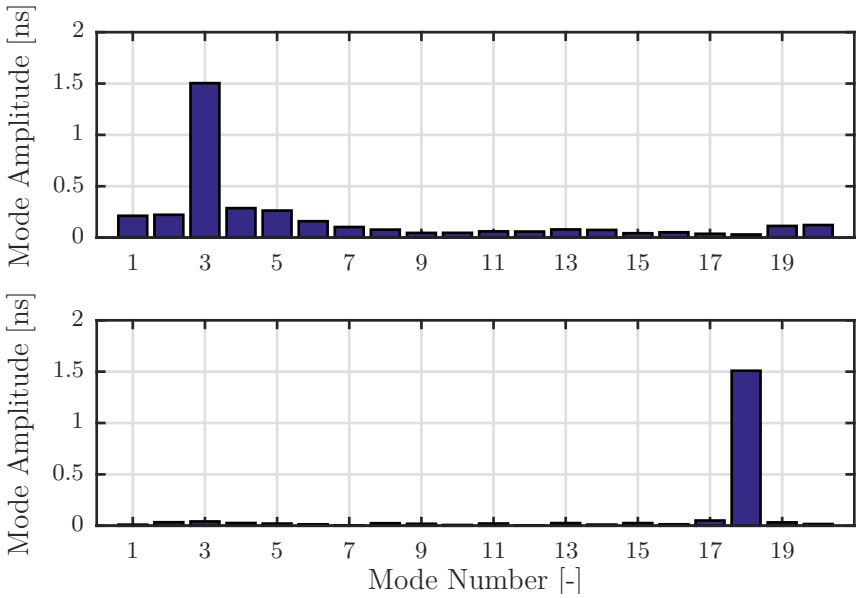

Figure 4.8. Mode amplitude for the uniform filling pattern, following the excitation of $h_{\mathrm{CB}} = 18$ LSB (top) and USB (bottom).

Another example is shown in Fig. 4.9, where we can see the amplitude of all modes in $h = 21$ following the excitation of the upper sideband of $h_{\mathrm{CB}} = 7$. We can observe that the mode grows linearly until the beating behavior appears. All the other mode are not influenced by the excitation.
These results confirm that the CB modes are well decoupled as it was observed for the first time during measurements in 2013 [6] and so, with the FB system it is possible to act with precision on the sideband of choice, without exciting any other frequency line, despite f_s is only 390 Hz distant from the correspondent f_{rev}.
A summary of the measured mode spectra following the scan of h_{CB} for the USB only, for 21 bunches in $h = 21$, was already shown in Chapter 3 in Fig. 3.20 and Fig. 3.23 for both a full machine and a nominal filling pattern.
In particular, with a batch of 18 bunches in $h = 21$, the excitation at f_{s}-sidebands of f_{rev} harmonics does not correspond to the excitation of a single CB mode, as already discussed.
A linear fit on the evolution of the amplitude for each excited mode (upper sideband excitation) was performed, and the linear growth rate, α, was evaluated. The results are summarized in Fig. 4.10 and qualitatively compared with the Finemet transfer function. Larger α are achieved for modes $h_{\mathrm{CB}} < 10$ which correspond to the frequency where s_{21} is larger, providing more voltage for the same amount of power.

4.1.3 Excitation Voltage Scan

Last test campaign consisted in checking the linearity of the Finemet cavity behavior. We choose a specific CB oscillation mode, h_{CB}, exciting only the upper sidebands and performed a scan of the voltage V_{FB} provided by the cavity. During these measurements in 2015, 4 gaps were operational, out of the 6 available, with a

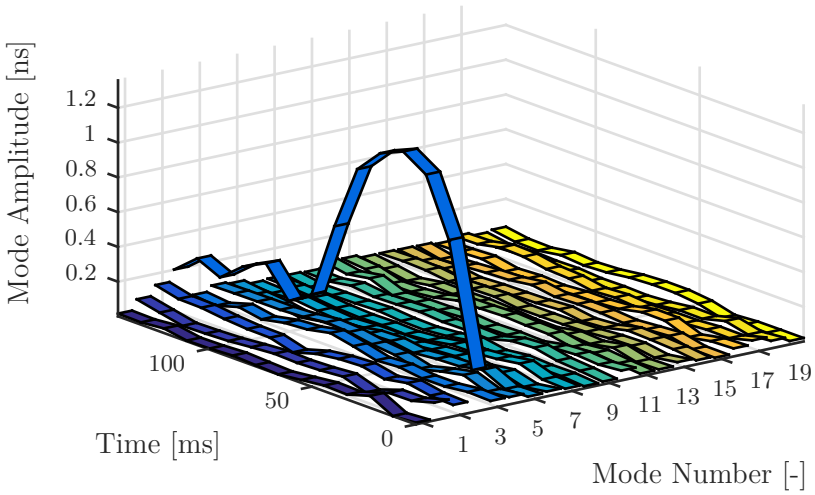

Figure 4.9. Plot of mode amplitude versus time for all the CB modes in h =21

maximum total peak voltage of 3.5 kV over 5 kV. The linearity of the beam excitation was verified by measuring the mode growth rate, as a function of V_{FB}. Fig. 4.11 shows one example measurements: the h_{CB} =1 mode amplitude has been measured for $V_{FB} = [0, \ldots, 3.5]$ kV. We can observe that when the voltage from the cavity increases, the mode amplitude follow accordingly. In Fig. 4.11 we selected the first 25 ms where the modes behavior is linear and evaluated the linear growth rates, α. The resulted analysis is shown in Fig. 4.12 where α is plotted versus V_{FB}: as expected, we are exciting the beam in a linear regime and the slope is constant. This measurement is very important for exploring the FB potential since it allows to investigate the limits of the FB.
The Finemet cavity has a total of 5 kV available to damp the unstable modes and in the commissioning phase it was important to establish if these 5 kV were sufficient to damp CB instabilities with the LIU intensity of $2.6 \cdot 10^{11}$ ppb.
We refer to the simulations of Chapter 3 in Fig. 3.7, were we showed the simulated CB modes evolution within the LIU space parameters. We performed an exponential fit on the mode μ =2 (the one that grows unstable) and evaluated $\tau^{-1} = 0.015\ ms^{-1}$, as shown in Fig. 4.13. At this point we tried to make a synthesis of simulations and measurements. We assume that the FB system cannot distinguish the mode amplitude before it reaches an amplitude of $A_{noise} = 0.7$ ns (FB system noise level limit as in the algorithm analysis). If the FB pickup can intercepts the mode just above this noise level, then the kicker has to apply a correction $\alpha = A_{noise} \cdot \tau^{-1}=$ 0.01 ns/ms to contain the mode. Even if the FB should damp all the modes, once out from the noise level, with the same voltage, we would obtain a total of $\sim$ 5 kV, the total available voltage of the cavity. From this analysis we can conclude that the maximum damping rate that the cavity can achieve is 0.25 ns/ms with 3.5 kV and simulations shows that, with the new LIU beam parameters, the FB could damp the unstable modes within the total 5 kV available.

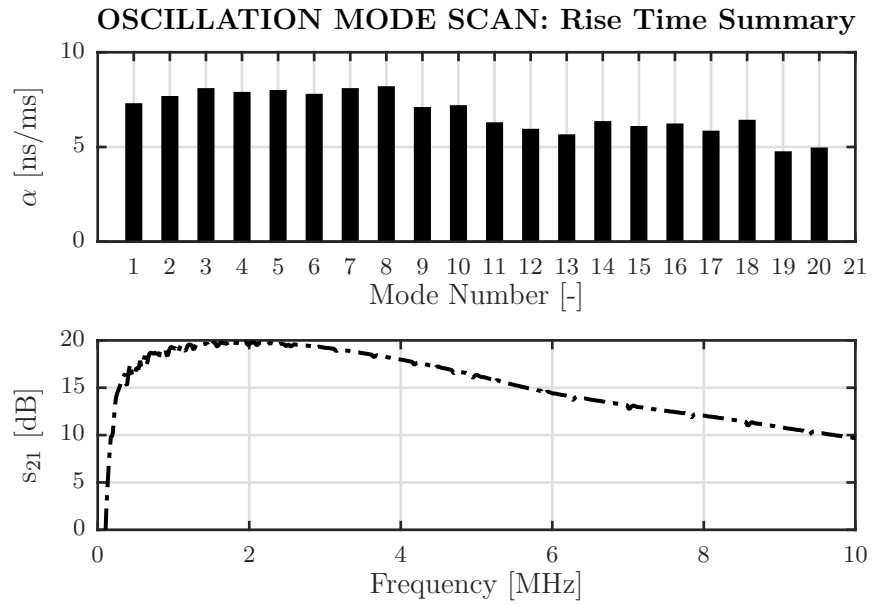

Figure 4.10. Linear growth rate versus CB oscillation mode (top). Absolute part of the Finemet cavity transfer function in logarithmic unit (bottom). Note that the measured growth rate is represented in linear scale while the transfer function in logarithmic scale.

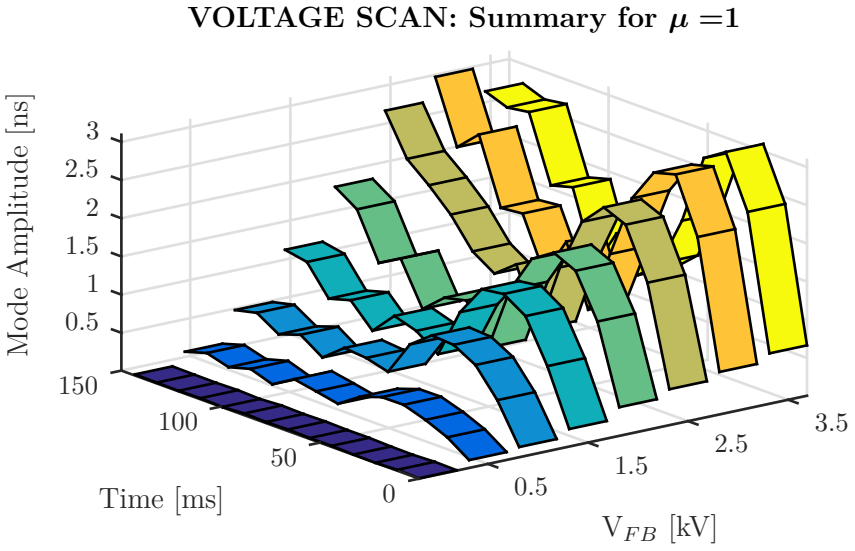

Figure 4.11. Measured amplitude of of mode h_{CB} =1 for different voltage V_{FB} from the Finemet cavity.

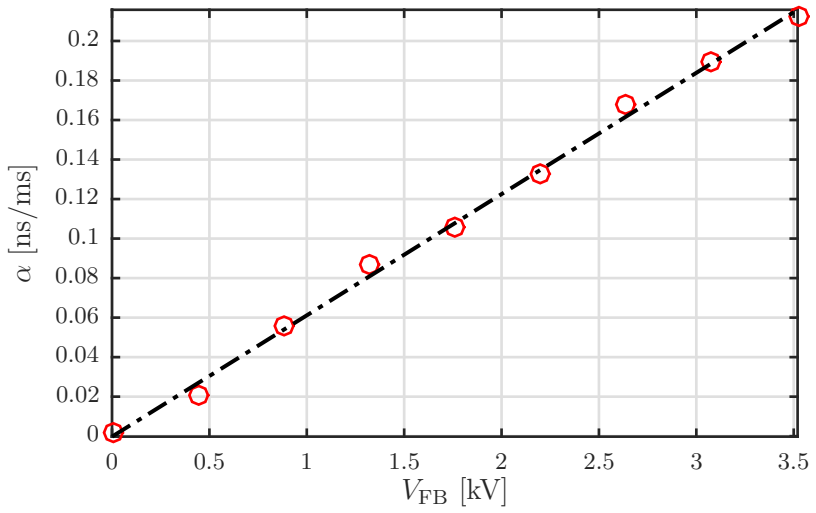

Figure 4.12. Voltage scan summary: excitation of single harmonic, $h_{CB} = 1$ (USB), and observation of the growth rate for different values of voltage, V_{FB}, from the Finemet cavity.

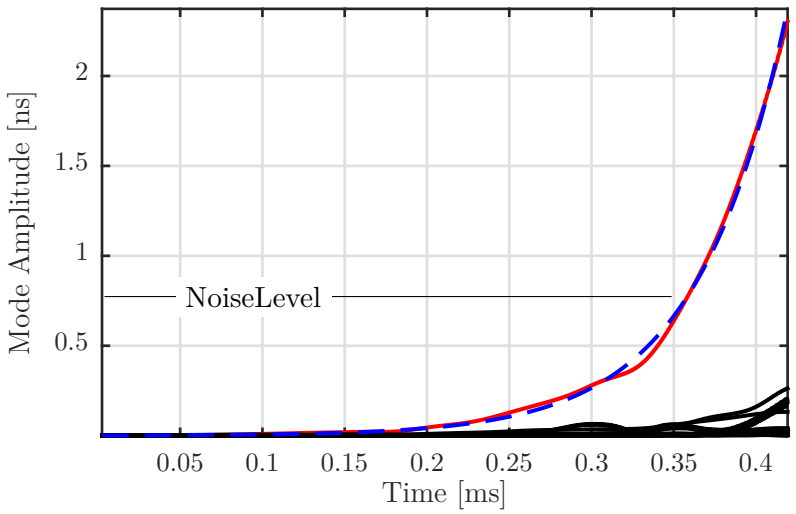

Figure 4.13. Simulated mode amplitude versus time for 21 bunches in $h = 21$ with the LIU intensity. The mode $\mu = 2$ is plotted in red line and its exponential fit in blue dashed line.

4.2 Achievements in 2016

In the previous Section we addressed the commissioning phase of the FB system and damper cavity with the purpose to explore the functionality of each block of the FB chain. We obtained results in agreement with the theory and with the FB design specifications.
The performance exploration of the longitudinal FB took place during the run of 2016 when the FB system has been actively used during the machine development cycle. A first example of the FB performance can be appreciated in Fig. 4.14, where the

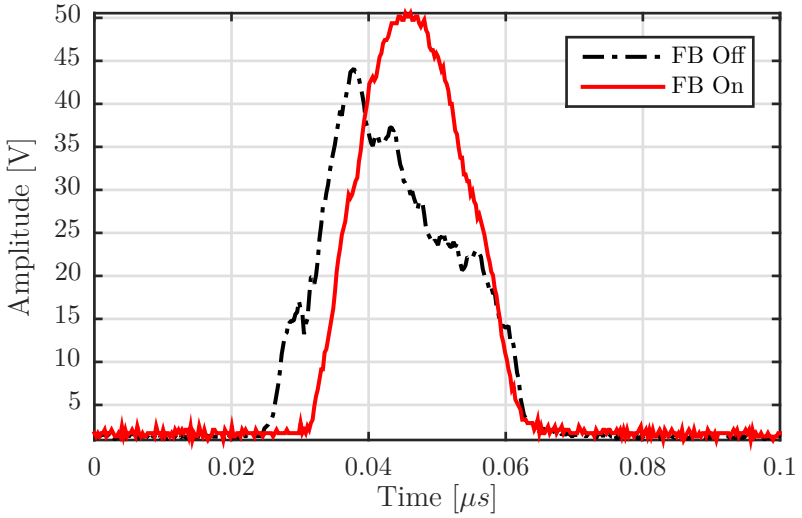

Figure 4.14. Bunch longitudinal profile at the flat-top with and without feedback.

longitudinal profile of one bunch at the flat-top with and without the FB contribute is illustrated.
If the FB is not active (black curve), the bunch shape is deeply distorted. If the FB is switched on (red curve), the bunch shape is preserved as well as its intensity and length. We can compare the unstable beam behavior at the flat-top and at the extraction presented in Chapter 1 (see Fig. 1.10 and Fig. 1.11 respectively) with the results obtained, in the same machine conditions, with the FB system, showed in Fig. 4.15 and Fig. 4.16. CB oscillations at the flat-top are damped, and at the last machine turn the beam quality is preserved and the bunch length is below the requested 4 ns.

According to the LIU-PS requirements, the intensity in the PS has to reach $2.6 \cdot 10^{11}$ ppb with a bunch length at extraction of 4 ns to be compatible with the bucket of the SPS (200 MHz RF system). Currently with the FB system we can reach an intensity of $2 \cdot 10^{11}$ ppb. When trying to increase the intensity, the FB still damp the dipolar CB oscillations but the bunches seems to perform quadrupolar CB oscillations, as in Fig. 4.17.
The coupled-bunch feedback has been designed to deal with dipolar oscillations as

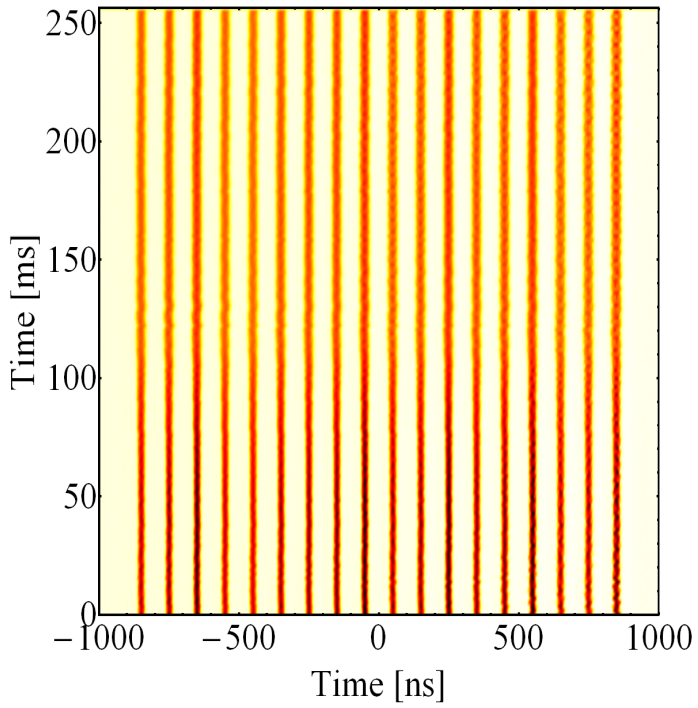

Figure 4.15. Measured bunch longitudinal oscillation observed at the flat-top in the PS with the FB active [4].

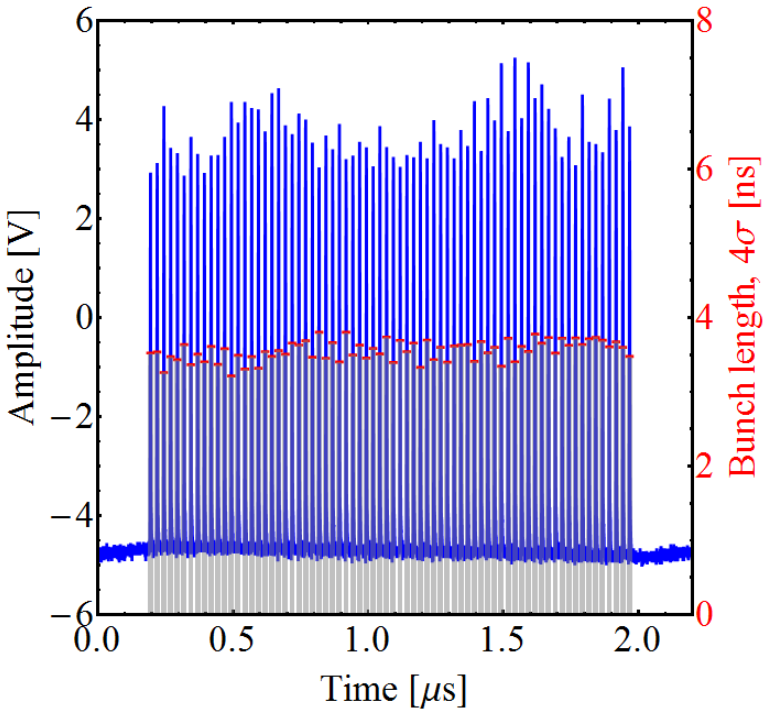

Figure 4.16. Beam longitudinal profile at last PS turn before extraction with the FB active [4].

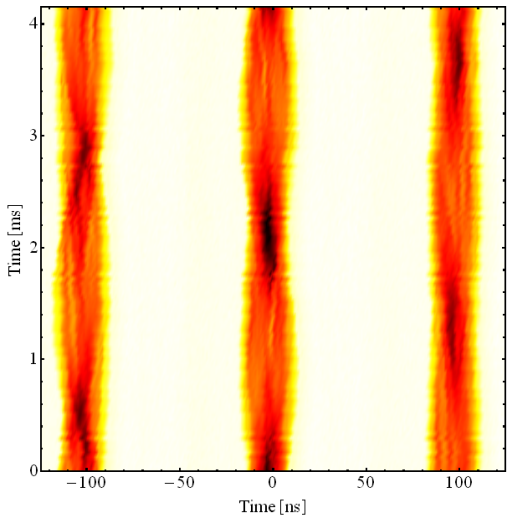

Figure 4.17. Bunch longitudinal oscillation with the FB on for an intensity $> 2 \cdot 10^{11}$ ppb; the beam seems to perform quadrupolar CB oscillation [4].

well as the simulation studies and predictions were performed under the assumption of only dipolar CB modes. If further investigation studies will confirm that those observed are quadrupolar oscillations, then appropriate countermeasure should be taken, like a dedicated quadrupolar CB FB.

4.3 Summary

After its installation in early 2014, an extensive machine development program has been carried out to qualify the new Finemet wide-band damper cavity and its digital coupled- bunch LLRF FB system. The complete prototype feedback chain of pick-up, digital processing and Finemet kicker have been installed and commissioned. Excitation measurements with the FB in open loop show that the Finemet cavity interacts with the beam as expected and that the different coupled-bunch oscillation modes can be excited individually. Tests in 2016 confirm that coupled-bunch oscillations can be damped by the Finemet cavity in closed loop with an intensity of at least $2 \cdot 10^{11}$ ppb.

Bibliography

[1] M. Lonza, "Multi-bunch feedback systems," *CAS Sweden*, 2007.

[2] D. Boussard, "Cures of instabilities," *CAS CERN Accelerator School, Fifth Advanced Accelerator Physics Course*, 1993.

[3] L. Ventura, "Study of longitudinal multibunch instabilities for lhc-type beams at the cern proton synchrotron," *CERN PhD Thesis*.

[4] H. Damerau and L. Ventura, "Signal processing for the coupled-bunch feedback in the CERN PS," *Low Level Radio Frequency Workshop*, 2015.

[5] D. Perrelet, "New PS one-turn delay feedbacks and further developments," *CERN*.

[6] H. D. et al., "Longitudinal coupled-bunch oscillation studies in the CERN PS," *Proceedings of IPAC2013, Shanghai, China*, 2013.

Conclusions

Among various and challenging objectives of the LHC (Large Hadron Collider) Injectors Upgrade project (LIU), one aim is to double the beam intensity of the CERN Proton Synchrotron (PS) in order to achieve the integrated luminosity target of the High-Luminosity LHC project (HL-LHC). Each bunch at the extraction in the PS should nominally contain $2.6 \cdot 10^{11}$ proton within a total longitudinal bunch length of 4 ns.

Longitudinal coupled-bunch (CB) oscillations in the PS have been identified as one of the major challenge to reach the high intensity beam required by the HL-LHC project. Dipolar CB oscillations develop above the PS transition energy and cause asymmetries of the bunch splittings used to establish the required bunch spacing, compromising the quality of delivered beam train. The splitting is based on the precise control of the bunch phase and CB instabilities causes bunch oscillation preventing the phase control and thus spoiling the beam quality. In 2014 a new longitudinal kicker cavity has been installed, the Finemet cavity, as a part of the new digital longitudinal coupled-bunch feedback (FB) system. The Finemet cavity allows, with its large frequency bandwidth, to damp all the expected CB modes simultaneously.

During this PhD work an extensive study programme has been done to improve the understanding of coupled-bunch instabilities in the PS and to support the commissioning of the new coupled-bunch feedback.

The impedance contribution of the RF equipment in the PS has been analyzed starting from the present knowledge of the machine impedance to derive a resonant expansion to be used in the macroparticle simulation code MuSiC. This allowed to extrapolate the dipolar modes evolution in different machine configurations. From simulations it has been possible to show that the 10 MHz system is the main source of instabilities and to confirm that the contribution of the Finemet cavity and the high frequency cavities to the couple-bunch instability is negligible. Simulations with the present beam intensity are compatible with the measurements in term of dipolar modes observed and growth rate evaluated.

An original algorithm has been developed and proposed to analyze the coupled-bunch oscillation and to perform the mode analysis of the system in order to study its stability. With this numerical approach it is possible to define the eigenmodes of the system with sub-nanosecond detection of the bunch oscillation for a generic

impedance and bunch pattern. The stability of the PS has been studied with this approach for the nominal filling pattern. Moreover the procedure to evaluate a generic base of mode in a non-circulant system has been described.

The complete feedback chain of pick-up, digital processing and Finemet kicker has been installed and commissioned in 2014 and 2015. A dedicated measurement campaign was performed to qualify both the wide-band damper cavity as well as the new digital coupled-bunch low-level RF feedback system. Multiple scans have been performed with FB in open loop on each of the system's key parameters to explore the sensitivity of the excitation and verify that the Finemet cavity interacts with the bunch train as expected. Through a synthesis of measurements and macroparticle simulations it was possible to demonstrate that, with a reasonable sensitivity of the pickup, the Finemet cavity voltage is sufficient to damp dipolar CB instability with an intensity of $2.6 \cdot 10^{11}$ protons per bunch.

Since 2016 the longitudinal CB feedback system allowed to explore the longitudinal dynamics of the beam in the PS with an intensity never observed before. Tests showed that coupled-bunch oscillations can be damped by the new feedback system up to an intensity of $2 \cdot 10^{11}$ protons per bunch at extraction. For intensity above $2 \cdot 10^{11}$ ppb the FB still damps dipolar CB oscillations but the bunch seems to perform quadrupolar CB oscillations. Still, a 30% in intensity needs to be achieved to reach the project goal, but now (2016) the dipolar CB instabilities issue has been addressed and solved by the CB feedback system; the quadrupolar oscillation needs to be studied in details but the FB system and the damper cavity, with a new dedicated LLRF, can be used to solve this new problem.

Ringraziamenti

> "Ma come mai tentiamo se gli ostacoli sono tanto alti e le possibilità di successo tanto basse? Perché non facciamo i bagagli e non torniamo a casa? Sarebbe molto più facile. È perché, alla fine, non c'è gloria nel facile. Nessuno ricorda le cose facili. Si ricorda il sangue e le ossa e la battaglia lunga e angosciosa per arrivare in cima. Ed è così che diventi una leggenda."

Vorrei ringraziare in questa ultima pagina tutte le persone che hanno contribuito alla nascita e allo sviluppo di questa tesi: chi con una collaborazione costante, chi con un supporto morale, chi con consigli, suggerimenti o parole di incoraggiamento.

Ringrazio il mio supervisor al CERN Dr. Guido Sterbini per avermi indicato sempre la giusta soluzione ai problemi che si sono presentati. Questo lavoro non avrebbe mai visto la luce senza il suo supporto, la costante presenza, disponibilit*á*, gentilezza ed infinita pazienza nei miei confronti.
Thanks to Heiko Damerau for helping and guiding me during my entire journey at CERN, it has been a privilege to work with him.
Un ringraziamento particolare va al Prof. Mauro Migliorati, mio mentore fin dall'inizio di questa avventura al CERN. Grazie per avermi dato questa stupenda opportunita e per non avermi mai fatto mancare, anche da lontano, il supporto di cui avevo bisogno.

Grazie ai miei amici di una vita Federica, Laura, Letizia e Stelvio, anche se da lontano ho sempre saputo di poter contare su di voi. Grazie per le risate e le serate insieme e per la vostra importantissima amicizia. Un ringraziamento particolare va alle persone che hanno condiviso con me questi anni a Ginevra: Annalisa, Claudia e Giorgia. Mi hanno sempre incoraggiata a stringere i denti nei momenti difficili e hanno festeggiato con me le vittorie nelle tappe che mi hanno portata a tagliare questo traguardo. Anche se saremo lontane sappiate che sarà impossibile dimenticare quanto abbiamo vissuto insieme. Mi ritengo molto fortunata di avervi conosciuto e di aver affrontato questo straordinario percorso insieme a voi.

Grazie a Michele per essermi sempre stato accanto in tutti questi anni, avermi sopportata e avermi fatto superare momenti difficili con il suo straordinario modo di fare.

Grazie a Debora e Silvia, per avermi sopportata e supportata, per la vostra presenza, i consigli, la gioia e l'allegria che date alla mia vita. Senza di voi non potrei essere

quella che sono.
Ed infine grazie ai miei genitori che in tutti questi anni mi hanno spronata e aiutata nei momenti difficili, grazie al loro sostegno continuo ho potuto raggiungere questo importante obiettivo.

AD MAIORA.